Correlated behavior of electrostatically trapped dipolar excitons at low temperatures

Dissertation der Fakultät für Physik
der Ludwigs-Maximilians-Universität München

vorgelegt von
Georg J. Schinner
geboren in Neustadt an der Waldnaab
München, März 2012

Erstgutachter: Prof. Dr. Jörg P. Kotthaus
Zweitgutachter: Prof. Dr. Alexander W. Holleitner
Tag der mündlichen Prüfung: 25.05.2012

Contents

Zusammenfassung

In der vorliegenden Doktorarbeit werden photogenerierte räumlich indirekte Exzitonen in gekoppelten InGaAs Quantentrögen experimentell untersucht. Die räumliche Trennung von Elektronen und Löchern in zwei benachbarte Quantentröge ist die Ursache für die lange Lebensdauer und das große Dipolmoment dieser Exzitonen. Der Dipolcharakter der Exzitonen erlaubt die Erzeugung von elektrostatisch abstimmbaren zweidimensionalen Potentiallandschaften. Hierzu werden neu entworfene nanostrukturierte Gatter auf die Probenoberfläche aufgebracht. Das Forschungsinteresse an diesem System wird dadurch geweckt, dass die indirekten Exzitonen starke Dipol-Dipol-Wechselwirkung zeigen und gleichzeitig wegen des bosonischen Charakters der Exzitonen die Bose-Einstein Kondensation vorausgesagt wird. Zur Untersuchung der Fallenstrukturen wird ein neues Anregungs- und Detektionsschema eingeführt. Herzstück dieses Aufbaus ist ein neu entwickeltes ^{3}He gekühltes konfokales Mikroskop mit zwei unabhängig voneinander beweglichen Objektiven. In dieser Arbeit werden zwei Arten von Fallen erforscht.

Das erste Fallendesign sind kreisrunde Fallen mit einem Durchmesser von 6 μm. Dieses Design erlaubt die Beobachtung von kollektiven Vielteilchen-Effekten thermalisierter exzitonischer Ensembles mit etwa 10^4 indirekten Exzitonen. Die optische Anregung von Exzitonen erfolgt außerhalb der eigentlichen Falle, so dass diese nur mit auf die Kristallgitter-Temperatur von 250 mK vorgekühlten und langlebigen Exzitonen gefüllt wird. Diese eingeschlossenen kalten Exzitonen-Ensembles besitzen eine thermische de Broglie Wellenlänge, die deutlich größer ist als der Teilchenabstand, und das Dipolmoment aller Exzitonen ist senkrecht zur Quantentrogebene ausgerichtet. Deshalb wird ein korreliertes Verhalten der Exzitonen in ihrer Photolumineszenz als Funktion der eingeschlossenen Dichte und Temperatur beobachtet. Mit abnehmender Temperatur zeigen sich Vielteilchen-Korrelationen in einer starken Zunahme der emittierten Photolumineszenz-Intensität sowie einer energetischen Verschmälerung der Photolumineszenz-Linie, die zusätzlich eine starke Asymmetrie entwickelt. Bei tiefen Temperaturen wird mit zunehmender Exzitonen-Dichte ein exponentieller Anstieg der Photolumineszenz-Intensität sowie eine Abnahme der spektralen Linienbreite beobachtet.

In Fallen, die in der lateralen Ausdehnung eine Größenordnung kleiner sind, ist es gelungen den Übergang von einem Vielteilchen-Zustand zu einem einzelnen Exziton zu studieren. In diesen Fallen, bevölkert mit einer geringen Anzahl von Exzitonen, werden diskrete Photolumineszenz-Linien beobachtet, welche die charakteris-

tischen Eigenschaften von einem einzelnen Exziton, Biexziton und Triexziton zeigen. Diese diskreten Photolumineszenz-Energien sind das Ergebnis der räumlichen Quantisierung durch das Einschlusspotential der Falle und der Dipolwechselwirkung der indirekten Exzitonen. Mit dieser Quantenfalle ist die erstmalige Realisierung und Charakterisierung eines mit Gattern definierten, optisch aktiven Quantenpunkts gelungen. Sie eröffnet eine Vielzahl neuer Anwendungen.

Einer der Quantentröge ist gatterspannungsabhängig an den Rückkontakt der Feldeffektstruktur gekoppelt. Das ermöglicht die Ausbildung eines zweidimensionalen Elektronensystems in diesem Quantentrog. Optisch erzeugte Elektron-Loch-Paare bilden in der Gegenwart des zweidimensionalen Elektronensystems Mahan-artige Exzitonen. Die Photolumineszenz dieser Exzitonen zeigt im senkrechten Magnetfeld einen ganzzahligen und gebrochenzahligen Quanten-Hall-Effekt. Die elektrostatische Abstimmbarkeit der Fallen erlaubt die Realisierung einer Fallenkonfiguration, die nur neutrale Exzitonen einfängt und kein zweidimensionales Elektronensystem enthält. Die Befüllung der Falle mit Exzitonen wird aber stark durch die Landau-Quantisierung des umgebenden zweidimensionalen Elektronensystems beeinflusst. Die eingeschlossenen, neutralen Exzitonen zeigen durch langreichweitige Wechselwirkungen über den Fallenrand hinweg Quanten-Hall-Effekt Signaturen.

1. Introduction

The periodic arrangement of atoms in a crystal causes the formation of a band structure. The energy bands are filled with the available electrons of the outer atomic orbitals. In an undoped semiconductor at low temperatures the so called valence band is the highest band fully occupied with electrons. It is separated by an energy gap from the lowest empty band, called the conduction band. An optical excitation of the crystal by the absorption of a photon can lift an electron from the valence band into the conduction band. The empty state left behind in the valence band can be described by a positively charged quasi particle called a hole. This state is the result of the collective behavior of the remaining electrons. Since electron and hole are fermions of opposite charge they are bound by Coulomb attraction and form a state comparable to a hydrogen atom or a positronium atom. This new bound quasi particle is called a Mott-Wannier exciton [Wannier 1937; Mott 1938] and it can be considered as a composite boson. Therefore, since the 1960s it is expected that excitons can undergo a Bose-Einstein condensation (BEC) [Blatt et al. 1962; Moskalenko 1962; Casella 1963; Keldysh et al. 1968]. Considering the fact that the critical temperature of the quantum degeneracy scales inversely with the particle mass, excitons have been considered as promising candidates for an exciton BEC at temperatures of about 1 K, which is several orders of magnitude higher than for atoms [Butov et al. 2002; Anderson et al. 1995]. In contrast to atomic systems, a convincing demonstration of an excitonic quantum phase transition to a bosonic ground state is sill missing [Snoke 2011].

The realization of an atomic condensate in 1995 is the result of the combination of laser cooling with evaporative cooling and the spatial confinement of the ultra cooled atomic gas in a magneto-optical trap [Anderson et al. 1995; Davis et al. 1995; Phillips 1998]. The transition temperature of alkali atomic gases is below one microkelvin. Experiments have shown that the atomic BECs behave like a coherent matter wave with long range phase coherence [Andrews et al. 1997; Bloch et al. 2000] and exhibit superfluidity [Matthews et al. 1999; Raman et al. 1999]. The same cooling technique is used to achieve a Bardeen-Cooper-Schrieffer (BCS) superfluidity of fermionic atom gases [Holland et al. 2001; Giorgini et al. 2008]. The Feshbach resonance allows the reversible conversion of a Fermi gas in a gas of bosonic diatomic molecules which undergo Bose-Einstein condensation [Regal et al. 2003; Strecker et al. 2003; Greiner et al. 2003; Jochim et al. 2003]. This is the basis for the realization of a BCS-BEC crossover in a atomic Fermi gas [Regal et al. 2004]. The full tunability of

the magneto-optical trap enable the opportunity to study the atom condensation in one- and two-dimensional systems and their dimensional crossover [Hadzibabic et al. 2006; Cladé et al. 2009; Sommer et al. 2012].

These overwhelming prosperous realizations of atomic condensates stimulated strong research interests in excitonic systems. Furthermore, such investigations are motivated by the successful realization of a non-equilibrium condensate of exciton-polaritons which are strongly related to excitons [Kasprzak et al. 2006; Balili et al. 2007; Deng et al. 2010]. The challenge in pure excitonic systems is to trap a sufficiently high density of thermalized excitons within their short lifetime. A promising system that has been extensively investigated in recent years, is the two-dimensional system of spatially separated electron and hole layers based on a semiconductor heterostructures [Lozovik et al. 1975; Fukuzawa et al. 1990; Timofeev et al. 1999; Finck et al. 2011; Kuznetsova et al. 2012; Alloing et al. 2012b; Matuszewski et al. 2012]. In such a coupled double quantum well heterostructure, spatially indirect excitons are formed with a permanent dipole moment. Therefore spatially indirect excitons are alternatively called dipolar excitons. The main advantages of the dipolar excitons are a long lifetime up to $50\,\mu$s [Vörös et al. 2006] and a high cooling rate which allows the creation of cold excitonic ensembles [Ivanov et al. 1997; Ivanov et al. 1999]. The dipolar character causes a repulsive force between the indirect excitons preventing the formation of excitonic molecules. Finally, the exciton energy can be tuned via the quantum confined Stark effect (QCSE) [Miller et al. 1984; Miller et al. 1985; Chen et al. 1987]. This allows the creation of excitonic potential landscapes [Schinner et al. 2011a; Remeika et al. 2012; Kowalik-Seidl et al. 2012].

Fundamental research is the major motivation to investigate these two-dimensional bilayer systems. The main aim is the realization of a quantum phase transition such as an excitonic BEC [Keldysh et al. 1968] or the observation of a superfluid BCS state [Lozovik et al. 1976; Berman et al. 2007; Snoke 2011]. To reach this lofty goal of a coherent bosonic ground state, many elementary questions about the physical properties of the dipolar excitons have to be answered. The most investigated topics are exciton-exciton interactions [Vörös et al. 2009b], exciton diffusion [Vögele et al. 2009a], and the temporal dynamics of exciton ensembles [Alloing et al. 2012a].

Additionally, dipolar excitons exhibit physical properties of interest for potential applications in optoelectronic devices. Excitons excited by light can be voltage controlled stored in a so called photonic memory [Zimmermann et al. 1999; Lundstrom et al. 1999; Krauss et al. 2004; Winbow et al. 2007] and the polarization of the photon is conserved in the spin of the exciton [Leonard et al. 2009; Kowalik-Seidl et al. 2010]. This supplies a simple method to transfer quantum information from an optical field into the solid state [Boyer de la Giroday et al. 2011]. The exciton can be transformed back into a photon by simply switching an external voltage. The exciton, with an effective Bohr radius of $a_{\mathrm{B}}= 20\,\mathrm{nm}$, is small compared to the wavelength of the light and can be laterally transported by electrostatically formed

potential ramps [Gärtner et al. 2006], moving potentials created by surface acoustic waves [Rocke et al. 1997; Rudolph et al. 2007] or an electrostatic conveyer [Winbow et al. 2011]. Further the exciton flow can be controlled by excitonic transistors [High et al. 2007; Kuznetsova et al. 2010] and they can be assembled to excitonic integrated circuits to perform basic logical operations [High et al. 2008; Grosso et al. 2009].

In this work, we are interested in both possible applications as well as in the realization of a bosonic quantum phase transition of an excitonic ensemble. The aim of this thesis is the control of the exciton in-plane dynamics via electrostatically defined potential landscapes which are in-situ voltage tunable. The trapping configurations developed here allow the investigation of both an individual exciton as well as large thermalized excitonic ensembles with high densities.

Chapter 2 is introduced by a historical overview of the developments in the search for a coherent exciton condensate. This is followed by the presentation of the fundamental physical properties of dipolar excitons in a semiconductor heterostructure and how these excitons can be manipulated.

The used heterostructure with InGaAs quantum wells and the sample fabrication are described in Chapter 3. The major advantage of this novel InGaAs based heterostructure is the transparency of the GaAs substrate for the quantum well photoluminescence.

Therefore, it is possible to set up a new detection scheme by means of a confocal microscope with two objectives embedded in a ^{3}He refrigerator with a base temperature down to 240 mK. The complete experimental setup is shown in Chapter 4.

Chapter 5 is based on the publication [Schinner et al. 2011a]. In a first step, the InGaAs coupled double quantum well heterostructure device is characterized by gate voltage dependent photoluminescence measurements. In the next step a novel trapping configuration is introduced where the exciton generation is spatially separated from the trapping potential. Hence the trap is filled only with indirect excitons pre-cooled to the lattice temperature. In this device, the flow of dipolar excitons is efficiently controlled by gate voltages. Spatially and spectrally resolved photoluminescence measurements fully quantify the potential landscape and show that the excitons become trapped in a well-defined spatial region. Additionally, the in-situ voltage controlled tunability of the electrostatic trap is demonstrated. In the emission of the trapped excitonic ensemble, indications for the presence of collective effects are found. Varying gate voltages, switching effects are observed in the exciton flow, which are comparable to the behavior of excitonic transistors [High et al. 2007; Kuznetsova et al. 2010].

In Chapter 6 the dipolar excitons are pumped by resonantly excited excitons and cooled down to a lattice temperature of 240 mK. At these temperatures their ther-

mal de Broglie wavelength is comparable to the exciton separation and a correlated behavior is observed as a function of the trapped exciton density and lattice temperature. With decreasing temperature, many-body correlations manifest themselves in a strongly increasing integrated intensity as well as a decreasing linewidth of the photoluminescence. At lowest temperature and with increasing exciton density this is accompanied by a non-linear and spectral asymmetric increase of the emission intensity as well as a narrowing of the photoluminescence linewidth. In the analysis of the red tail of the luminescence lineshape, the correlations are found to be reflected in the appearance of a density and temperature dependent power law. This chapter is built on the manuscript [Schinner et al. 2011b] which presently is under review at Physical Review Letters.

Chapter 7 is based on a manuscript which is also in a review process at Nature. It demonstrates the first realization of an electrostatically gate-defined and optically active individual quantum dot. These new quantum traps allow sequential single exciton occupation and combine the advantage of electrostatic tunability with the possibility of studying single and multiple exciton physics. Discrete photoluminescence lines are observed which reflect the interplay of spatial quantization and interexcitonic dipolar repulsion. These interexcitonic interactions result in spatial correlations forming molecular-like structures within the quantum trap confining potential. These quantum trap introduce a new gate-defined platform for creating and controlling optically active quantum dots and open the route to lithographically defined quantum dot arrays with tunable in-plane coupling and voltage controlled optical properties of single exciton states. Thereby, it substantially contributes to achieve working quantum computation devices which build the interface between a stored solid state excitonic qubit and a flying photonic qubit [Tanzilli et al. 2005]. In a series of publications the optical, electrostatic, and optoelectronic coherent manipulation of excitonic qubits in quantum dots have been successfully demonstrated [Ramsay et al. 2008; Boyer de la Giroday et al. 2010; Zrenner et al. 2002; Michaelis de Vasconcellos et al. 2010].

In Chapter 8 a new quasi-particle, the Mahan-like indirect exciton is introduced. The coupled double quantum well is embedded between a degenerately doped back contact and mesoscopic surface gates that allow to tune the device by a voltage such that the electrons from the doped back contact are transferred to the adjacent quantum well forming a degenerate two-dimensional electron system (2DES). Optically generated electron-hole pairs interact with the 2DES and form Mahan-like excitons [Mahan 1967]. The photoluminescence of Mahan excitons in a quantizing magnetic fields is studied and it is found that they strongly reflect both integer and fractional quantum Hall effect. The investigated device also contains an individually voltage-tunable electrostatic trap which collects and confines neutral dipolar excitons from the surrounding bath of long-living dipolar Mahan excitons. Though the 2DES is electrostatically expelled from the trap, the neutral dipolar excitons in the trap are surprisingly found to exhibit quantum Hall effect signatures, mediated by non-local

interactions across the trap perimeter with the surrounding 2DES. Thus the created devices offers the opportunity to study non-local many-body interactions via spatially resolved photoluminescence in the quantum Hall effect regime. This chapter is based on a manuscript which is in a review process at Physical Review Letters.

2. Exciton basics

In this chapter the fundamental theoretical properties of excitons are described. At the beginning the historical background is summarized which motivates this work. Then the electron-hole bilayer system with dipolar excitons is introduced and the most significant physical properties are discussed. More details about indirect excitons can be found in the following review articles [Snoke et al. 2005; Kotthaus 2006; Rapaport et al. 2007].

2.1. Historical overview

The spontaneous condensation of an ideal atomic gas into the lowest energy state with zero momentum has been first predicted by Einstein in two famous papers [Einstein 1924; Einstein 1925]. Einstein´s work was inspired by a paper of Bose [Bose 1924] on the statistical properties of indistinguishable photons in the black-body radiation. Einstein applied this concept to massive atoms and justified his approach by using the new idea of de Broglie´s matter waves for the the first time. Schrödinger heard about this concept of matter waves the first time by reading Einstein's papers [de Broglie 1924; Griffin 1999]. The now called Bose-Einstein statistics was established both before the introduction of Fermi statistics [Fermi 1926] as well as the division of the particles into fermions and bosons in 1927. Physicists ignored the concept of Bose-Einstein condensation for many years because there was no practical significance. In 1938 superfluid ^{4}He was discovered [Allen et al. 1938; Kapitza 1938] and London recognized the analogy to an ideal Bose gas and Bose-Einstein condensation [London 1938]. A similar idea has been predicted by Blatt for superconductors and it was proposed that at low temperatures charge carrying bosons can occur [Schafroth 1954; Blatt et al. 1954]. In 1956 Cooper found that a pair of fermions forms a bosonic bound state. In the following year superconductivity was successfully described by the Bardeen-Cooper-Schrieffer (BCS) theory [Bardeen et al. 1957a; Bardeen et al. 1957b]. Nowadays the established and accepted definition of BEC is that a large fraction of bosons spontaneously occupies the same quantum state which can be described by a macroscopic wavefunction with a spontaneous long-range coherence (see Fig. 2.1). This picture unifies the understanding of BEC, superconductivity, and superfluidity [Penrose et al. 1956; Yang 1962].

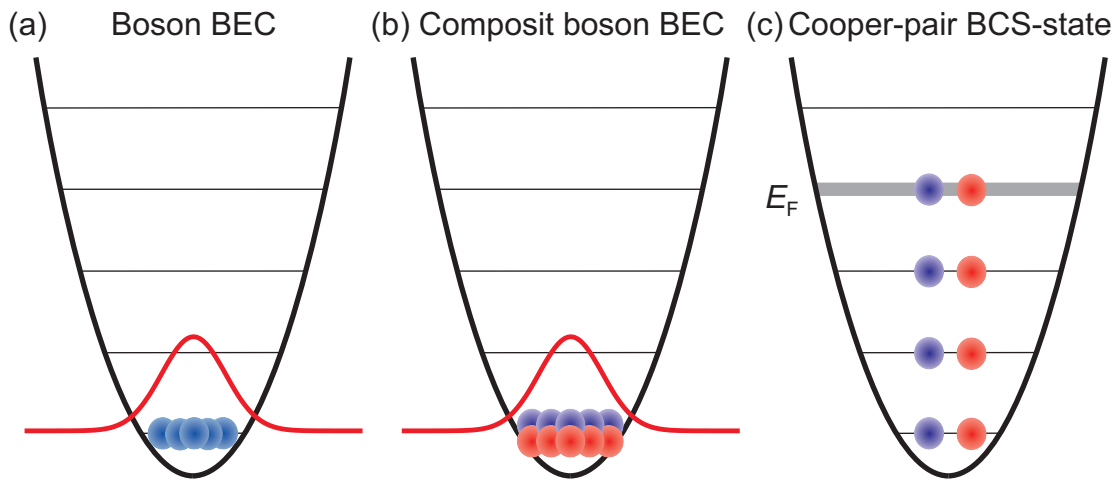

Figure 2.1.: **BEC versus BCS-state.** The confinement of different particles in a harmonic trap at $T = 0$ is shown. In (a) a Bose-Einstein condensate is illustrated. The groundstate of the harmonic oscillator is macroscopically occupied with bosons, e.g. bosonic atoms, which can be described by a macroscopic wavefunction (see Equation (2.11)). The Bose-Einstein condensate of composite bosons, for example diatomic molecules or diluted excitons, is shown in (b). In (c) the condensate of Cooper pairs in a BCS superfluidity or superconductivity state is illustrated. Caused by the Pauli exclusion principle fermions form a Fermi sea where all energy states up to the Fermi energy are occupied. The red and blue balls are for example $|\uparrow\rangle$ and $|\downarrow\rangle$ fermionic states. The BCS state in (c) is characterized by collective excitation modes, a pairing gap, and the formation of vortices.

After the BCS-theory became generally accepted again, Blatt developed the idea of the possibility that a gas of hydrogen-like excitons can undergo a Bose-Einstein condensation [Blatt et al. 1962]. The excitons can be considered as composite bosons because they consist of electron and hole which both are of fermionic nature. The resulting Coulomb bound state has an integer-value spin. In the dilute limit with $na_B^d \ll 1$, where n is the exciton density, a_B the exciton Bohr radius, and d the dimensionality, excitons can be treated as a weakly interacting Bose gas [Keldysh et al. 1968]. It is expected that a phase transition from a classical to a quantum gas occurs as soon as with decreasing temperature T the thermal de Broglie wavelength

$$\lambda_{dB} = \frac{\hbar}{\sqrt{2\pi MkT}} \tag{2.1}$$

of the excitons with mass M becomes comparable to the interparticle separation ρ as illustrated in Fig. 2.2(a). The mass M is the sum of the electron and hole mass $M = m_e + m_h$ and is normally smaller than the mass of a free electron.

Furthermore, the quantum degeneracy temperature is inversely proportional to the mass. Therefore a critical temperature is anticipated of about 1 K which is orders of magnitude higher than for atoms [Anderson et al. 1995; Butov et al. 2002]. The low mass is the main advantage of the bosonic excitons allowing a quantum phase transition at temperatures accessible with standard cryogenic techniques. But the bosonic nature of the exciton is fragile because of the small binding energy and the large Bohr radius. With increasing exciton density phase space filling causes an overlap of the wavefunctions and a significant occupation of the fermionic phase space [Schmitt-Rink et al. 1985; Schmitt-Rink et al. 1989]. In this high density limit $na_{\mathrm{B}}^{d} \gg 1$ excitons can be conceived as uncharged Cooper pairs and a BCS-like condensate is expected which is called excitonic insulator [Keldysh et al. 1968]. BCS-theory is expected to describe this state because it accurately explains superfluid ^{3}He and aspects of high temperature superconductors [Osheroff et al. 1972; Chen et al. 2005]. At higher exciton densities and above a certain temperature dissociation of excitons produces free charge carriers which screen the Coulomb binding of the excitons. This causes the so called Mott transition to an electron-hole plasma (EHP) [Schmitt-Rink et al. 1989; Stern et al. 2008a]. In Fig. 2.2(b) a strongly simplified general structure of a possible excitonic phase diagram is illustrated. With increasing exciton density a BEC-BCS transition is predicted [Hakioglu et al. 2007].

After the proposals of the 1960s the search for an excitonic quantum phase transition started. But direct gap semiconductors are not well suited for an excitonic

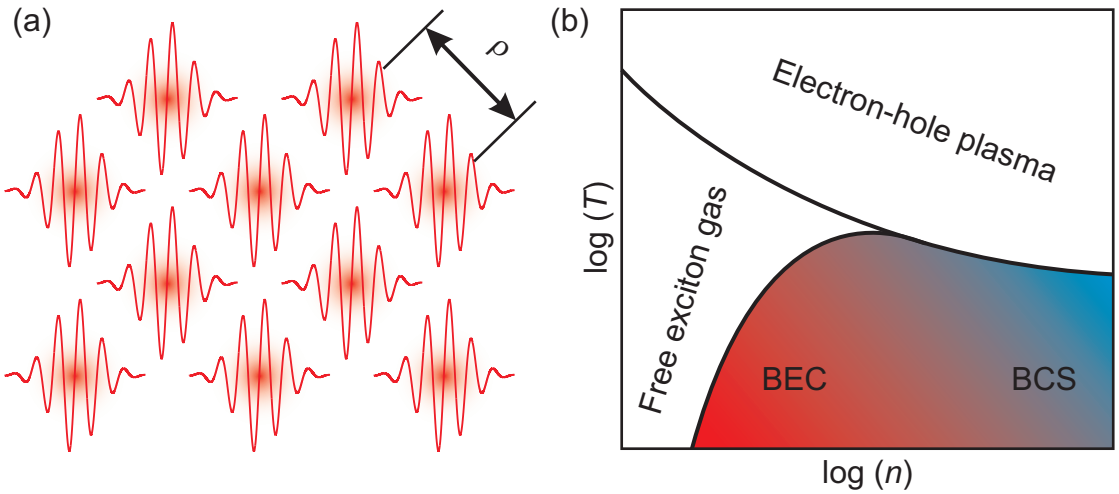

Figure 2.2.: **Quantum phase transition of excitons.** (a) A phase transition is expected to occur when the exciton separation ρ is comparable to the thermal de Broglie wavelength λ_{dB}. (b) Shows a simplified thermodynamic phase diagram of an excitonic ensemble (similar to [Snoke 2011]). With increasing density n a crossover from a BEC to BCS-state is expected.

BEC because of the strong exciton-photon coupling. The problem is to cool the photo-excited excitonic ensemble down to the crystal lattice temperature within the short lifetime of the excitons. In order to thermalize an excitonic ensemble close to the lattice temperature the excitonic lifetime should significantly exceed the energy relaxation time.

Other suitable candidates seem to be indirect gap semiconductors like Germanium and Silicon where phonons are involved in the radiative annihilation and therefore the equilibration is much faster than the optical decay [Gergel et al. 1968]. These materials are characterized by a strong anisotropy of the effective masses and a strong orbital degeneracy where the excitonic state is not the ground state. The lowest energetic state is a metallic electron-hole liquid and the occurrence of this phase is caused by an attractive interaction between the excitons. Over the last 30 years, the best investigated and most promising bulk semiconductor for BEC is cuprous oxide [Hulin et al. 1980; Snoke et al. 1990; Fortin et al. 1993; Kubouchi et al. 2005; Yoshioka et al. 2011]. Here, the excitons are characterized by a very high binding energy as well as an optically dipole forbidden excitonic ground state with a lifetime of a microsecond which enables the thermalization of the excitons with the lattice.

In the recent years, excitons in electron-hole bilayer systems have been extensively investigated [Fukuzawa et al. 1990; Kash et al. 1991; Butov et al. 2002; Stern et al. 2008b; Vörös et al. 2009b; Snoke 2011; Sivalertporn et al. 2012; Kowalik-Seidl et al. 2012]. In 1975, this two-dimensional system was proposed and it was expected that in this scheme superfluidity should be observable [Lozovik et al. 1975]. Spatially indirect excitons in coupled double quantum well heterostructures are characterized by a high cooling rate and long lifetime due to the spatial separation of the electrons and holes in two adjacent quantum wells. This two-dimensional system is the topic of this thesis and will be described in the next sections in more detail.

2.2. Bose Einstein condensation in two-dimensional systems

In contrast to three-dimensional systems where independent of the interaction between the bosonic particles and independent of the size of the system a Bose Einstein condensation always theoretically can occur, the situation in two dimensions is more complicated as illustrated in Table 2.1. In an infinite, translationally invariant two-dimensional system with a non-interacting Bose gas Bose-Einstein condensation can not occur, because phase fluctuations inherent to the system prevent any spontaneous coherence [Hohenberg 1967; Mermin et al. 1966]. The general expression of the number of Bosons N as a function of the chemical potential μ and the temperature

2D	**no interaction**	**interaction**
infinite	no condensation	BKT
trap	BEC	BEC / BKT

Table 2.1.: **Condensation in two-dimensions.** In two dimensions the possibility of a quantum phase transition depends on the size of the system and the interaction between the bosonic particles as indicated.

T is given by

$$N(\mu, T) = N_0 + \int_0^\infty \frac{D(E)}{e^{\frac{1}{kT}(E-\mu)} - 1} \tag{2.2}$$

where N_0 is the number of condensed particles with an energy $E = 0$ and $D(E)$ is the density of states. In a d dimensional system the density of states of massive particles with kinetic energy $E = \frac{(\hbar k)^2}{2M}$ can be expressed by

$$D(E) \propto E^{\frac{d}{2}-1}. \tag{2.3}$$

Bose-Einstein condensation in Einstein's sense occurs when the integral in Equation (2.2) has a finite value for $\mu = 0$ and further added particles have to go into the ground state where they form a condensate. The integral in Equation (2.2) shows an upper bound for

$$D(E) \propto E^q \tag{2.4}$$

with $q > 0$. Therefore the shape of $D(E)$ is essential and in two dimensions where $D^{2d}(E) = const.$ condensation is not allowed and added bosons occupy the normal phase with a finite energy. On the other hand, in three dimension where $D^{3d}(E) \propto E^{\frac{1}{2}}$ and in the harmonic trapped case $D^{3d}_{trap}(E) \propto E^2$ the integral in Equation (2.2) converts and Bose-Einstein condensation can take place [Mullin 1997; Posazhennikova 2006].

To achieve a condensate in two dimensions it is necessary to use a trap [Widom 1968; Bagnato et al. 1991; Li et al. 1999]. In the following, an isotropic harmonic trap is introduced as realized in the experiments (see Chapter 7). The trap profile is given by

$$V = \frac{1}{2}\alpha r^2 = \frac{1}{2}M\omega^2 r^2 \tag{2.5}$$

where α is the spring constant, M the particle mass and $\hbar\omega$ the quantization energy of the harmonic oscillator. The total number of the bosonic particles in the two-dimensional harmonic trap is

$$N = \sum_{n_x,n_y}^{\infty} \frac{1}{e^{\frac{1}{kT}(\hbar\omega(n_x+n_y+1)-\mu)} - 1} = \sum_{n}^{\infty} \frac{n+1}{e^{\frac{1}{kT}(\hbar\omega(n+1)-\mu)} - 1} \tag{2.6}$$

where $n = n_x + n_y$ and $n = 0, 1, 2 \ldots$. The energy of the state n is $E_n = n\hbar\omega$ and the resulting density of states in two dimensions is

$$D^{2d}_{trap}(E) \propto E^1. \tag{2.7}$$

Therefore the integral in Equation (2.2) is finite so that Equation (2.6) can be rewritten as

$$N = N_0 + N_\mathrm{c} \quad \text{and} \quad N_c = \frac{\pi^2}{6}\frac{gM}{\hbar^2\alpha}(kT)^2, \tag{2.8}$$

where g is the spin degeneracy. From this the nonzero critical condensation temperature

$$T^{2d}_\mathrm{c} = \frac{\sqrt{6}}{\pi}\frac{\hbar\omega}{k}\sqrt{\frac{N}{g}} \tag{2.9}$$

follows as given by [Ketterle et al. 1996]. It is uncomplicated to calculate the two-dimensional condensate fraction

$$\frac{N_0}{N} = 1 - \left(\frac{T}{T_\mathrm{c}}\right)^2 \tag{2.10}$$

But this expression is exactly valid only for large particle numbers.

The harmonic trap potential allows not only the condensation in the two-dimensional momentum space but also spatial condensation. The condensate particles occupy the ground state of the harmonic oscillator and the wavefunction of the cloud of these particles (see Fig. 2.1) is given by

$$\varphi_0(\mathbf{r}) = \left(\frac{M\omega}{\pi\hbar}\right)^{\frac{1}{2}} e^{-\frac{M\omega}{2\hbar}\mathbf{r}^2} \tag{2.11}$$

From this, it is easy to find the spatial density distribution of the condensate [Dalfovo et al. 1999]

$$n_0(\mathbf{r}) = N_0 \mid \varphi_0(\mathbf{r}) \mid^2 \tag{2.12}$$

This position dependent density distribution is characterized by a Gaussian profile with a width ρ_0 of

$$\rho_0 = \sqrt{\frac{\hbar}{M\omega}} \tag{2.13}$$

as illustrated in Fig. 2.3.

In an interacting infinite two-dimensional Bose liquid, however a special type of order can occur which enables superfluidity [Kane et al. 1967]. The transition to this quasi-condensate is named Berezinskiĭ-Kosterlitz-Thouless (BKT) transition after the physicists who theoretically described it for the first time [Berezinskiĭ 1971; Berezinskiĭ 1972; Kosterlitz et al. 1973]. The BKT transition is characterized by the formation of vortices and a fluctuating phase avoiding a global phase of the

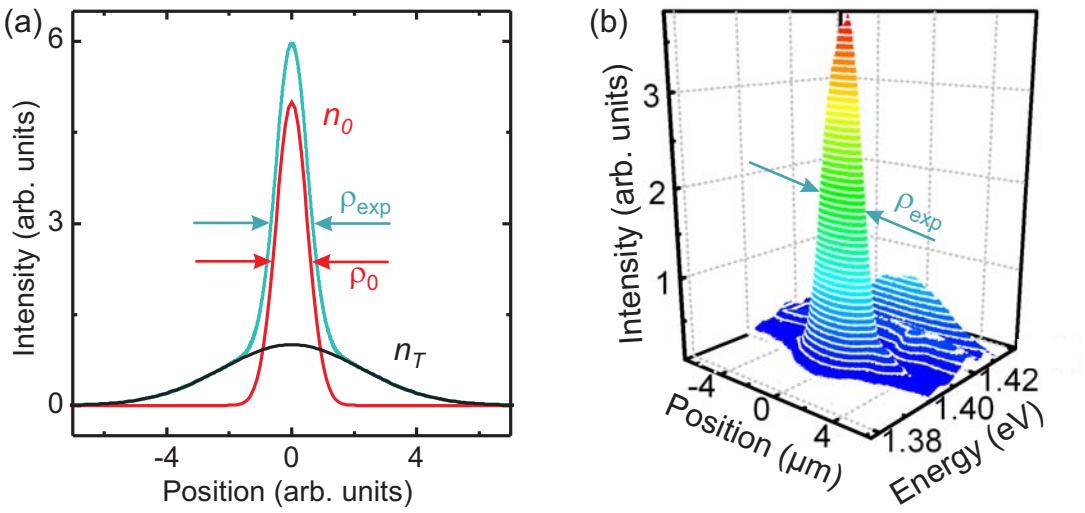

Figure 2.3.: **Spatial density distribution in a harmonic trap.** In (a) the theoretical density distribution of a cloud of trapped excitons is shown. The total density is the sum of the condensate density $n_0(\mathbf{r})$ and the thermal distribution of the non-condensate excitons $n_T(\mathbf{r})$. The pseudo-3D picture in (b) shows a spatially and energy resolved measurement of the exciton distribution in a harmonic trap as discussed in Chapter 7.

condensate. The coherence correlations of this quasi-condensate decay with a spatial power-law dependence [Berman et al. 2008c]. In a diluted Bose liquid it is expected that the BKT transition critical temperature T_c^{BKT} depends on the exciton density n as

$$T_c^{BKT} = \frac{4\pi\hbar^2 n}{2M \ln\ln(\frac{1}{na_B^2})} \tag{2.14}$$

where a_B is the Bohr radius which characterizes the interaction range. Superfluidity for an electron-hole bilayer system was first predicted by [Lozovik et al. 1975] and is still under consideration [Lozovik et al. 2002b; Berman et al. 2008b]. In the next section different possibilities are discussed, which exist to realize an electron-hole bilayer system.

2.3. Electron-hole bilayer structures

Since graphene became popular in 2005 [Novoselov et al. 2005], two-sheet graphene systems have been extensively theoretically investigated. It is expected that superfluidity and Bose-Einstein condensation of dipolar excitons occur in this system

[Berman et al. 2008a; Berman et al. 2012]. But practical relevance have up to now only semiconductor heterostructures containing a coupled quantum well grown by molecular beam epitaxy. In these samples two quantum wells are formed parallel to each other that are separated by a thin tunnel barrier.

One type of bilayer systems contains permanent excitons [Eisenstein et al. 2004; Yoon et al. 2010], which do not recombine into photons. Here, doping is used to create a degenerate two-dimensional electron system of equal density in each quantum well. A sufficiently high magnetic field causes half filled Landau levels so that in each well the lowest Landau level is filled half with electrons and half with holes binding to so-called quantum Hall excitons due to Coulomb attraction. This system stays always in the high-density regime and is investigated via transport experiments at millikelvin temperatures [Finck et al. 2010]. As a function of magnetic field and temperature a critical enhancement of the tunneling between the layers was observed and it is claimed that this is an indication for long-range coherence [Spielman et al. 2000; Eisenstein et al. 2004].

To create an optically active bilayer system undoped type I or type II quantum wells are used. In a type II like structure [Butov et al. 1994] the electron and hole layers are separated by using AlAs/GaAs coupled quantum wells as illustrated in Fig. 2.4(a). The formed dipolar excitons are spatially indirect as well as indirect in momentum space because an electron from the X point in AlAs layer is bound to a hole from the Γ point in the GaAs quantum well [Grosso et al. 2009].

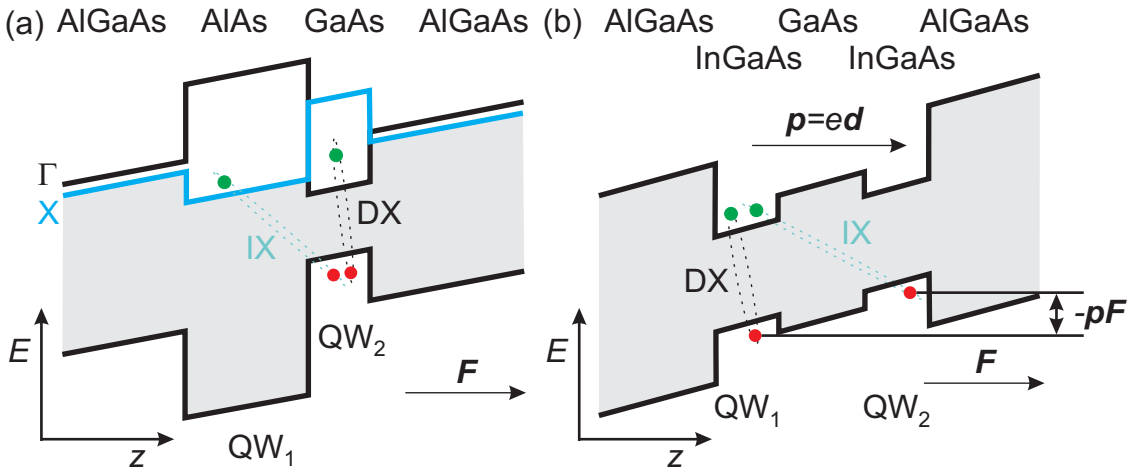

Figure 2.4.: **Quantum well bilayer systems.** Schematic representation of the energy band diagram in growth direction of (a) AlAs/GaAs coupled quantum wells and (b) type I quantum wells coupled via a tunnel barrier. Additionally, the formation of a direct exciton (DX) as well as an indirect exciton (IX) is shown, respectively, and **p** is the resulting indirect exciton dipole moment.

Most research groups investigate type I coupled quantum wells as shown in Fig. 2.4(b). Two undoped quantum wells are grown adjacent to one another. An electric field **F** applied perpendicular to the quantum well plane is used to tilt the band structure. By this, the optically excited electrons are confined in one quantum well and the corresponding holes are spatially separated confined in the other quantum well and form the indirect excitons. In most experiments, symmetric coupled quantum wells are used but for some studies it is advantageous to use asymmetric quantum wells with different well width to perform e.g. mass filtering or to resonantly excite intra well excitons in one quantum well [Stern et al. 2008a; Kukushkin et al. 2011]. The last method mentioned here to create indirect excitons is to remove the tunnel barrier between the quantum wells and work with a single wide quantum well. This approach avoids interfaces between the different quantum films and thereby reduces dramatically the interface roughness scattering due to fluctuation in the well width L. It can be easily shown that the mean interface roughness scattering time is $\tau \propto L^6$. And it was experimentally found that the electron mobility shows a L^6 power law dependence on the well width [Sakaki et al. 1987].

2.4. The excitonic life cycle

To create excitons, the heterostructure is illuminated with laser light of sufficiently high energy. Within about 20 ps after the initial excitation of an unbound electron-hole pair by photon absorption, an exciton is formed. Therefore a cascade of longitudinal optical and acoustical phonon emissions as well as carrier-carrier scattering events are necessary to relax the hot carriers [Damen et al. 1990; Eccleston et al. 1991; Blom et al. 1993]. Without an applied electric field, intra well excitons are created as shown in Fig. 2.5(a). These excitons are also called direct excitons with energy E_{DX} and the corresponding electrons and holes are confined within one quantum well. The two-dimensional localization of the exciton causes an increased binding energy compared to three-dimensional excitons [Miller et al. 1981; Bastard et al. 1982]. The optically created hot exciton ensemble then thermalizes through low energy bulk acoustic phonon emission within a few hundred picoseconds [Damen et al. 1990]. The cooling rate for excitons in quantum wells is about three orders of magnitude faster than in bulk semiconductors due to the relaxation of the momentum conservation in the growth direction perpendicular to the quantum well plane. The thermalization time increases with increasing exciton density, decreasing lattice temperature and increasing quantum well width [Ivanov et al. 1997; Ivanov et al. 1999]. As illustrated in Fig. 2.5(a) the electron and hole wavefunctions of the direct excitons show a strong overlap and therefore these intra well excitons are characterized by a short lifetime of about 1 ns dependent on both well width and temperature [Feldmann et al. 1987]. Within this short lifetime the direct excitons are nearly unable to thermalize and they can diffuse only short distances.

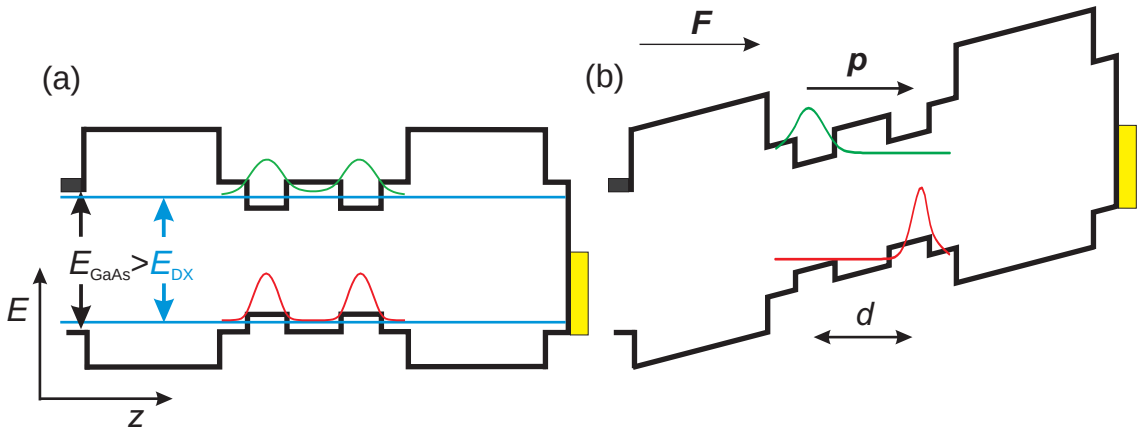

Figure 2.5.: **Simulated electron and hole wavefunction.** Schematic of the coupled double quantum well structure used in this thesis work. (a) Without applied bias and (b) with an electric field causing a band tilt. The plotted wavefunctions are obtained by solving the Poisson and Schrödinger equation with *nextnano*[3] for the heterostructure used in the experiments.

The situation is completely changed by applying a Stark electric field **F** tilting the band structure as plotted in Fig. 2.5(b). The tilting causes a tunneling of the constituents of the exciton, because the left quantum well is energetically favored for electrons and the right is preferred by holes. The binding energy of the now formed indirect exciton is only slightly reduced for sufficiently small electron-hole separation d. The Coulomb attraction is dominated by the electron-hole distance and as long as d is comparable to the Bohr radius the binding is only weakly influenced by the wavefunctions overlap [Szymanska et al. 2003]. As displayed in Fig. 2.5(b) the spatial separation of the electron and hole causes a strongly reduced overlap of the wavefunctions. The consequence is that the recombination rate decreases and the lifetime increases from about 1 ns for direct excitons up to 50 μs and more dependent on the wavefunction overlap integral [Vörös et al. 2006]. The lifetime is inversely proportional to the overlap integral. In this way, a variation of the applied bias influences the lifetime [Charbonneau et al. 1988; Alexandrou et al. 1990]. Figure 2.6(a) shows the calculated overlap integral as a function of the applied electric field. With increasing electric field the overlap integral decreases and consequently the lifetime increases by more than three orders of magnitude. This voltage tuneability of the excitonic lifetime can be used for practical applications in devices to store

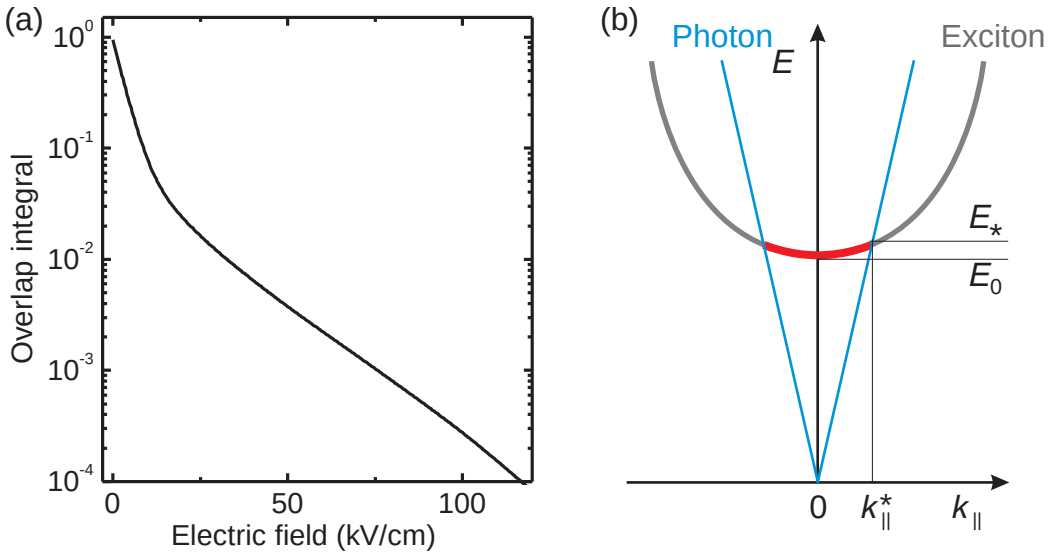

Figure 2.6.: **Electric field dependence of the overlap integral and exciton as well as photon dispersion relation.** In (a) the overlap integral quantifying the overlap of the electron and hole wavefunction is plotted as a function of the applied electric field. The overlap integral is obtained by solving the Poisson and Schrödinger equations with *nextnano*[3] for the heterostructure used in the experiments (see Section 3.1). With increasing electric field the overlap of the wavefunctions is reduced due to a rising localization of the electron wavefunction and hole wavefunction within the associated quantum well and consequently the lifetime increases. A second point which influences the radiative lifetime is illustrated in (b). The parabolic dispersion relation of the exciton and the linear dispersion of the emitted photon is shown. Because of in-plane momentum conservation only low-energy excitons from the radiative zone, with $|k_{\parallel}| < k^*_{\parallel}$ (highlighted in red) can emit a photon.

photons [Winbow et al. 2007; Winbow et al. 2008]. The long lifetime enables indirect excitons to thermalize with the crystal lattice, which is necessary for the realization of a quantum phase transition. Additionally, the long lifetime allows the excitons to explore an excitonic potential landscape and to flow towards the minimum of the potential or to diffuse over long distances [Vörös et al. 2006; Gärtner et al. 2007; Vögele et al. 2009a]. The exciton expansion is driven by diffusive forces, due to a gradient in the chemical potential and by strong repulsive interactions between the dipolar excitons (see Section 2.6.3). In addition to the overlap integral, the exciton in-plane momentum influences the excitonic lifetime. The exciton is annihilated by the radiative recombination of the electron with the hole and the emission of a corresponding resonant photon. Beside the exciton energy, the in-plane momentum

must be conserved as long as exciton scattering from impurities is sufficiently small. Therefore, only excitons from the so-called radiative zone can recombine by photon emission as illustrated in Fig. 2.6(b) [Feldmann et al. 1987; Butov et al. 2001]. The emitted photoluminescence light is the main experimental information source about the excitonic properties as described in the next section.

2.5. Photoluminescence analysis

To experimentally study the properties of an excitonic ensemble one can perform photon absorption experiments, measure tunnel currents of ionized excitons or analyze the emitted photoluminescence light as a function of external parameters. The first two methods we used to investigate unstructured two-dimensional systems and these techniques and the physical results are described in the diploma theses of [Stallhofer, Markus 2009; Schubert, Enrico 2010], originated in the frame of this thesis.

The recombining excitons couple directly to emitted photons and, by this, provide accessible information about the excitonic properties. In the case of an excitonic Bose-Einstein condensate, the coherence of the excitons should directly be reflected in the optical coherence of the emitted light, spectral and spatial narrowing as well as in the angular distribution of the photoluminescence and in the polarization of the emitted photons [J. Fernandez-Rossier 1997; Keeling et al. 2004; Snoke 2011].

In experiments, on exciton transport, the location where the photon is emitted is always interesting. This also plays a role when analyzing for example the spatial emission profile of a trap (see Fig. 2.3). The most important information is the energy of the photoluminescence light. Further interesting characteristics of the emitted light are the polarization, the emission angle, and the temporal statistical properties. To show the coherence of an excitonic ensemble it is necessary to investigate the first order temporal and spatial coherence of the radiated photoluminescence.

The spectrally resolved emission provides a statistic of the energetic distribution of the detected photons. It is informative to analyze the resulting photoluminescence lineshape. This lineshape is characterized by a spectral linewidth Δ_{FWHM} which is approximated by

$$\Delta_{\mathrm{FWHM}} = \sqrt{\Gamma_{\mathrm{hom}}^2 + \Gamma_{\mathrm{inhom}}^2}. \tag{2.15}$$

Where Γ_{hom} is the homogeneous broadening and Γ_{inhom} describes the inhomogeneous broadening due to disorder. The homogeneous broadening causes a more Lorentzian lineshape and Γ_{hom} is given by

$$\Gamma_{\mathrm{hom}} = \frac{\hbar}{\tau_{\mathrm{IX-IX}}} + \frac{\hbar}{\tau_{\mathrm{phonon-IX}}} + \frac{\hbar}{\tau_{\mathrm{rec}}}, \tag{2.16}$$

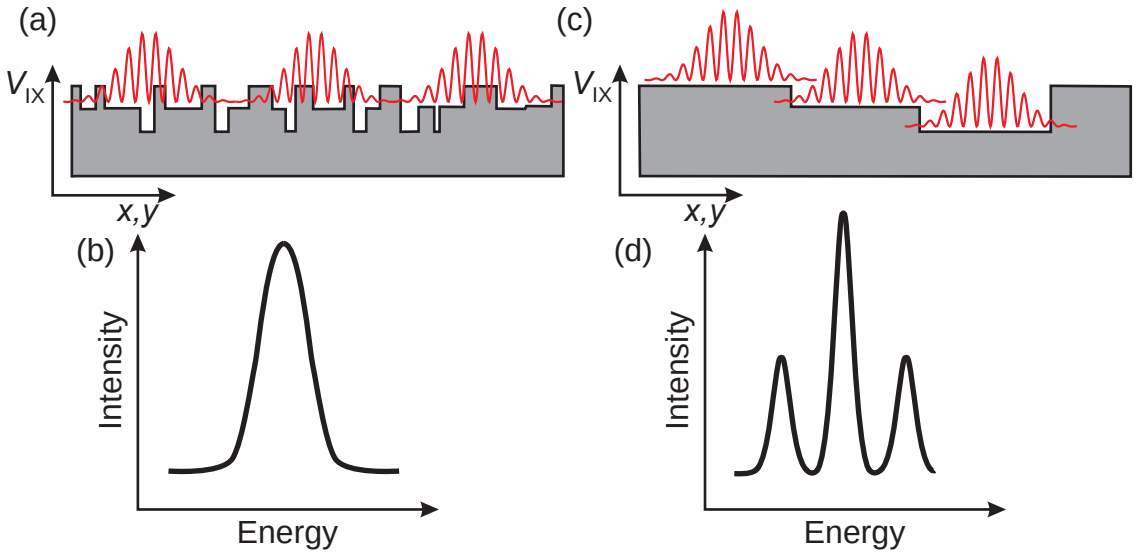

Figure 2.7.: **How the random disorder potential influences the photoluminescence lineshape.** In (a) the extent of the exciton wavefunction is large compared to the disorder correlation length. The corresponding photoluminescence line is plotted in (b). (c) Shows the case of long correlations in the disorder potential where the individual exciton sees a nearly constant potential. The corresponding photoluminescence lineshape (d) is characterized by discrete lines.

where $\tau_{\mathrm{IX-IX}}$ describes the exciton-exciton scattering caused by dipole-dipole interaction and phase-space filling effects (see Section 2.6.3). With increasing exciton density the exciton-exciton interaction dominates the linewidth. At low temperatures the $\tau_{\mathrm{phonon-IX}}$ plays a minor role and is caused by acoustic phonon scattering and piezoelectric phonon scattering [Basu et al. 1992]. τ_{rec} is the finite recombination lifetime. Here, this contribution to the line broadening is negligible because of the long excitonic lifetime.

The inhomogeneous disorder broadening Γ_{inhom} can be described by an average amplitude of the quantum well in-plane random disorder potential $\Gamma_{\mathrm{inhom}} =< U_{\mathrm{disorder}} >$ [High et al. 2009a]. The origins of the disorder potential are impurities, crystal defects, and alloy fluctuations that cause changes in the band gap especially in InGaAs. Additionally, quantum well width fluctuations created by the interface roughness are a source for disorder. The inhomogeneous broadening is most important at low exciton densities. With increasing density the random disorder potential is effectively screened by the dipolar excitons [Ivanov 2002]. The in-plane lateral correlation length and the energetic amplitude of the fluctuations characterize the random disorder potential as illustrated in Fig. 2.7. If the correlation length is small compared to the excitonic Bohr radius, the exciton wavefunction explores all fluctuations (see Fig.

2.7(a)). The corresponding photoluminescence lineshape is structureless and inhomogeneously broadened by the random disorder potential as shown in Fig. 2.7(b). On the other hand, if the correlation length is larger than the envelope wavefunction, as illustrated in Fig. 2.7(c), the luminescence spectrum shows separated, discrete emission lines (see Fig. 2.7(d)).

In Chapter 6 and Chapter 7 the photoluminescence lineshape is analyzed in detail. Therefore the red low-energy side and blue parts of the line are separately investigated. From the blue high-energy side it is possible to extract an upper limit of the exciton gas temperature. In the analysis of the red tail of the photoluminescence lineshape characteristic power laws are found, which are interpreted to reflect exciton correlations.

2.6. The dipole nature of double-layer excitons

The spatial separation of the electron and hole in two adjacent quantum wells forms an exciton with a permanent dipole moment $\mathbf{p} = e\mathbf{d}$ where $\mathbf{d}$ is the electron-hole separation. Therefore the indirect exciton is often called dipolar exciton. The dipolar excitons are all aligned and oriented perpendicular to the quantum well plane as illustrated in Fig. 2.8. One consequence of the dipolar character of indirect excitons is the above mentioned possibility to screen the random disorder potential. A further result is the large quantum confined Stark effect.

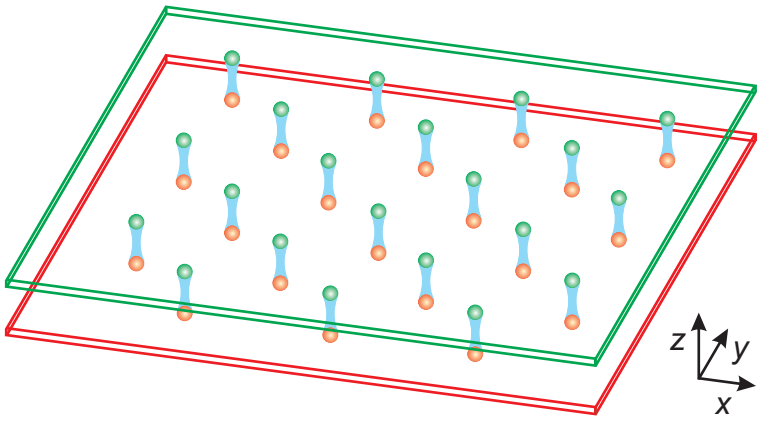

Figure 2.8.: **Spatial arrangement of dipolar excitons.** The dipolar excitons are aligned and oriented perpendicular to the quantum well plane. In addition, the strong dipolar repulsion can cause a spatially ordered arrangement of the excitons at low temperatures.

2.6.1. Quantum confined Stark effect

The energy of the dipolar excitons depends on the electric field that is applied to tilt the band structure. The energy of an indirect exciton with a dipole moment $\mathbf{p}$ is red shifted in an electric field $\mathbf{F}$ by

$$\Delta E_{\mathrm{IX}} = -\mathbf{pF}. \tag{2.17}$$

This energy reduction is called quantum confined Stark effect [Miller et al. 1984; Miller et al. 1985; Charbonneau et al. 1988; Chen et al. 1987; Andrews et al. 1988]. The energy shift ΔE_{IX} relative to the intra well exciton due to the tilted band structure is illustrated in Fig. 2.4(b). In the experiments a linear red shift with increasing electric field is observed (see Fig. 5.1 and Fig. 8.1(c)). This is remarkable and means that the electron-hole separation is independent of the electric field whereas the overlap integral changes dramatically (see Fig. 2.6(a)). The displacement between electron and hole is comparable to the center-to-center distance of the coupled quantum wells. For very small electric fields near flat band (see Fig. 2.5(a)) it is expected that the electron-hole separation is proportional to the applied electric field. The dipole moment reliant on the electric field causes a quadratic behavior of the exciton energy shift. The Quantum confined Stark effect allows the modification of the uncharged exciton energy by changing the bias used to create the electric field. A lateral variation of the electric field makes it possible to build a potential landscape $V_{\mathrm{IX}}(x, y)$ for dipolar excitons (see Section 2.8). The indirect excitons will accumulate on the place of the highest electric field. Therefore they are also called high field seekers.

2.6.2. Dipolar exciton interaction

The alignment of the dipolar excitons in an uniform direction perpendicular to the quantum well plane (see Fig. 2.8) causes a strong repulsion between the excitons with an interaction energy of

$$W = \frac{p^2}{\epsilon r_{\mathrm{IX-IX}}^3} \tag{2.18}$$

where $r_{\mathrm{IX-IX}}$ is the lateral distance between the indirect excitons.

The repelling interactions between the excitons avoid the appearance of molecular biexcitons. Additionally, the formation of metallic electron-hole droplets is prevented [Zhu et al. 1995; Lozovik et al. 1999]. Therefore, the repulsive interaction is advantageous to realize a bosonic high density exciton ensemble. At low temperatures we expect that the strong dipolar interactions cause correlations between the excitons, which result in a spatially ordered arrangement of the dipoles comparable to a Wigner-crystal-like state (see Fig. 2.8) or a Wigner-glass [Aoki 1979; Yoshioka et al. 1990; Laikhtman et al. 2009].

2.6.3. Density effect

The repulsive dipole-dipole interaction increases the energy of indirect excitons (see Equation (2.18)). With increasing exciton density, for example due to stronger laser excitation, the exciton energy is blue shifted by the reduced $r_{\mathrm{IX-IX}}$. A second repulsive interaction that increases the exciton energy at higher densities is the phase-space filling effect with which the fermionic structure of the excitons starts to become important. Additionally, it is possible that with increasing exciton density the binding energy of the excitons is reduced so that the spectral energy of their photoluminescence is blue shifted. The enhancement of the exciton energy with growing exciton density is observed in single and coupled double quantum wells [Peyghambarian et al. 1984; Negoita et al. 2000; Schinner et al. 2011a]. The blue shift of the luminescence energy is accompanied by a broadening of the emission line due to increased exciton scattering (see Section 2.5) [Vörös et al. 2009b].

In a strong simplified approach the exciton-exciton interaction can be electrostatically described with the so-called plate capacitor model. The spatially separated electron and hole layers create a depolarizing electric field, which reduces the external applied electric field. The decreasing effective electric field seen by the indirect excitons reduces the quantum confined Stark effect and causes a blue shift of the emission line. The measurement of the spectral shift provides a possibility to get an experimental estimate of the exciton density n. The assumption is that the blue shift ΔE is proportional to the exciton density n

$$\Delta E = \frac{4\pi e^2 d}{\epsilon} n \tag{2.19}$$

where d is the electron-hole separation and ϵ the dielectric constant. For small densities this relation underestimates the real exciton density up to a factor of 10. A modified conversion formula from blue shift to density is detailed discussed in Section 6.6.

From the dipole interaction described in Equation (2.19) a dipole repulsion force can be extracted given by

$$F_{\mathrm{dipol}}(\mathbf{r}) = -\frac{4\pi e^2 d}{\epsilon} \nabla n(\mathbf{r}) \tag{2.20}$$

At an inhomogeneous density distribution $n(\mathbf{r})$ this repulsion force causes strong exciton drift over long distances [Vörös et al. 2005; Gärtner et al. 2007; Vögele et al. 2009a].

2.7. Excitons in a magnetic field

The magnetic field behavior of dipolar excitons is nontrivial and discussed in many theoretical papers [Lozovik et al. 1997; Govorov et al. 1998; Lozovik et al. 2002a; Morales et al. 2008]. In this section the case of non-interacting and spinless excitons is discussed when a magnetic field is applied perpendicular to the quantum well plane. The Hamiltonian in the effective mass approximation can be written in the following way

$$H = \frac{1}{2m_e}(\hat{\mathbf{p}}_e + \frac{e}{c}\mathbf{A}_e)^2 + \frac{1}{2m_h}(\hat{\mathbf{p}}_h + \frac{e}{c}\mathbf{A}_h)^2 + V_e^z + V_h^z - \frac{e}{\epsilon\sqrt{d^2 + (r_e - r_h)^2}} - e\mathbf{dF}, \quad (2.21)$$

where $m_{e,h}$ is the effective electron or hole mass. The first and second term in Equation (2.21) describes the kinetic energy with a generalized momentum where $\hat{\mathbf{p}}_{e,h} = \frac{\hbar}{i}\nabla_{e,h}$ is the momentum operator and $\mathbf{A}_{e,h}$ is the vector potential for the electron and hole. The in-plane solution of the first both terms of the Hamiltonian (2.21) in the magnetic field results in a Landau level quantization of the charge carriers

$$\Delta E(B) = \hbar\omega_\mathrm{c}\left(n_\mathrm{LL} + \frac{1}{2}\right) \quad (2.22)$$

where $\hbar\omega_\mathrm{c}$ is the cyclotron energy with $\omega_\mathrm{c} = \frac{eB}{c\mu}$ and μ is the reduced mass of the exciton given by

$$\mu = \left(\frac{1}{m_e} + \frac{1}{m_h}\right)^{-1}. \quad (2.23)$$

A Landau level is $n^\mathrm{L} = 2\frac{eB}{h}$ times degenerate and the so-called filling factor, is given by

$$\nu = \frac{nh}{eB} \quad (2.24)$$

where n is the total density.

The next two terms in the Hamiltonian (2.21) are the confinement potentials of the electron and hole in the z direction of the coupled quantum wells which cause a quantum well width dependent increase of the exciton energy by E_qc due to the quantum confinement. The fifth term is the Coulomb interaction between the electron and hole where ϵ is the dielectric constant, d the electron-hole separation in z direction and $r_{e,h}$ are the lateral coordinates of the electron and hole. The bound exciton state shows a reduced energy due to the binding energy. The last term in Equation (2.21) describes the energy reduction of the dipolar excitons in the external electric field due to the quantum confined Stark effect.

For free charge carriers Landau level quantization is always dominant in the magnetic field in contrast to excitons where one can distinguish two cases as discussed below. For the excitonic behavior the strength of the magnetic field and the kinetic energy of the exciton are important.

2.7.1. Coulomb exciton

In the case of weak perpendicular magnetic field and small in-plane excitonic momentum the Coulomb interaction between the electron and hole dominates the excitonic binding. The exciton is a hydrogen-like bound state only slightly changed by the magnetic field and is called a Coulomb exciton. The applied magnetic field can be treated as a weak perturbation which causes a diamagnetic shift ΔE_{dia} of the exciton energy [Bugajski et al. 1986; Stern et al. 2008a]

$$\Delta E_{\mathrm{dia}} = \frac{e^2 a_{\mathrm{B}}^2}{8\mu c^2} B^2. \tag{2.25}$$

This energy blue shift shows a quadratic dependence on the magnetic field, which is characteristic for localized excitons. From the diamagnetic shift it is possible to extract an effective Bohr radius a_{B}. Additionally, the diamagnetic behavior can be used to control the exciton in-plane dynamics and build exciton traps, because the excitons are rejected from areas of high magnetic field [Christianen et al. 1998]. In electrostatic trapping devices (see next Section 2.8) a supplementary applied magnetic field suppresses exciton ionization and stabilizes excitons [Govorov et al. 1998].

2.7.2. Magneto exciton

On the other hand, in the case of high excitonic momentum even at low magnetic field or at high magnetic flux density the hydrogen exciton transforms in a magneto exciton. In this limit the excitonic behavior is dominated by the cyclotron energy and Landau level quantization, being much larger than the Coulomb binding energy. The energy shift is determined by the Landau levels (see Equation (2.22)) and therefore linear in magnetic field. The magnetic field additionally increases the excitonic binding energy of direct $E_{\mathrm{B}}^{\mathrm{DX}}$and indirect $E_{\mathrm{B}}^{\mathrm{IX}}$ excitons

$$E_{\mathrm{B}}^{\mathrm{DX}} \propto \frac{1}{l_B} \propto \sqrt{B} \tag{2.26}$$

$$E_{\mathrm{B}}^{\mathrm{IX}} \propto \frac{1}{\sqrt{l_B^2 + d^2}} \tag{2.27}$$

where $l_B = \sqrt{\frac{\hbar c}{eB}}$ is the magnetic length. For indirect excitons the electron and hole layer separation d has to be considered.

The internal structure of the magneto exciton is dominated by the individual interaction of counter charged electron and hole with the magnetic field. The in-plane momentum P of the exciton in combination with the applied perpendicular magnetic field B causes a Lorentz force which results in an in-plane separation $< r >$ of the electron and hole of $< r >= \frac{P}{eB}$.

2.8. Electrostatic traps for dipolar excitons

As discussed in Section 2.2, it is absolutely essential to trap the excitonic ensemble in order to achieve a quantum phase transition to a Bose-Einstein condensate [Hohenberg 1967]. Therefore it is necessary to manage the exciton in-plane dynamics and control the exciton expansion. Furthermore it is interesting for applications in optoelectronic devices to control the lateral exciton drift [High et al. 2008].

The ideal trap is characterized by a long-lasting effective confinement of a thermalized excitonic ensemble, a certain tunability and a parabolic trap profile. The best way to realize such a trap is to use the in-plane variation of the local Stark electric field $F_z(x, y)$ to create a potential landscape $V_{\mathrm{IX}}(x, y)$ for the dipolar excitons. Thereby the quantum confined Stark effect (see Section 2.6.1) is used to laterally change the exciton energy and the excitons accumulate in the region of highest electric field perpendicular to the quantum well plane. The in-plane variation of the electric field $F_z(x, y)$ is achieved by differently biased surface gates. Other possibilities to obtain an excitonic confinement are: strain-induced traps [Trauernicht et al. 1983; Kash et al. 1988; Negoita et al. 1999], magnetic traps [Christianen et al. 1998] and silicon-dioxide based traps [Gärtner et al. 2007; Vögele et al. 2009a]. But these traps are not as universal as the reported electrostatic traps [Zimmermann et al. 1997; Zimmermann et al. 1998; Rapaport et al. 2005; Hammack et al. 2006a; Chen et al. 2006; High et al. 2009b; Schinner et al. 2011a; Kowalik-Seidl et al. 2012].

Electrostatic traps are characterized by a very high versatility. The lithographic lateral structuring allows nearly arbitrarily shaped potential landscapes for the indirect excitons. Furthermore the gate defined trapping configurations are characterized by a high in-situ tuneability by simply varying the applied gate-voltages. Additionally, it is possible to change the gate-potentials on a time scale, which is short compared to the excitonic lifetime [High et al. 2007]. This allows the creation of electrostatic traps where evaporative cooling is possible similar to atomic traps. The electrostatic trap has also an incorporated evaporative cooling because of the electric field dependence of the excitonic lifetime (see Fig. 2.6(a)). In areas with high excitonic energy and low electric field the excitons annihilate much faster than in the trap center with high electric field. To build high-quality traps it is necessary to prevent free surfaces with an undefined electric surface potential and avoid large in-plane electric fields ionizing the excitons. Therefore the position of the bilayer within the heterostructure and the thickness of the diode structure are important [Rapaport et al. 2005].

One of the simplest possible exciton traps is schematically shown in Fig. 2.9(a). The coupled double quantum wells are located in the middle between the grounded homogeneous back contact and the surface gates. The grounded guard gate surrounds the biased central circular trap gate. For this geometry it is possible to solve the Laplace equation inside the heterostructure. The result is cylindrically symmetric

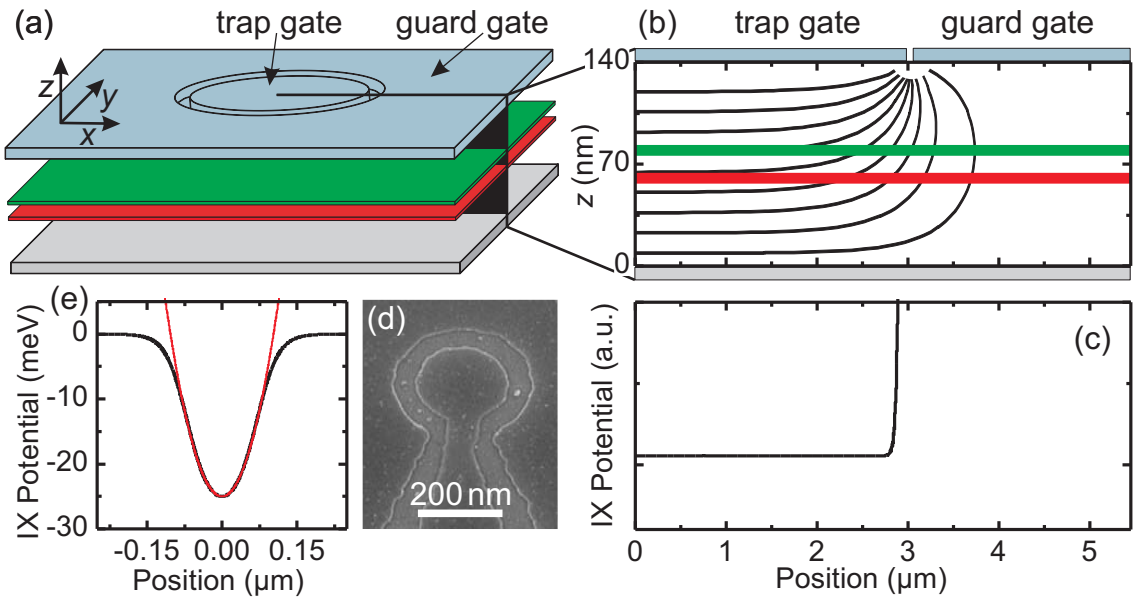

Figure 2.9.: **Electrostatic traps for dipolar excitons.** (a) Illustrates the bilayer heterostructure with two surface gates on top defining an electrostatic exciton trap. In (b) the calculated solution of the Laplace equation is shown in terms of equipotential-lines inside the heterostructure [the trap gate is biased, the guard gate and back contact are grounded]. (c) Illustrates the corresponding exciton confinement. The scanning electron microscope image in (d) displays the practical realization of such a circular exciton trap and (e) shows the resulting exciton trap potential.

and in Fig. 2.9(b) lines of equal potential are plotted for a trap with a trap gate radius of 3 μm. The electric field component F_z in the exciton plane perpendicularly oriented to the quantum well causes the confinement potential which is comparable to a pot with a flat bottom as shown in Fig. 2.9(c). For smaller trap gate radii as depicted in Fig. 2.9(d) the theoretically calculated exciton confinement potential is characterized by a parabolic trap shape as illustrated in Fig. 2.9(e). Note that these classical calculations neglect depletion of the background charges in the heterostructure and do not include screening by the presence of dipolar excitons. In the next chapter the heterostructure used for the experiments and the sample fabrication is described.

3. Sample fabrication

The samples used in this thesis are all fabricated in two steps. First a semiconductor heterostructure is grown providing an exciton confinement in growth direction. The result is a two-dimensional exciton system. Then the sample surface is laterally structured with top-gates via lithographic techniques to control the exciton in-plane dynamics. In the best case it is then possible to create a zero dimensional exciton confinement as shown in Chapter 7.

3.1. Heterostructure

The heterostructure is grown by molecular beam epitaxy. This is a crystal growth method where semiconductor films are deposited in ultra-high vacuum with atomic layer precision. The deposition of semiconductor materials with different band gap and similar lattice constant allows a structuring of a heterostructure in growth direction by band gap engineering. The energy bands line-up and the resulting band offset between the different semiconductor-materials are determined by the branching point energy [Tersoff 1984]. This crystal growth technique was developed in the 1970s simultaneously with the first prediction of an electron-hole bilayer system [Dingle et al. 1975; Lozovik et al. 1975]. The heterostructure used in this work is shown in Fig. 3.1 and for a detailed description of the layer structure see Appendix B.1. The heterostructures are provided by Andreas Wieck, University of Bochum and Dieter Schuh, University of Regensburg.

The origin for the sample growth is a both side polished GaAs substrate. The first functional layer is the silicon doped GaAs back contact, which is necessary to built a diode structure and therefore it will be contacted afterwards via ohmic contacts. In the middle of the heterostructure are the coupled double quantum wells. A 10 nm GaAs tunneling barrier separates the two 7 nm $In_{0.11}Ga_{0.89}As$ quantum wells. 5 nm GaAs ledges and thick AlGaAs blocking barriers surround the quantum well layers. The 5 nm GaAs spacer layer is grown to avoid an InGaAs-AlGaAs interface which would be very ragged and cause thereby strong roughness scattering of the excitons. The blocking barriers are grown to prevent a current flow through the heterostructure. The growth procedure is closed by a 5 nm GaAs capping layer, which protects the AlGaAs from oxidation and is important for the semiconductor-metal interface of the diode structure.

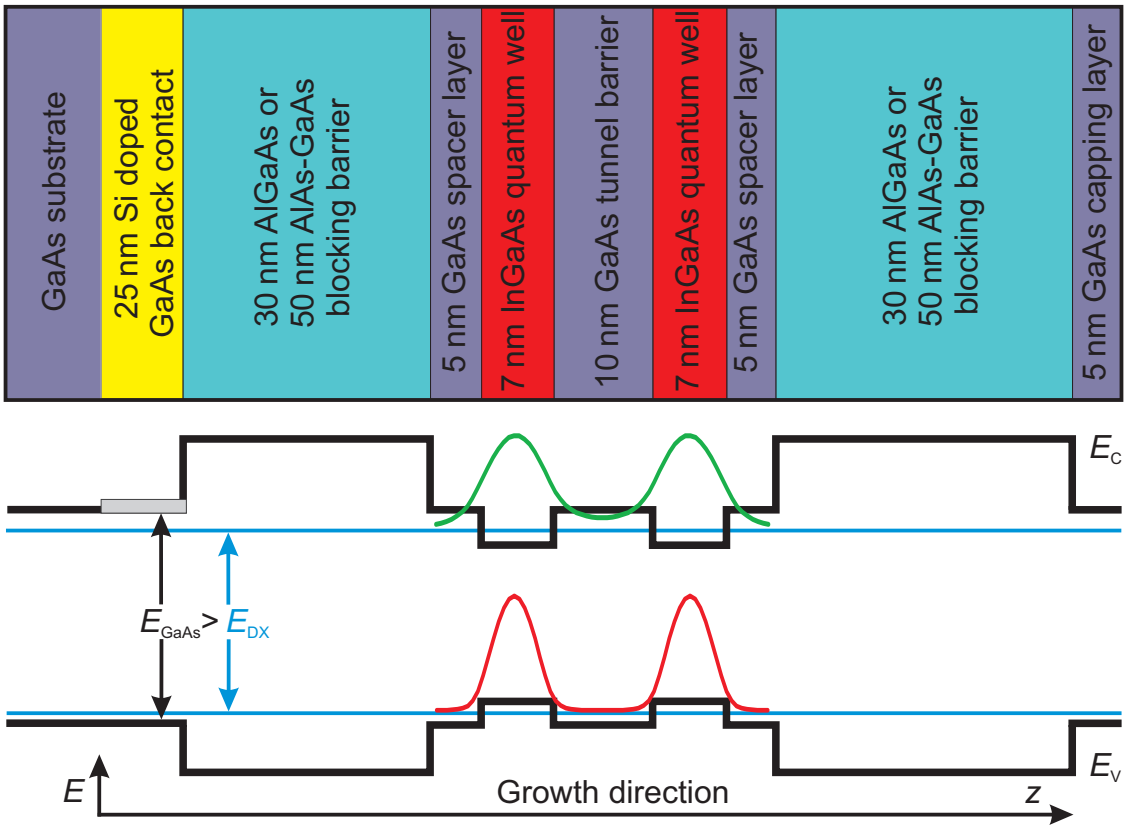

Figure 3.1.: **Layer structure of the coupled double quantum well samples.** It is illustrated the sequential arrangement of the different semiconductor layers and the resulting conduction and valence band edge leveling.

The previous investigated bilayer systems in our lab were based on GaAs-AlGaAs with GaAs quantum wells. The here introduced InGaAs quantum well samples have a few advantages over the former structures. The most important advantage is that the exciton energy in InGaAs quantum wells is below the absorption edge of GaAs (see Fig. 3.1). Therefore it is possible to perform transmission measurements, which allow introducing a new detection scheme (see next Chapter 4) where the photoluminescence light is collected in transmission. Another advantage is that one can use a pump-laser with an energy below the GaAs absorption edge. This avoids the excitation of electron-hole pairs in the GaAs capping layer and substrate, which can cause charge carrier accumulation, currents through the sample and unwanted photoluminescence from bulk GaAs excitons. Additionally, the possibility exists to resonantly excite excitons in the coupled quantum wells. This allows performing absorption experiments [Stallhofer, Markus 2009; Schubert, Enrico 2010] and minimizes the heat deposition in the heterostructure (see Section 6.4). The energy of the excitonic states in the InGaAs quantum wells is below the Fermi energy of the back contact. Therefore it is possible to fill via voltage tuning one of the quantum

wells with a two-dimensional electron system. This allows the investigation of the coupling between a Fermi sea and excitons (see Chapter 8). But to explore a pure bosonic system one should avoid these excess electrons. Another disadvantage is the ternary alloy InGaAs. The three-component semiconductor assists the formation of random disorder due to alloy fluctuations and a mismatch of the lattice constant. Therefore the indium concentration was kept as low as possible.

3.2. Device fabrication

The sample fabrication is performed in the clean room. There two optical lithography steps as well as two electron beam lithography steps are necessary. The fabrication of the sample starts with cleaving the wafer in small pieces of $4.5 \times 4.5\,\mathrm{mm}^2$. Afterwards, the sample surface has to be cleaned with solvents to remove all dirt. The complete sample preparation procedure and the corresponding parameters are described in Appendix B.2. Pictures of the device are shown in Fig. 3.2.

3.2.1. Lithographical device processing

For all optical lithography design steps the clean sample surface is spin coated with a light sensitive resist. In the following, the sample is baked on a hotplate to remove the solvent from the photo resist. In the next step, the sample is aligned and brought into contact with a shadow mask made of chrome coated glass. The areas of the sample exposed to ultraviolet light change their chemical properties. In the subsequent development process the illuminated regions of the photo resist are chemically removed and the structure of the mask is transferred to the sample surface.

In the first optical lithography step ohmic contacts are produced to connect the doped back contact. The ohmic contacts provide an electrically conducting connection between the sample surface and the back contact. Therefore, a mask with four rectangular apertures in each corner of the sample is used. After the development of the illuminated areas the chip is evaporated with an eutectic AuGe alloy. In the so-called liftoff process acetone is used to remove the resist and the excess metal layer on top of it. To create the electric connection to the back contact the sample is heated up in argon protective atmosphere and the AuGe partly diffuses into the heterostructure and forms the ohmic contacts. In the second optical lithography design step large scaled gate electrodes and alignment markers for the electron beam lithography are created. Large contact pads characterize the outer end of the gate electrodes (see Fig. 3.2(d), 3.2(e)). After development, a thin 5 nm Ti adhesion layer as well as a thick 90 nm Au layer are evaporated. The procedure is closed by the liftoff in warm acetone.

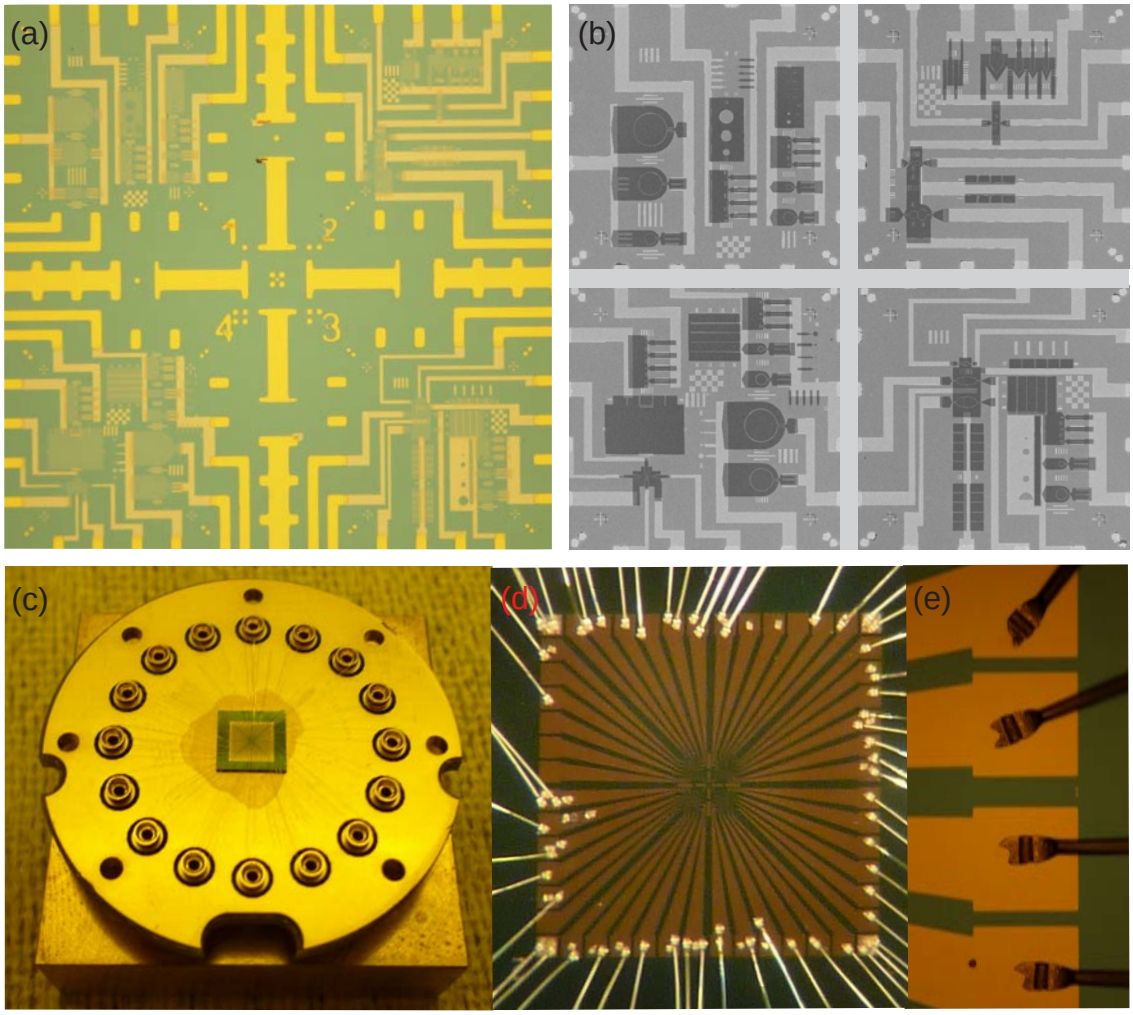

Figure 3.2.: **Pictures of the sample.** (a) Shows a light microscope picture of the four electron beam lithography write fields. (b) Displays scanning electron microscope pictures of the four patterned fields. The gold gate electrodes are light gray and the semitransparent titan gates are dark gray. (c) Shows the wire bonded chip glued on the sample holder. In (d) and (e) are illustrated the contact pads with the gold wires.

3.2.2. Electron beam lithography

The electron beam lithography uses the focused electron beam of a scanning electron microscope. Therefore it is possible to create nanostructures in the order of 50 nm of arbitrary geometry independent of a shadow mask with dimensions of the order 1 μm. Additionally, it is possible to align different lithography steps with highest accuracy. As resist for the electron beam lithography poly-methyl-methacrylate (PMMA) is spin-coated on the sample. In the exposed areas the high-energy electrons crack

the polymer chains in short fractions, which in the next step are dissolved in a developer. In the first electron beam lithography design step the gold gate electrodes are extended as fine gold gates and gold alignment markers are written for the orientation with the confocal microscope during the measurements as well as to align the second electron beam lithography step. In this step the semitransparent 5 nm thick Ti gates are fabricated, which define the potential landscape for the dipolar excitons.

3.2.3. Bonding

At the end of the chip processing, the sample is glued onto a newly designed chip carrier (see Fig. 3.2(c)). This is a crucial step to align the coordinate system of the lithography with the one of the confocal microscope. In the next step the contact pads of the sample are connected via wire bonding with a 25 μm gold wire to the contact pins of the sample holder (see Fig. 3.2). When the chip carrier is mounted in the confocal microscope, the pins are connected to the cryostat wiring.

4. Experimental setup

The dipolar exciton properties in the potential landscapes are investigated by means of optical spectroscopy. The transparency of the GaAs substrate of the heterostructure for the photoluminescence light of the quantum well excitons allows the introduction of a new detection scheme. Two low-temperature confocal microscopes are designed and homemade. Both are composed of two diffraction limited confocal objectives.

Fig. 4.1 shows the optical setup for time-averaged measurements. Here, three con-

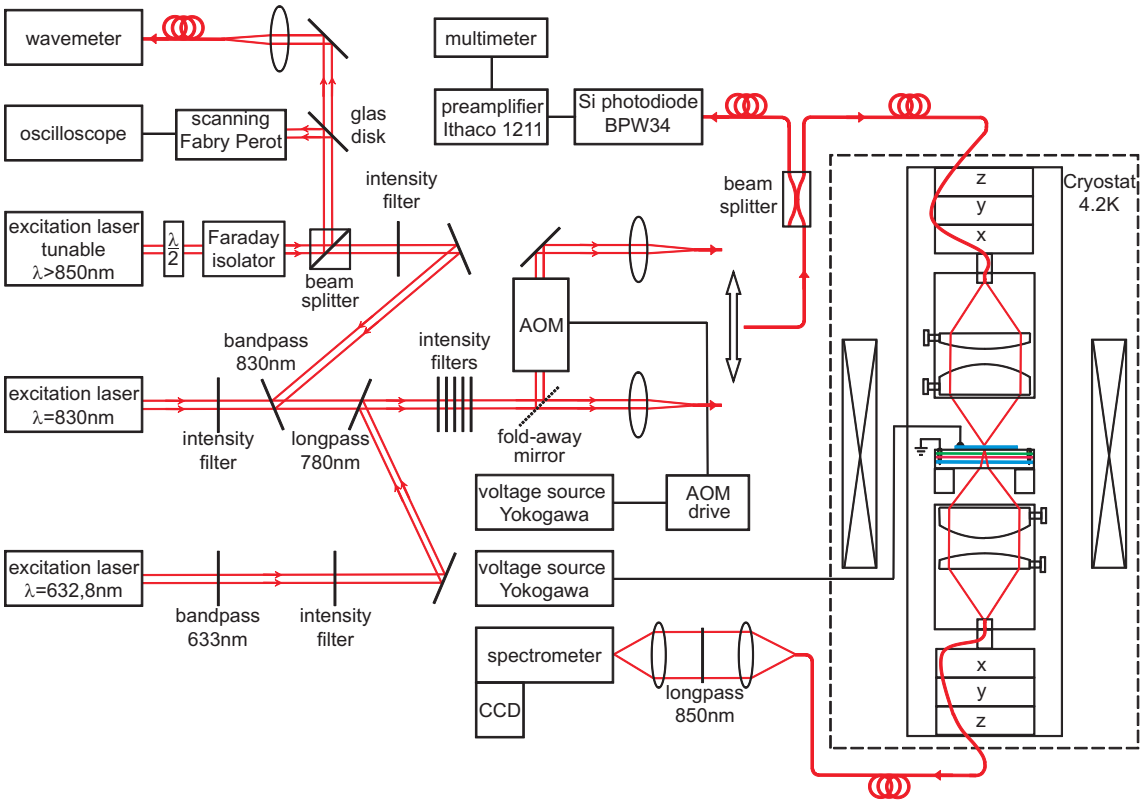

Figure 4.1.: **Experimental setup for continues wave experiments.** The schematic drawing shows the excitation and detection scheme used in the time-averaged measurements. Centerpiece of the experimental setup is the confocal microscope with two objectives.

tinues wave lasers are available. The main laser is a tunable diode laser, which covers exactly the energy spectrum of the dipolar excitons. This laser is actively power stabilized by an acousto-optical modulator, which is driven by a PID-controller. The used emission wavelength of the tunable laser is detected by a wavemeter. For non-resonant excitation below the GaAs absorption edge an 830 nm diode laser is used and above a helium-neon laser is available. All three lasers can be directly coupled into an optical fiber or via an acousto-optical modulator. The modulator allows varying the laser intensity by three orders of magnitude. Thereby it is easy to change the exciton density with the incident laser power. The laser light is guided into the cryogenic confocal microscope via a single mode optical fiber. A fiber beam splitter allows attaining a reference signal to determinate the laser power incident on the sample surface as a function of the used excitation laser wavelength. In the low-temperature microscope the upper confocal objective is used to focus the laser light diffraction limited on the quantum well plane exciting excitons. All excitons recombining in the focal area of the lower objective are detected in transmission if they are emitted in the solid angle of the objective below the sample. The collected photoluminescence light is coupled into a second single mode optical fiber, directing

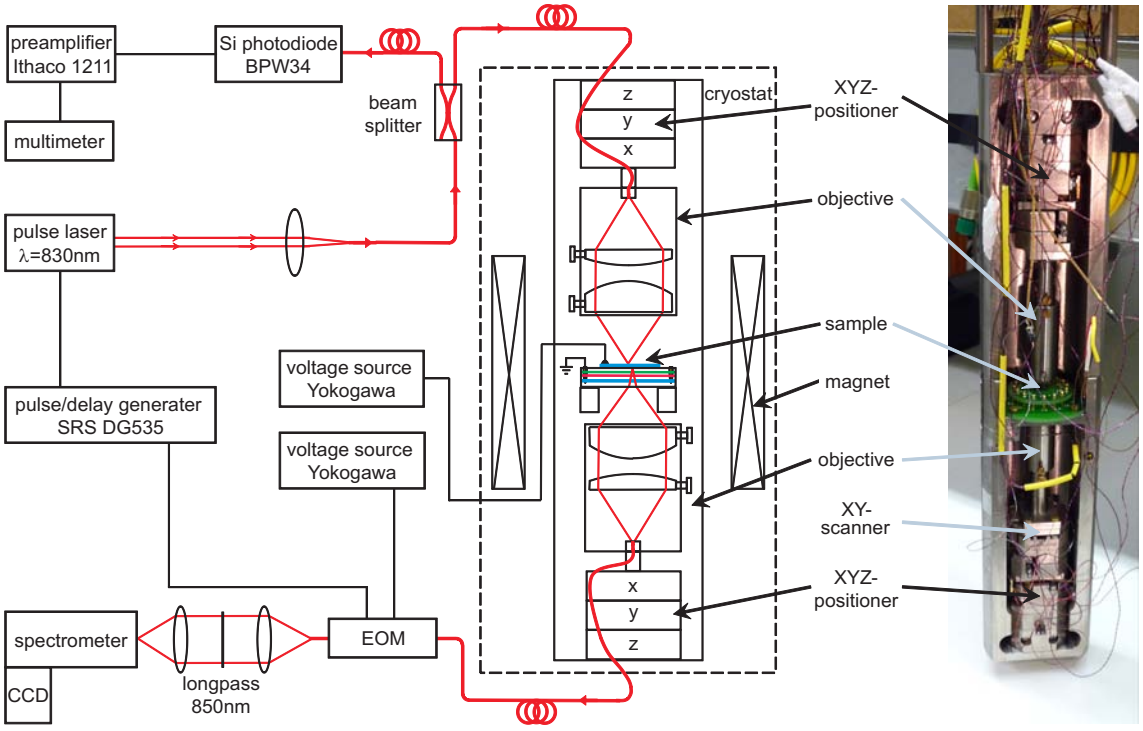

Figure 4.2.: **Experimental setup for time-resolved experiments.** The diagram illustrates excitation and detection scheme used in measurements with time-resolution. On the right-hand side is shown a photograph of the liquid helium cooled microscope.

the light outside the cryostat. At room temperature the photoluminescence can then be analyzed for example in a grating spectrometer.

To perform time-resolved measurements the setup illustrated in Fig. 4.2 is introduced. A pulse-delay generator controls a pulsed diode laser with 830 nm emission wavelength. Thereby the tunable laser pulse length varies the excited exciton density. The photoluminescence is again collected in transmission and guided via an optical fiber out of the cryostat. To achieve a spectrally resolved time-resolution a fast electro-optical lithium niobate modulator is used which is controlled via the pulse-delay generator. The electro-optical modulator allows the photoluminescence light to enter the spectrometer a certain delay time after the laser pulse for a defined time interval. The modulator is characterized by an extinction ration of 30 dB within 1 ns, which is fast compared to the excitonic lifetime of order 100 ns.

On the right-hand side of Fig. 4.2 a photograph of the 4 K microscope is displayed. This is a redesigned commercial microscope formerly used for self-assembled quan-

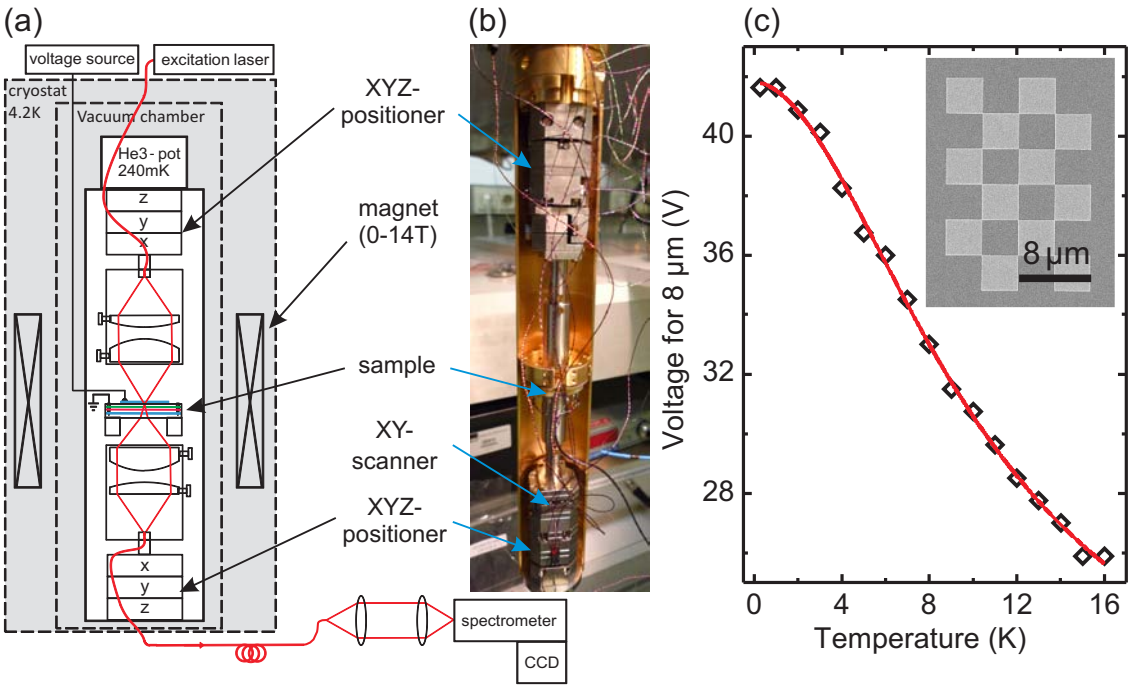

Figure 4.3.: **Cryogenic setup for millikelvin temperatures.** (a) Schematic diagram and (b) photograph of the low temperature microscope with two diffraction limited confocal objectives embedded in a ^{3}He refrigerator. In (c) is plotted the voltage which has to be applied to move with the $x-y$ piozo-scanner a distance of 8 μm as a function of the temperature, where 8 μm is the periodicity of the chessboard used for the calibration (see inset).

tum dot spectroscopy. Figure 4.3(a) shows a schematic drawing and Fig. 4.3(b) a photograph of the newly designed and homemade millikelvin microscope. The microscope is embedded in a ^{3}He refrigerator with a base temperature below 240 mK. The cryogenic setup exhibits an excellent long-time stability in position against temperature sweeps and magnetic field variations. Both objectives are diffraction limited and thus have a focus spot size with a diameter comparable to the wavelength and can be individually positioned with a low-temperature piezo-xyz-positioning unit [Högele et al. 2008]. The positioning works at temperatures down to 240 mK along all three space coordinates over millimeter distances and with a nanometer accuracy. In order to efficiently cool the device chip, it is mounted on a cold gold plate and bonded several times to a cold ground.

To obtain a spatially resolved image of the excitonic in-plane dynamic the scanning of the detection objective is necessary. Thereby a spatial resolution is achieved which is comparable to the wavelength of the detected photons, because any light emitted outside of the focus is not imaged into the detection fiber. To facilitate the spatially resolved measurements an additional $x-y$ piozo-scanner is mounted which allows to scan the detection objective over distance of 30 μm at 4 K. But this scanning range is strongly temperature dependent as shown in Fig. 4.3(c).

5. Electrostatic trapping of dipolar excitons

We report on photoluminescence experiments on spatially indirect excitons in an InGaAs coupled double quantum well device in which semitransparent gates are employed to tune the in-plane potential landscape. We introduce a new trapping configuration in which exciton generation is spatially separated from the excitonic trapping potential. Suitably biased gates control the flow of indirect dipolar excitons from the generation area to the electrostatically defined trap. Thus the trap is filled only with indirect excitons pre-cooled to the lattice temperature. Using a confocal microscope at liquid helium temperatures we map the in-plane distribution of excitons at various gate voltages and illumination conditions. Our small and strongly-confining traps with pre-cooled excitons demonstrate interesting many-body effects which can be interpreted in terms of the electrostatic screening, the Coulomb binding, and excitonic flows. Gate voltage dependencies of PL energy in our samples are not monotonic and can be explained by considering the non-linear exciton flows between the elements of our structure. At strong illumination hysteretic switching of the trapped exciton population reflects a nonlinear character of the self-consistent trapping potential. An unusual non-linear increase of the emission of the trap is likely coming from the many-body interactions in a dense exciton gas in the presence of a disorder potential at high light intensity. The new designs of electrostatic traps proposed and realized here allow for stronger confinements and lower temperatures and will be used to search for coherent phenomena in dense exciton gases.

5.1. Introduction

Spatially indirect excitons (IX) are bound electron-hole pairs consisting of an electron and a hole spatially separated in two adjacent quantum wells. The constituents of the exciton are fermions, but the bound state builds a boson. Bose-Einstein condensation (BEC) of excitons, though predicted by Keldysh and Kozlov decades ago [Keldysh et al. 1968], deserves further experimental exploration beyond recent experiments [Yang et al. 2006; Gorbunov et al. 2006] reporting spatial coherence of indirect excitons in coupled quantum wells (CDQW). Such dipolar excitons form a

complicated bosonic system of dipolar and interacting quasiparticles with an inner structure and a tunable lifetime exposed to a disorder potential.

BEC has been observed in superconductors, superfluids and ultracold diluted atomic gases in the last century. More recently, condensation of non-equilibrium quasiparticles in solids, namely magnons [Demokritov et al. 2006] and exciton polaritons [Kasprzak et al. 2006; Deng et al. 2010] have been reported as other examples of BEC. To achieve a BEC of excitons confined in the 2D plane of the heterostructure, an efficient trapping of high exciton densities thermalized to cryogenic temperatures is required [Ketterle et al. 1996] [Petrov et al. 2000]. With different approaches such exciton traps have been realized within the last years. They include strain-induced traps [Trauernicht et al. 1983; Kash et al. 1988; Negoita et al. 1999], natural traps due to disorder in the QW plane [Butov et al. 2002], magnetic traps [Christianen et al. 1998], traps generated by surface acoustic waves [Stotz et al. 2005], and laser-induced trap [Hammack et al. 2006b]. The most promising and widely tunable exciton traps rely on the electrostatically induced quantum confined Stark effect (QCSE) [Zimmermann et al. 1997; Zimmermann et al. 1998; Huber et al. 1998; Rapaport et al. 2005; Timofeev et al. 2007; Hammack et al. 2006a; Chen et al. 2006; High et al. 2009a; High et al. 2009b]. They were realized in various geometries and with different trapping efficiencies. Excitonic traps can also combine the electrostatic confinement and the strain-induced localization. Such traps were realized using silicon dioxide [Gärtner et al. 2007]. They provide a strong confinement along the perimeter around a SiO_2 patch and allow the exciton gas a one dimensional expansion over very long distances [Vögele et al. 2009a].

Here, we utilize a novel trap configuration in which the exciton generation is separated spatially far from the trapping potential and the confinement potential of the trap can be tuned widely with independently biased gates. Thus the trap is filled only with indirect excitons, pre-cooled to the lattice temperature and acquiring only a small well-controlled excess energy when entering the trap. This is in contrast to the majority of traps previously realized. Using spatially resolved photoluminescence (PL) we demonstrate the operating principle. We are able to fully control the in-plane exciton gas dynamics by suitably chosen voltages applied to the gates. We report how each gate influences the exciton behavior when the applied bias is changed. Additionally, it is possible to use a nonlinear trapping configuration to switch the exciton population and we present the characteristics of switching the IX flow. Furthermore, we observe and interpret an unexpected nonlinear increase of the PL intensity with the trapped IX density.

5.2. Spatially indirect excitons in voltage-tuned Coupled Double Quantum Wells

In our experiments on spatially indirect excitons we employ double quantum wells embedded within a field-effect tunable diode structure. A schematic of the band diagram is displayed in Fig. 5.1(a). Two narrow $In_{0.11}Ga_{0.89}As$ quantum wells, separated by a center to center distance d comparable to the excitonic Bohr radius $a_B \approx 20\,nm$, are embedded between an n-doped GaAs backcontact and a semi-transparent gate electrode. Without bias, mid-gap states at the surface of the GaAs-based heterostructure are the cause of a built-in electric field perpendicular to the CDQW plane, which raises the conduction band energy at the heterojunction-gate interface by about 0.7 eV, half the band gap of GaAs. With laser illumination at an energy above the band gap of GaAs, we create electron-hole pairs which relax via optical and acoustic phonon emission on a sub-nanosecond timescale to form both direct excitons (DX) within one of the quantum wells as well as spatially indirect excitons in which the electron and hole are separated by a distance of about the center to center distance of the DQW [Damen et al. 1990; Gulia et al. 1997; Hammack et al. 2009].Whereas the direct excitons recombine on a nanoseconds time scale [Feldmann et al. 1987], the indirect excitons exhibit lifetimes up to microseconds [Vörös et al. 2009b] which are determined by the spatial overlap of the electron and hole wavefunction. The binding energy of the indirect exciton is dominated by the DQW distance d and at $d \sim a_B$ is only weakly dependent on the wavefunction overlap [Szymanska et al. 2003]. The IX form dipoles with dipole moment $p = ed$ oriented perpendicular to the QW plane. As long as their in-plane separation $l = \frac{1}{\sqrt{n_{IX}}}$, where n_{IX} denotes the excitonic density, is larger than a_B, their dipolar repulsion prevents a Mott-transition to a metallic electron-hole double layer plasma [Stern et al. 2008a]. Since the recombination lifetime of the IX is significantly longer than the energy relaxation time to the excitonic ground state, the IX are likely to cool down to lattice temperature before recombining. This makes them particularly suitable for studies aimed at BEC.

The motion of IX within the QW plane is driven by gradients of both, the effective excitonic potential V_{IX} and density n_{IX} and, furthermore, by dipolar repulsion forces between excitons. The potential V_{IX} is formed by the biased gates and also includes a disorder component. To aim for the excitonic BEC it is necessary to create traps within the QW plane to spatially confine excitons. We employ the easy voltage tunability of the quantum-confined Stark effect to create a landscape for the in-plane excitonic potential that guides IX to a tunable trap, conceptually similar to what is employed in BEC of atomic systems. The QCSE causes a red-shift of the excitonic energy of $\Delta E_{IX} = -pF$, where F is the effective electric field perpendicular to the QW plane. At sufficiently low n_{IX} and for a large diameter gate with $D \gg d$, this is determined solely by the capacitance of the field-effect

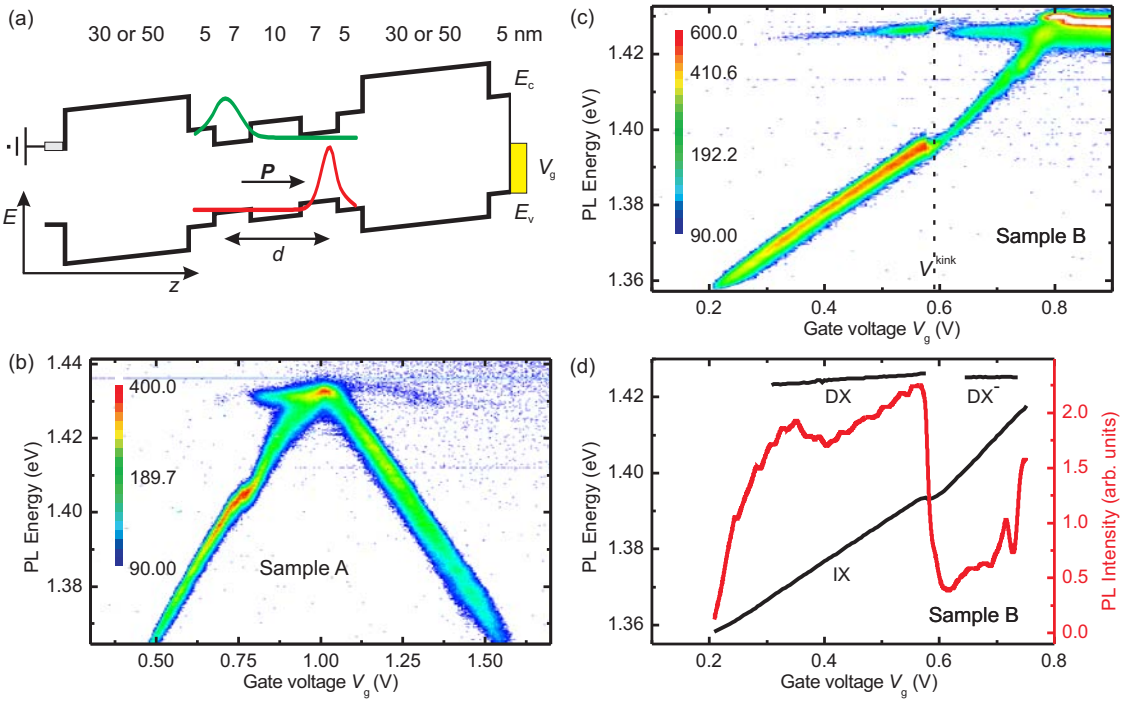

Figure 5.1.: (a) Schematic of the CDQW bandgap within a field-effect device with numbers indicating the layer thickness of the InGaAs QWs, the GaAs spacers, and the AlGaAs barriers, respectively. E_c and E_v denote the conduction and valence band edge, respectively. (b) PL measurement of the QCSE of sample A and sample B (c) with a homogeneous unstructured gate. In (b) and (c), the PL intensity is displayed in a logarithmic color scale and plotted as function of the PL energy and the applied bias V_g. In (d), the PL peak energies of direct (DX) and spatially indirect (IX) excitons (black, left axis) and the integrated intensity of the IX PL (red, right axis) of the measurement (c) are shown as a function of the gate voltage V_g.

device and is $F = \frac{1}{l_0}(V_g - V_{FB})$, where V_{FB} corresponds to the flat-band voltage, at which the external voltage compensates the built-in electric field, and l_0 denotes the lever arm, i.e., the distance between the gate and the embedded n-doped back contact. In the case of high IX densities, especially for trapped IX, a large ensemble of IX partially screens the externally applied electric field via their dipole interaction. The consequence is a blueshift ΔE of the IX energy, because the effective electric field is reduced. A different way to understand this blueshift is the IX-IX interaction. The IX gas influences the V_{IX} seen by the individual IX at a constant gate voltage V_g. For not too small IX densities n_{IX}, it is possible to well approximate

$$n_{IX} = \frac{\epsilon_0 \epsilon \Delta E}{e^2 d} \tag{5.1}$$

with the measured blueshift ΔE and $\epsilon_0\epsilon$ are the vacuum and relative dielectric constants respectively [Schindler et al. 2008]. This linear relation is likely to underestimate the total IX density by about $2\times10^{10}\frac{1}{cm^2}$ as discussed in more detail in Ref [Ivanov et al. 2010].

In the following we discuss the QCSE for a large area homogeneous gate observed in our $In_xGa_{1-x}As$ CDQW. The heterostructures employed are a CDQW field-effect device with an n-doped back contact grown by molecular beam epitaxy on a GaAs substrate polished on both sides. The two InGaAs quantum wells with 7 nm width are separated by a 10 nm GaAs tunnel barrier. The active layer is surrounded by two symmetric spacer layers [see Fig. 5.1(b)]. In sample A we used 30 nm AlGaAs and in sample B 50 nm thick GaAs-AlAs short period superlattices (SPS) as spacers (see Section 3.1).

Figure 5.1(b) shows the QCSE of sample A under a homogeneous gate. Plotted is the PL intensity in a logarithmic color scale as a function of the PL energy and applied gate voltage V_g. The PL is measured at a bath temperature of 4 K in the focus of the exciton generation with a 633 nm (1.959 eV) pump laser operating at power $P_{laser} = 80\,nW$. Fig. 5.1(c) show a comparable measurement on sample B. For a more quantitative analysis Fig. 5.1(d) displays the data of Fig. 5.1(c), giving both the PL peak energies of IX and DX (black, left-hand axis) and integrated intensity (red, right-hand axis) of the IX PL as a function of gate voltage V_g. At flat band, when the electrical field in the field-effect device vanishes, the electronic ground state of the InGaAs DQW is below the chemical potential of the back contact. At the gate voltage V_{kink} at which the electron ground state of the IX in the lower QW coincides with the Fermi energy of the back contact, the linear QCSE shows a kink. At voltage $V_g < V_{kink}$, the IX PL energy is blueshifted and the IX PL intensity shows a steep increase [see red trace in Fig. 5.1(d)]. In sample A with barriers on both sides of the CDQW made of $Al_xGa_{1-x}As$ ($x = 0.42$) the QCSE is observable for voltage V_g both below and above V_{FB} [Fig. 5.1(b)]. In sample B where the alloy is replaced by a SPS barrier as described above, charge storage in the QW under illumination prevents the observation of the QCSE $V_g > V_{FB}$, because the

externally applied electric field is completely screened. Both samples show also a weak but discernible PL of direct excitons. In sample B and at $V_g > V^{kink}$, at which the QW electronic ground state is below Fermi energy of the back contact, we see PL of trion excitons. The trion is a negatively charged DX^- caused by the free electrons stored in the QW when $V_g > V^{kink}$ (for more details see Chapter 8). As expected the DX^- is observed at lower energy, than the DX and found to be independent of V_g at $V_g > V^{kink}$. In contrast, for $V_g < V^{kink}$, the direct exciton PL energy shows a redshift with increased electric field of 11 $\frac{meV}{V}$. On sample A, with AlGaAs alloy barriers, we observe a weak direct exciton PL, but we are unable to detect PL from DX^- at any laser power and excitation wavelength (830 nm, 808 nm and 633 nm). We interpret the different behavior of the two heterostructures by charge storage in sample B. Whenever the electronic ground state in the CDQW drops below the Fermi energy of the back contact, electrons can be collected in the CDQW. We then observe the trion formation and screening of the gate-induced field prevents a finite QCSE for $V_g \geq V_{FB}$.

The trap discussed in the next section is strongly influenced by the kink in the QCSE at $V_g = V^{kink}$. For the trap functionality, IX diffusion is important and depends critically on the gate voltage V_g. Therefore we investigate the IX diffusion on a large homogenous gate. We generate IX in the focus of a 830 nm (1.494 eV) pump laser (9 μW). With spatially resolved PL measurements (not shown here) we find that for a gate voltage $V_g = 0.60\,V > V^{kink}$, the IX intensity is halved after 9 μm where as for $V_g = 0.50\,V < V^{kink}$ the IX intensity is halved after 24 μm. This indicates a rather sudden increase of the lifetime of IX at $V_g \leq V^{kink}$. Correspondingly, we see in Fig. 5.1(d) a strong increase in the IX PL intensity and IX density.

5.3. Spatially resolved photoluminescence from a chute trap

By a lateral modulation of the electric field applied perpendicular to the quantum well plane it is possible to create an arbitrary potential landscape for (indirect) excitons. Using adequate gate geometries and applied voltages it is possible to gain full control over the exciton in-plane dynamics. To achieve a perfect, exciton trapping the location of the DQW inside the heterostructure is important [Rapaport et al. 2005]. We have positioned the DQW in the middle of the field-effect device, because of the exponential decay of the Fourier components of the in-plane potential with increasing distance from surface gates defining the trap geometry. We use sample B with 50 nm GaAs-AlAs SPS barriers to build traps. The back contact is contacted by an ohmic contact and the surface gates are laterally patterned using *e*-beam lithography. The GaAs substrate is transparent for the CDQW PL light of the InGaAs QWs because the corresponding photon energy is below the GaAs

band gap. For our spatially resolved studies we use a confocal microscope with two objectives operating at liquid helium temperatures [Högele et al. 2008]. The objective on top of the sample is used to excite IX with 1.494 eV (830 nm) laser energy. The second objective below the sample is used to collect the PL light in transmission and analyze it in a spectrometer. Both objectives are diffraction limited and thus have a focus spot size with a diameter comparable to the wavelength and can be individually positioned with piezo actuators. Additionally, it is possible to apply magnetic fields up to 14 T perpendicular to the QW plane.

With the aim of studying the PL of fully confined IX in thermal equilibrium with the lattice and without the perturbation of emission by DX and impurity transitions generated in the focus area of the incident laser radiation, we developed a chute like trapping configuration displayed in Fig. 5.2(b). It has three gates with a circular gate with bias V_T defining a trap for IX, a slide gate with bias V_S on which we optically generate electron-hole pairs as indicated by the red spot in Fig. 5.2(b), and an outside surrounding guard like gate with bias V_G which defines the excitonic confining potential in the area surrounding the trap and slide. The semitransparent gates are 6 nm thick evaporated Ti films and are separated by narrow ungated slits, visible as long gray lines in Fig. 5.2(b) which are only about 100 nm wide. They are narrow to prevent ill-defined potentials which are caused by charges on open GaAs surfaces and can form barriers preventing exciton transport from, e.g. the slide gate to the trap gate.

Figure 5.2(c) shows a schematic sketch of the exciton potential landscape V_IX along the x-direction of the chute trap when $V_\mathrm{T} < V_\mathrm{S} < V_\mathrm{G}$. With illumination on the slide gate, IX generated in the laser focus are expanding on the slide driven by diffusion and dipolar repulsion and are attracted by the energetically deeper exciton potential under the suitably biased trap gate. With suitable bias, the device acts like a chute which transports IX from the point of generation into the trap with the latter essentially not exposed to electron-hole generating radiation by virtue of the two separate confocal optics employed in our low temperature microscope.

Figure 5.2(d) illustrates the corresponding energy landscape for the electron and hole states forming the indirect exciton in the InGaAs DQW. Note that the trapping potential in this bias configuration $V_\mathrm{T} < V_\mathrm{S} < V_\mathrm{G}$ only is effective for IX. The potential step at the trap edge can only be overcome by bound indirect excitons. Direct excitons are likely to recombine before reaching the trap and unbound electrons are repelled from the trap as illustrated in Fig. 5.2(d).

Spatially and energetically resolved PL images obtained with the collection objective moving along y and x directions, are displayed in Figs. 5.2(a) and Fig. 5.2(e), respectively. Figure 5.2(a) plots the PL energy against y for a section through the middle of the trap at $x = 0$ with the PL intensity logarithmically color coded. The same data are illustrated in a pseudo-3D Fig. 5.2(f) with a linear PL intensity scale. The excitonic cloud is perfectly trapped and the spatial width of the PL intensity

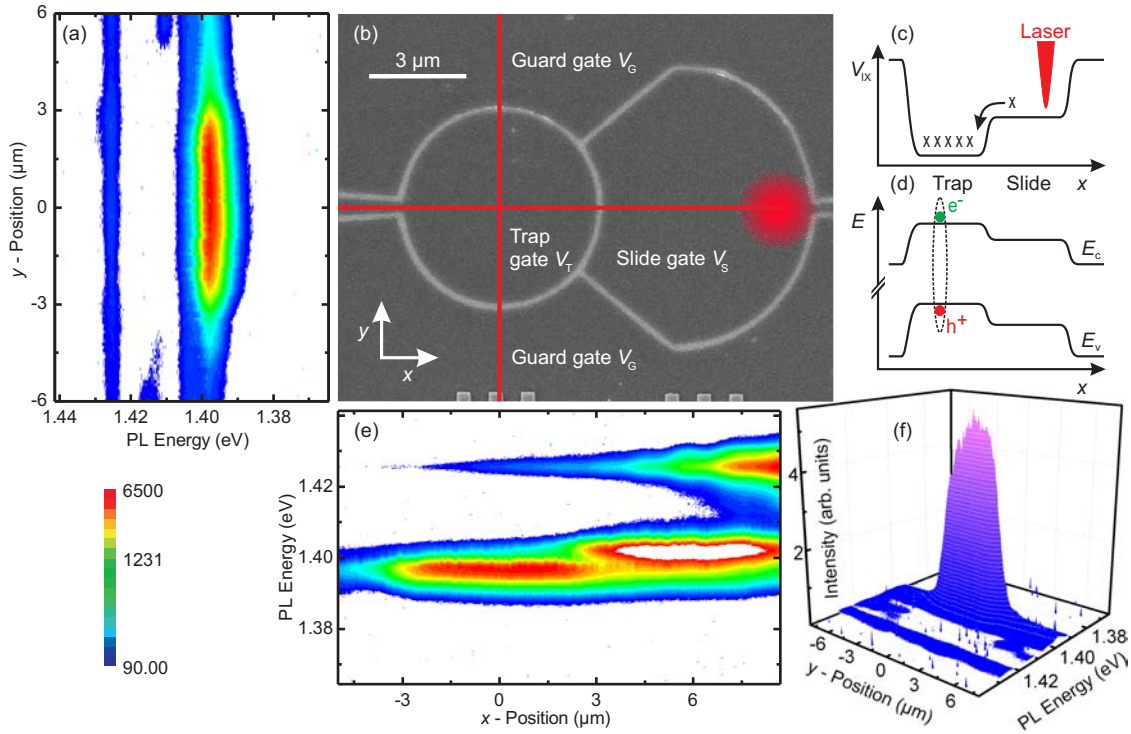

Figure 5.2.: The figure shows spatially and energy resolved measurements of the exciton expansion in the chute trap. In (a) and (e) cuts are shown of the PL intensity in a logarithmic color scale, given by the scale bar on the lower left, as a function of the position and PL energy. The data are measured along the red lines in the scanning electron micrograph shown in (b) of the trapping configuration which is composed of a slide, trap and guard gate. The pump laser position is fixed on the slide gate as indicated by the bright spot in (b). In (c) a schematic drawing of the exciton potential landscape of the chute trap is displayed. In (d) the corresponding energies of the conduction E_c and valence band edge E_v of the InGaAs CDQW are illustrated. The pseudo-3D picture (f) illustrates the same data as shown in (a) with a linear intensity axis. Here, the voltages applied are $V_G = 0.7\,V$ on the guard gate, V_T =0.35 V on the trap gate and $V_S = 0.45\,V$ on the slide gate. The temperature was 4 K and the laser power 8.0 μW at 1.494 eV energy.

at half maximum is 5.5 μm whereas the diameter of the trap gate is 6.0 μm. Solving the Laplace equation yields a box-like excitonic potential with 5.5 μm diameter, identical to the measured PL spatial width. In this trap configuration it is possible to realize ideal trapping and we are able to control the in-plane exciton dynamics.

Figure 5.2(e) displays the PL energy along x in a cut through the middle of the trap ($y = 0$) as indicated by the red line in Fig. 5.2(b) with the PL intensity again color coded logarithmically. The exciton generation by the pump laser occurs about 9 μm away from the trap center. In close vicinity to the pump laser focus, indirect excitons form within very short relaxation and cool-down times [Hammack et al. 2009]. Afterward, they diffuse into the energetically favored trapping area. Indirect excitons can easily transcend the gap between the slide and trap gate. As reflected in Fig. 5.2, the trap is homogeneously filled with indirect excitons, with no detectable leakage at the trap gate lead. The energetically highest PL signals in Figs. 5.2(a), 5.2(e), and 5.2(f) stem from direct excitons. Because of their short lifetime they decay within 1 μm distance from the excitation focus to half their intensity and are weakly detected by the collection objective. In the excitation focus, the indirect exciton recombination is strongly suppressed. This we interpret to result, at least partially, from the high kinetic energy and momentum of IX that prevents radiative recombination because of conservation laws [Hammack et al. 2009]. In contrast to observations in Ref [Stern et al. 2008b] we find no indications for the presence of an electron-hole plasma. We also observe in Figs. 5.2(a), 5.2(e), and 5.2(f) no PL from a DX^-.

5.4. Voltage-tunability of the excitonic potential of the chute trap

In the following we discuss how the trap can be tuned by the three gate voltages. In these experiments the pump laser (1.494 eV) is focused on the slide gate at a fixed position as indicated in Fig. 5.2(b). The PL is collected from the center of the trap gate.

5.4.1. Electrical currents

Before discussing the action of the gate voltages on the PL spectra we briefly want to discuss the characteristic dependencies of leakage currents in the device. We have measured the electrical current flow onto the gates and to the back contact. To generate electron-hole pairs we use an laser (1.494 eV) with a relatively high laser power of 28 μW focussed on the slide gate. All three gates are changed in parallel with a constant voltage offset to the trap gate of $V_S - V_T = 0.1$ V and $V_G - V_T = 0.2$ V.

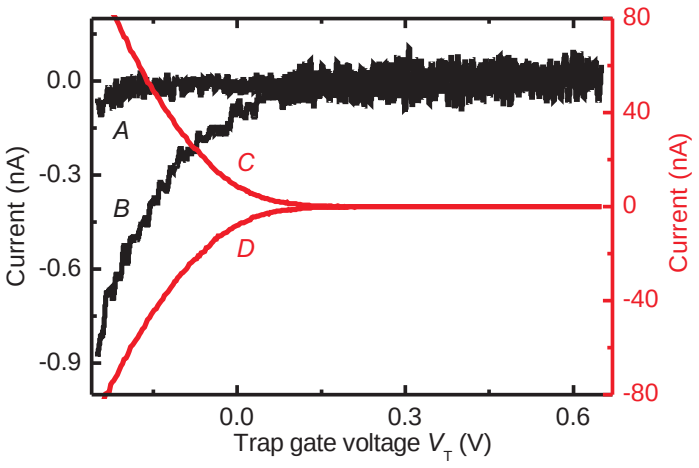

Figure 5.3.: Electrical current flow on the gates and to the back contact. The pump laser (1.494 eV) is fixed on the slide gate [as in Fig. 5.2(b)] with very high laser power 28 μW. All three gates are shifted parallel with a constant voltage offset to the trap gate of $V_S - V_T = 0.1\,V$ and $V_G - V_T = 0.2\,V$. Trace (A) is the current on the trap gate (black left-hand axis). (B) labels the current on the guard gate. On the right red current axis, the current of the back contact (C) and of the slide gate (D) is plotted.

The current I_T onto the trap gate (A, left black axis in Fig. 5.3) is always smaller than 100 pA. Trace (B) in Fig. 5.3 corresponds to a current I_G flowing onto the guard gate. For a smaller guard gate voltage $V_G < 0.25\,V$ I_G rises but remains very weak. On the slide gate we observe a strong current I_S for a slide gate voltage below $V_S < 0.2\,V$ (D and right red axis in Fig. 5.3). I_S also becomes the main contribution to the current out of the back contact I_B (C) in Fig. 5.3 with $I_B = I_S + I_T + I_G$. In the voltage range where we operate the trap and with the laser powers used (normally much less than 28 μW), there are no discernable currents between the gates. We thus can rely on the externally applied voltages fully reflecting the potentials applied at the gates.

5.4.2. Dependence on each gate voltage

Under variation of the trap gate voltage V_T at fixed $V_S = 0.5\,V$ and $V_G = 0.8\,V$ the IX change their energy and integrated intensity as displayed in Fig. 5.4(a). The excitons are generated on the slide gate and the PL is collected from the trap center. With decreasing V_T it is possible to increase the effective trap depth up to 30 meV. Raising V_T from 0.1 V to 0.6 V the PL energy in Fig. 5.4(a) increases faster than the linear QCSE as indicated by the dotted line which is an extension of a linear fit for $0.08\,V < V_T < 0.18\,V$ with a slope of 71 $\frac{meV}{V}$. This strong blueshift reflects

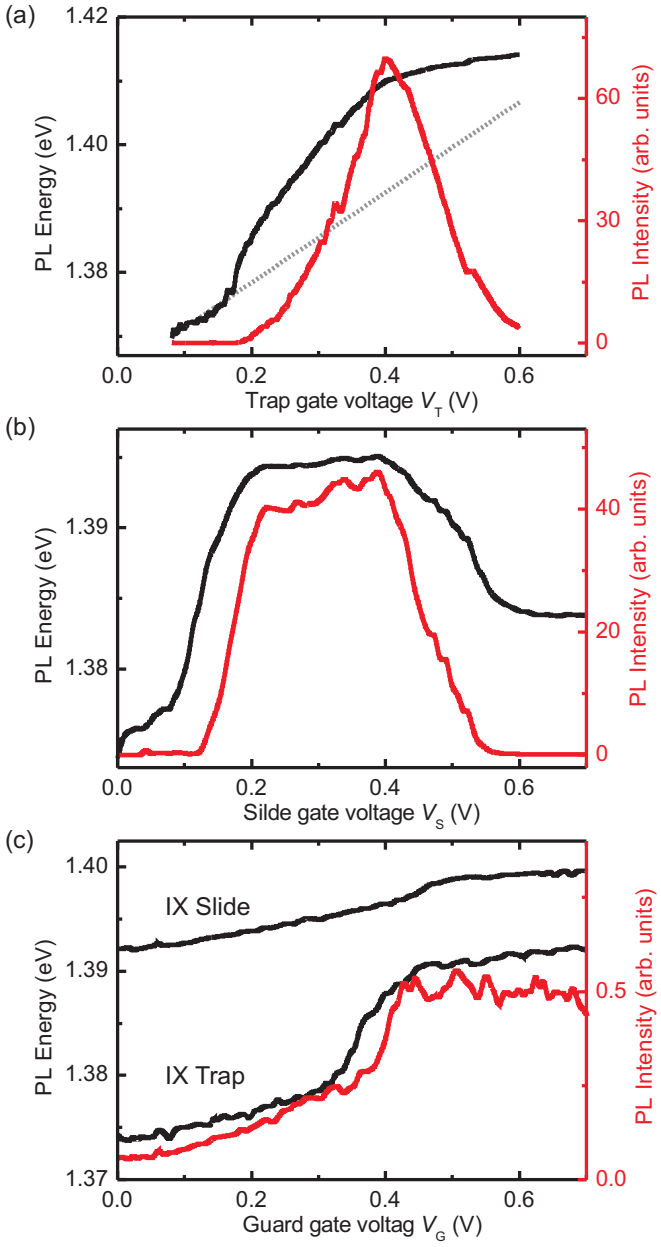

Figure 5.4.: The action of each gate voltage on the PL of IX in the trap is displayed. The excitons are generated at energy of 1.494 eV ($\lambda = 830$ nm) on the slide gate as in Fig. 5.2(b) and the PL is detected from the trap center. Plotted is the PL energy (black, left-hand side) and the integrated PL intensity of IX (red, right-hand side) as a function of the respective gate voltage with the other gates voltages constant. In (a) the V_T is varied at constant $V_G = 0.8$ V and $V_S = 0.5$ V (laser power 30 μW). In (b) the slide gate voltage V_S is varied at constant $V_G = 0.8$ V and $V_T = 0.35$ V (laser power 7 μW). In (c) is shown the dependence on the guard gate voltage V_G at constant $V_S = 0.45$ V and $V_T = 0.35$ V (laser power 7 μW). In (c), the IX PL energy from the slide gate area is plotted in addition.

the increasing exciton density in the trap. With increasing trap gate bias V_T, the PL intensity [red, right-hand side scale in Fig. 5.4(a)] rises from almost vanishing to a maximum value which is reached at $V_T \approx 0.4\,V$ where also the PL blueshift is maximal. Further increasing trap gate voltage yields an excitonic potential that is higher than the one under the slide gate and the PL intensity decreases strongly as IX no longer fill the trap. We name this configuration an antitrap.

Figure 5.4(b) shows the PL behavior of IX from the trap center with changing V_S at constant $V_T = 0.35\,V$, $V_G = 0.8\,V$. The PL energy for $V_S > 0.6\,V$ is constant. By varying the voltage on the slide gate the generation of IX on the slide gate is strongly enhanced for voltages $V_S < 0.6\,V < V^{kink}$ [see Fig. 5.1(c)], and the trap is effectively filled with excitons. For $0.15\,V \lesssim V_S \lesssim 0.6\,V$, the PL energy in the trap is blueshifted and the PL intensity enhanced. Further decreasing V_S results in an anti-trap and correspondingly causes the exciton density of IX in the trap to rapidly vanish.

Figure 5.4(c) displays the dependence of the IX PL from both the trap and slide area, on guard gate voltage V_G at fixed $V_T = 0.35\,V$ and $V_S = 0.45\,V$. Here, the PL energies from the slide (upper trace) and trap gate are plotted as functions of the guard gate voltage. In addition, it shows the PL intensity from the trap center in red as given by the right-hand side of Fig. 5.4(c). As the guard gate voltage V_G is reduced from 0.7 V to 0.5 V, the exciton energy and the corresponding density below the slide and trap gate are essentially constant. Once V_G drops below V_S, IX preferentially flow from the slide to the guard gate. This results in a reduction of the exciton energy and density on the slide gate. Consequently, the reduced confinement at around $V_G \simeq 0.2\,V$ causes a redshift of the trap PL of about 15 meV, corresponding to a drop in density of roughly $7{\times}10^{10}\frac{1}{cm^2}$. In comparison, one observes a much weaker decrease of the PL energy on the slide gate with decreasing V_G, reflecting the nearly constant density in the area where excitons are generated. The influence of the guard gate demonstrates that the trap design is well suited to collect and confine exciton densities up to high densities of order $10^{11}\frac{1}{cm^2}$.

Another experimental finding that characterizes the function of the trap design is summarized in Fig. 5.5. Here, the trap gate voltage V_T is changed simultaneously with V_G and V_S with the offset $\Delta V = V_S - V_T$ as parameter whereas $V_G - V_S = 0.2\,V$ is kept constant. In Fig. 5.5(a) the variation of the PL energy with V_T is logarithmically color coded for the case $\Delta V = 0.25\,V$. The energetically lowest PL branch results from the trap. For trap voltages larger than $V_T > 0.33\,V$ the PL intensity is weak. With decreasing trap gate voltage V_T, the PL energy shows a strong blueshift while the PL intensity grows abruptly. This reflects the sudden enhancement of the exciton density at $V_T = 0.33\,V$. At this value of V_T, corresponding to $V_S = 0.58\,V$, efficient generation of indirect excitons on the slide gate which drift into the trap begins. This can be deduced from the next higher PL branch in Fig. 5.5(a) which results from the PL on the slide gate that enters the objective. Once the QCSE enables, at

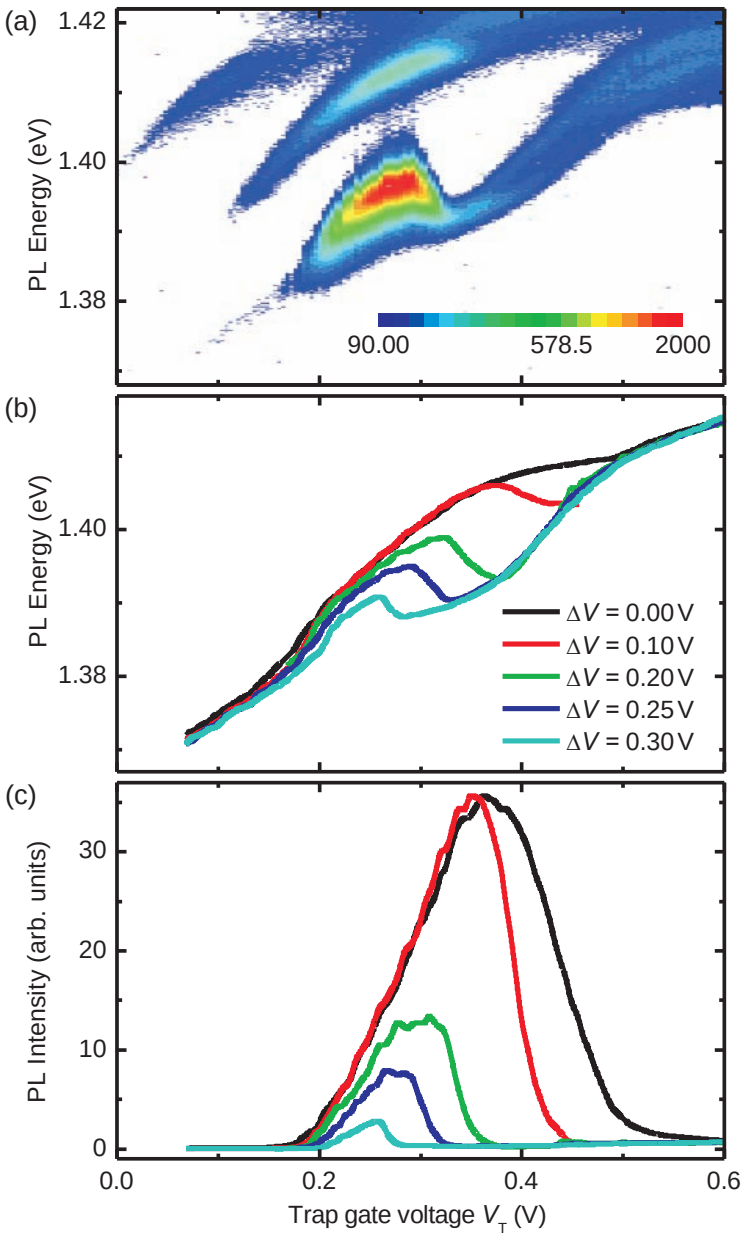

Figure 5.5.: (a) Trap PL dependence with all gate voltages varied simultaneously at constant offset $\Delta V = V_S - V_T = 0.25\,V$ and $V_G - V_T = 0.45\,V$. The energy resolved PL intensity is logarithmically plotted as function of the trap gate voltage. The energetically lowest PL branch is the PL from the trap. Above weak PL signals from the slide and guard gate area are discernible. In (b) is plotted the PL peak energy of the trap for different voltage offsets $\Delta V = V_S - V_T$. The voltage difference between guard and slide gate is always $V_G - V_S = 0.2\,V$. In (c) is shown the corresponding PL intensity collected in the trap. The incident laser power is $20\,\mu W$.

$V_S < 0.58\,V$, spatial separation of photo-generated electron-hole pairs in the CDQW on the slide, the PL energy on the slide decreases and simultaneously the slide PL intensity increases. This is in perfect agreement with the experiments on sample B with a homogenous gate, displayed in Figs. 5.1(c) and 5.1(d). As the offset voltage ΔV is varied the corresponding onset of the filling of the trap is seen in the PL energy versus V_T traces in Fig. 5.5(b). The accompanying increase in the exciton density is reflected by the increase in PL intensity with ΔV shown in Fig. 5.5(c).

With increasing offset ΔV, the region where the trap gets effectively filled with excitons shifts to lower trap gate voltages as a consequence of the voltage dependence generation of IX on the slide gate. The uppermost curve reflects the maximal filling with the laser power used here ($20\,\mu W$). In contrast the lowest trace in Fig. 5.5(c) provides the case of a low exciton density in the trap. Once a blueshift is noticeable in Fig. 5.5(b) we observe an increased PL intensity in Fig. 5.5(c).

5.5. Hysteretic switching of the trapped exciton density

At a sufficiently high generation rate of indirect excitons, we surprisingly observe a hysteretic behavior of the exciton population in the trap. As in the experiment discussed above, the trap gate is biased at a voltage below the one of the slide gate and indirect excitons are generated in the focus spot on the slide gate while PL is detected from the center of the trap gate. At $V_T = 0.35\,V$, $V_S = 0.55\,V$, and an illumination power of $20\,\mu W$ at a laser energy of $1.494\,eV$, the detected PL exhibits a sudden change with decreasing V_G as illustrated in Fig. 5.6(a), where the PL energy is displayed with its intensity logarithmically color coded. The slide gate voltage is chosen to be slightly below the kink voltage V^{kink} in the QCSE [see Fig. 5.1(c)] at which efficient generation of indirect excitons sets in. Using the same data as in Fig. 5.6(a) we plot the PL intensity and energy in Figs. 5.6(b) and 5.6(c), respectively, for both increasing V_G (red trace) and decreasing V_G (black trace). Accordingly, as displayed in Figs. 5.6(b) and 5.6(c), a relatively high intensity and energy of IX is recorded from the center of the trap at voltages $V_G \gg V_S, V_T$ where efficient confinement of IX is realized. However, once V_G is decreased below a threshold V_G^s we observe an abrupt decrease of both the IX energy and intensity in the trap reflecting a sudden loss of IX in the trap. Utilizing spatially resolved PL microscopy as in Fig. 5.2, we verify that this loss occurs whenever the confinement of IX on the slide is lost with decreasing V_G. We note that no such switching behavior is observed when V_G is increased from a value below V_G^s. At $V_G > V_G^s$ and sufficiently high generation rate on the slide a large flow of IX from the slide to the trap causes a strong population of the trap as reflected by a blueshift and a high PL intensity from IX as illustrated in the inset on the right-hand side of Fig. 5.7. At threshold

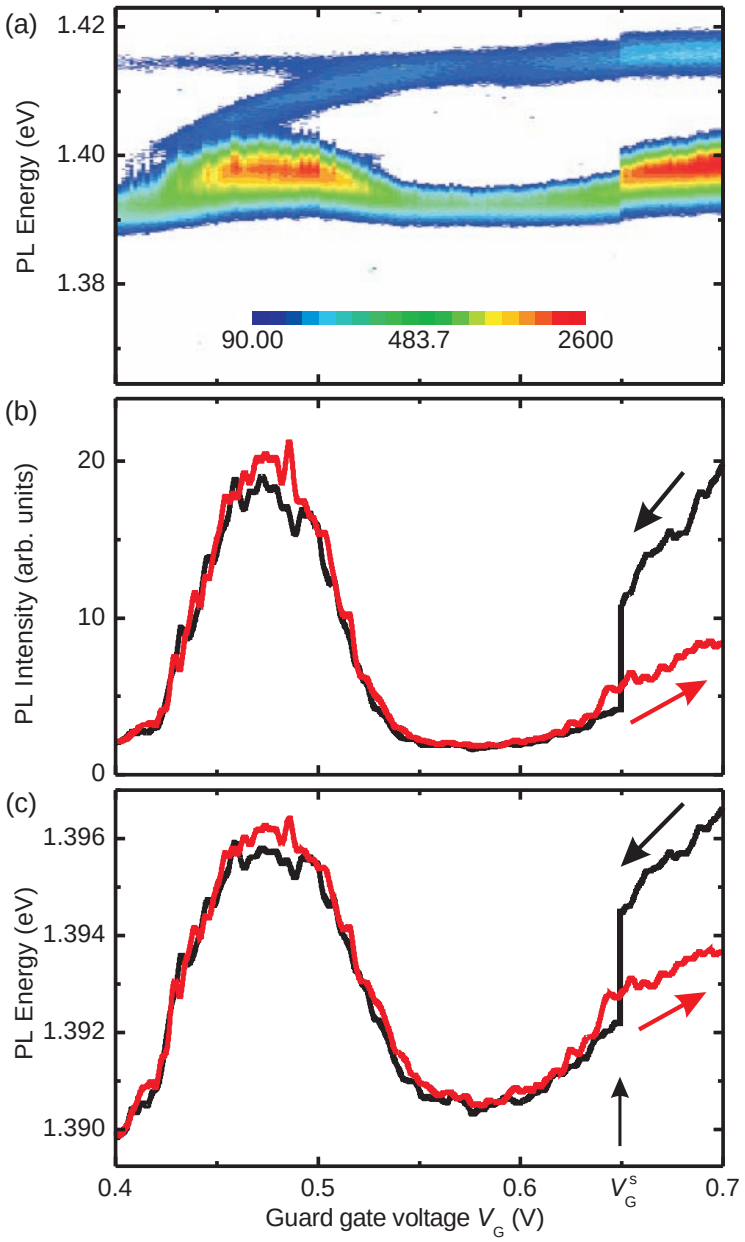

Figure 5.6.: The exciton potential below the guard gate is varied. For the case of high excitation power ($20\,\mu W$) and with the slide gate voltage slightly smaller than the kink voltage of the QCSE we observe a step-like change of the trapped exciton density. In (a) the PL intensity is plotted logarithmically as a function of the PL energy and the decreasing guard gate voltage. In (b) and (c) are shown the corresponding PL intensity energy of the trapped indirect excitons for both sweep directions of V_G. The trap gate voltage is $V_T = 0.35\,V$ and the slide gate voltage $V_S = 0.55\,V$.

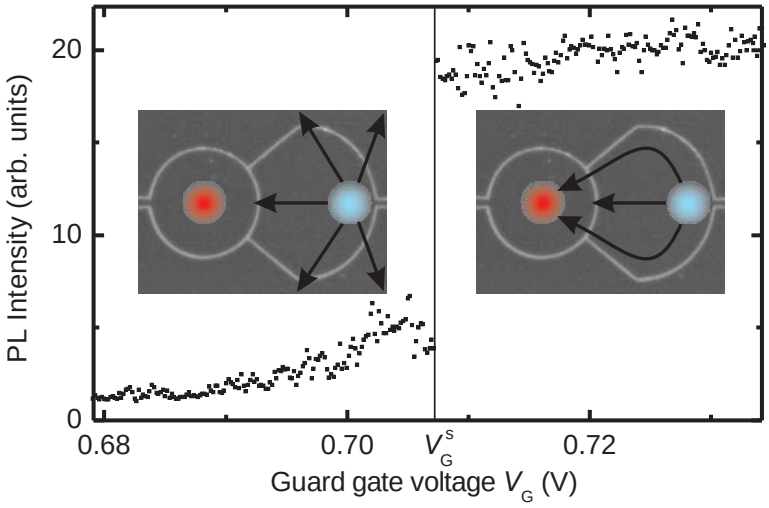

Figure 5.7.: PL intensity at energy 1.40 eV (λ=886.0 nm) as a function of the guard gate voltage. The guard gate voltage is changed in increments of ΔV_G =40 μV between each data point. The laser power of 20 μW is focused on the slide gate and $V_S = 0.575$ V and $V_T = 0.35$ V. The two insets show the IX flow in the potential landscape after and before the switching.

V_G^s confinement of IX on the slide is lost such that the flow of IX from the slide to the trap is suddenly reduced, resulting in a downward jump in the PL intensity and blueshift as illustrated in Fig. 5.6 and on the left-hand side in Fig. 5.7. By reversing the direction of the V_G sweep, the missing excitonic confinement on the slide prevents a strong buildup of IX population in the trap, as shown in the red trace in Figs. 5.6(b) and 5.6(c) for $V_G > V_G^s$.

In the left part of Fig. 5.6 we also observe a regime of decreasing V_G with $V_T < V_G < V_S$ in which the population in the trap builds up again before vanishing once $V_G < V_T$. This behavior is nonhysteretic and indicates that IX generated on the slide and transferred under the guard gate are partly collected in the trap whenever V_G approaches V_T. This implies that IX from under the guard gate become sufficiently long lived and mobile to reach the fringe fields of the trap ($V_G < V^{kink}$). This happens as the QCSE redshifts the PL under the guard gate as seen in the intensity and energy trace in the left part of Figs. 5.6(b) and 5.6(c). With further decreasing V_G the corresponding excitonic potential drops below the one of the trap and thus the trap gets depleted of IX.

The switching instability at V_G^s is further illustrated in Fig. 5.7, where the PL intensity at an emission energy of 1.40 eV ($\lambda \equiv$886 nm) is plotted with step wise reducing V_G in increments of $\Delta V_G = 40\,\mu$V. A single step in V_G reduces the PL intensity at the trap center by about a factor of three as excitons are transferred to the region under the guard gate instead of the trap (see insets in Fig. 5.7). Similar gate-controlled

excitonic switching behavior and flux control has been reported previously [High et al. 2007; High et al. 2008; Kuznetsova et al. 2010] and refereed to as an "exciton optoelectronic transistor", an example of an "excitonic integrated circuit" where the exciton flow is controlled by a gate between "source" and "drain". In our device the flow of IX from source (slide) to drain (trap) is controlled by the bias V_G of the guard gate as illustrated in Fig. 5.7.

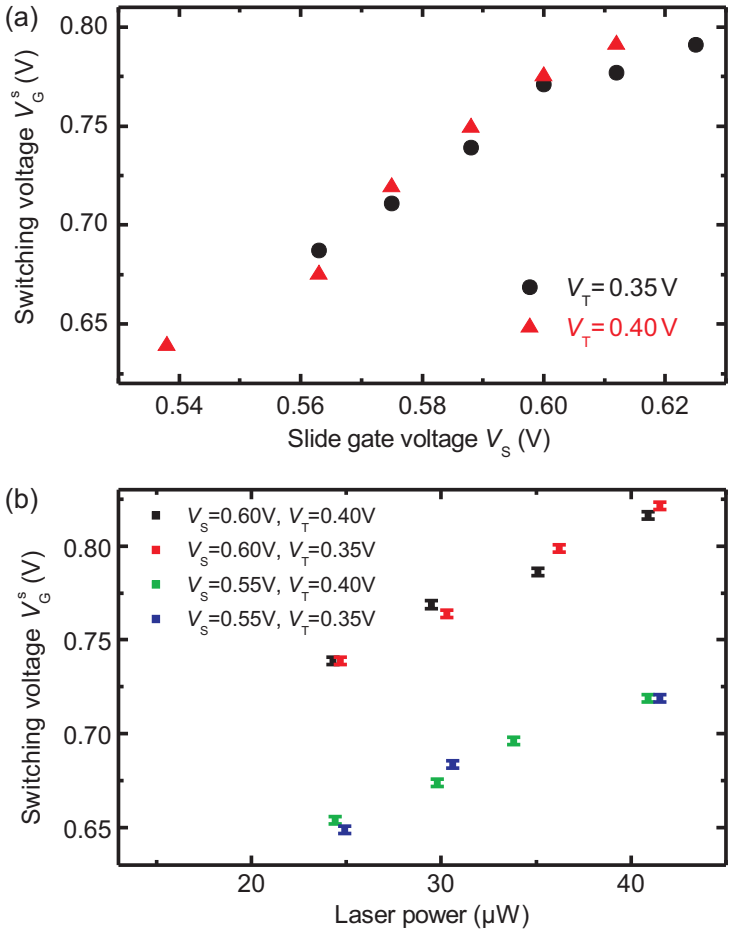

Figure 5.8.: (a) Dependence of the switching voltage V_G^s on the slide gate voltage V_S and (b) the incident laser power for slide gate voltages of $V_S = 0.55\,V$ and $V_S = 0.6\,V$. Variation of V_T from 0.35 V to 0.4 V shows no significant influence in (a) and (b).

Figure 5.8 summarizes the dependence of the switching voltage V_G^s on the bias of the slide gate V_S and the laser power incident onto the spot of electron-hole pair generation on the slide for two values of V_T. Figure 5.8(a) displays V_G^s versus V_S at an incident laser power of 20 μW and shows that V_G^s increases nearly linearly with V_S until it saturates close to the flat band voltage V_{FB}. No significant dependence

on V_T is seen. The population switching is only observed at slide gate voltages V_S with $0.53\,V \lesssim V_S \lesssim 0.63\,V$, i.e., in the regime around the voltage kink in the QCSE [see Fig. 5.1(c)] at which a strong increase of the exciton population occurs under the slide gate. In contrast the population switching appears only above $V_G^s \gtrsim 0.64\,V$, i.e., in the voltage regime where no strong IX population occurs under the guard gate. Increasing the incident laser power [Fig. 5.8(b)] one finds a nearly linear increase of the switching voltage V_G^s with its value depending on V_S but not on V_T. Such a linear increase can be interpreted as reflecting a linear increase in IX density and a corresponding blueshift of the IX energy. Accordingly, the switching voltage V_G^s is shifted upwards.

In the above discussion we have omitted the potential effect of the geometric opening of about 100 nm between the gates needed for isolation. There, the Fermi level pinning of a free GaAs surface at mid-energy gap introduces an additional excitonic barrier, preventing somewhat the immediate flow of excitons between gates biased at the same voltage. We expect some minor effect of this opening on the switching behavior but have omitted it from the above discussion as it is rather difficult to quantify. The abruptness of the switching might be enhanced by effects of illumination reaching the opening. Additionally, we can not exclude some influence of "free" electrons confined under the guard gate for $V_G > V^{kink}$ on the switching behavior.

5.6. Tuning the exciton density in the trap

We now explore the tunability of the exciton density in the trap with illumination intensity while operating at fixed gate voltage settings of $V_T = 0.38\,V$, $V_S = 0.43\,V$, $V_G = 0.8\,V$, close to where the optimum filling of the trap can be achieved. We vary the incident laser power focused on the slide as in Fig. 5.2(b) quasistatically by tuning the power transmitted into the microscope with an acousto-optical modulator. It thus is possible to change the excitation power by three orders of magnitude. The corresponding change in PL energy and intensity of the IX as collected from the trap center is displayed in Fig. 5.9(a). The PL energy initially rises steeply with increasing laser power and then approaches a saturation value. The PL intensity integrated over the IX line shape behaves distinctly differently as it starts with a slow rise and then, at an incident power of and above $\sim 5\,\mu W$, rises linearly with laser power. This difference in behavior becomes amplified as we plot in Fig. 5.9(b) the PL intensity versus the PL blueshift employing the same data as in Fig. 5.9(a), both on a linear scale [black left-hand side of Fig. 5.9(b)] and on a logarithmic scale [red right-hand side of Fig. 5.9(b)]. We assume the blueshift of the PL energy to be proportional to the density of IX as in Equation (5.1) to obtain the density values given at the top of Fig. 5.9(b). This linear relation is likely to underestimate the total IX density by about $2\times10^{10}\frac{1}{cm^2}$ as discussed in Section 5.2. This, however, cannot explain the

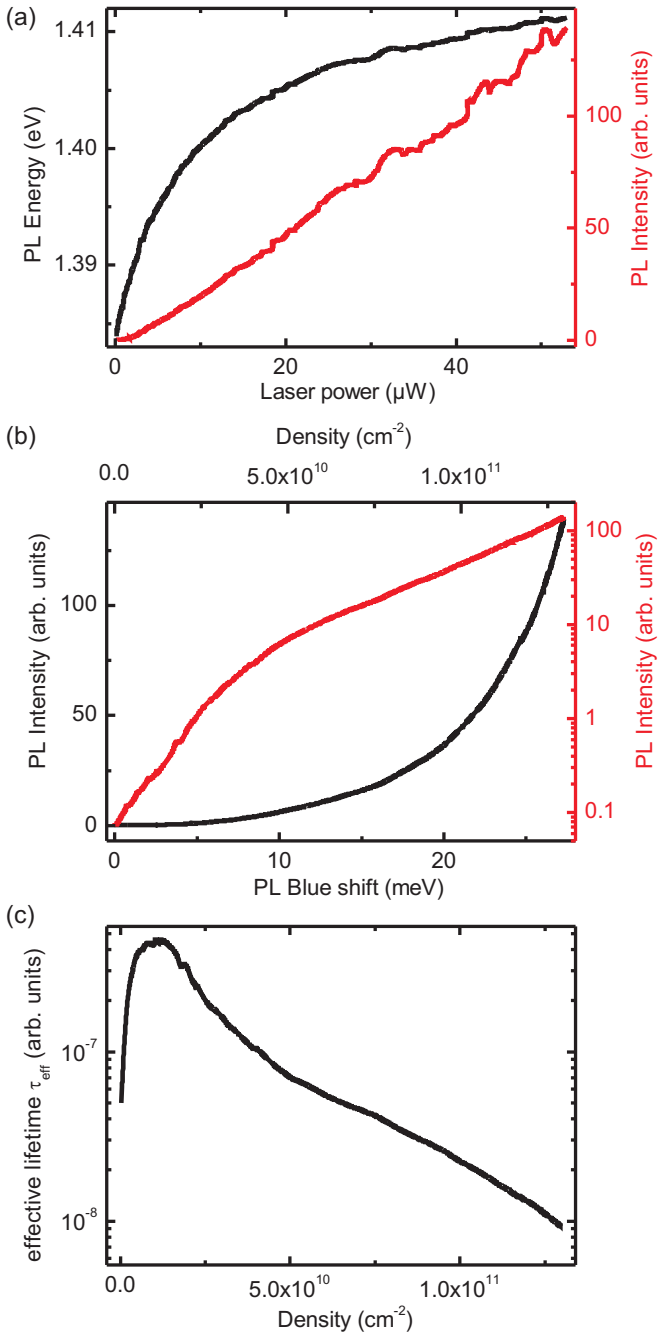

Figure 5.9.: The indirect exciton density in the trap is changed by laser power. In (a) are plotted the PL energy and blueshift (black, left-hand axis) and the intensity (red, right-hand axis) of the trapped excitons as a function of the laser power on the slide gate. The same data are shown in (b) with the PL intensity plotted as a function of the PL blueshift. The linearly scaled PL intensity is shown in black and refers to the scale on the left-hand side and the logarithmically scaled PL intensity in red refers to the scale on the right-hand side. In (c) is plotted the effective exciton lifetime extracted from the data shown in (a) and (b) as a function of the exciton density.

strong nonlinear relation between PL intensity and PL blueshift seen in Fig. 5.9(b). The logarithmically plotted intensity suggests an exponential rise of the PL intensity with density, at least at low excitation powers. A possible explanation could be the action of the random disorder potential, which tends to spatially separate electron and hole wavefunction in the CDQW plane and thus suppresses luminescence at low densities. Possibly at these higher densities collective behavior, such as the screening of a random potential in a trap and exciton-exciton interaction, starts to be of some importance. In particular, the exciton binding energy is expected to decrease at high exciton densities because of screening and scattering in an exciton gas. This can increase the exciton radius and also weaken the exciton oscillator strength. This may contribute to the behavior of PL intensity at high pumping intensities [Fig. 5.9]. In Fig. 5.9(a), the PL energy depends sublinearly on laser power, whereas the PL intensity is close to a linear function, except at small powers. Assuming that the PL energy reflects the IX density, then, one concludes that the IX density in a trap tends to become saturated at high laser powers (or correspondingly high IX densities).

The observations in Figs. 5.9(a) and 5.9(b) can also be interpreted in terms of an effective exciton lifetime. Assuming a simple rate equation for the total exciton population N in a trap, $dN/dt = P - N/\tau_{\text{eff}} = 0$, we obtain $\tau_{\text{eff}} = N/P$, where P is the rate of exciton feeding of the trap. Then, we assume that all excitons radiate and therefore $I_{\text{PL}} \sim P$, where I_{PL} is the PL intensity. In a simplified approach, N is proportional to the energy blueshift (ΔE). In the next step, this naive model gives us $\tau_{\text{eff}} = N/P \sim \Delta E/I_{\text{PL}}$. Since I_{PL} grows nearly linearly with laser power and hence faster than the PL energy shift ΔE [Fig. 5.9(a)], the ratio $\Delta E/I_{\text{PL}}$ and hence τ_{eff} decreases with increasing laser power and equivalently increasing N. Such behavior is reflected in Fig. 5.9(c) at not too low exciton densities in the trap where τ_{eff} versus the exciton density is plotted using the same data as in Figs. 5.9(a) and 5.9(b). This observations can be explained as follows: With increasing exciton density the exciton energy is blueshifted (ΔE) because of the screening of the externally applied electric field. The consequence is a strongly increasing overlap of the tails of the electron and hole wavefunctions forming the IX (at nearly constant dipole moment), thus resulting in a shorter lifetime. In simulations of the electron and hole wavefunction we can verify this behavior (see Section 2.4). Additionally, in experiments lifetimes vary between nanoseconds [Feldmann et al. 1987] for DX (maximum overlap of the wavefunctions) and up to microseconds [Vörös et al. 2009b] for IX. The lifetime decrease obtained in Fig. 5.9(c) at lowest densities $\leq 2 \times 10^{10} \frac{1}{\text{cm}^2}$ is likely to be an artifact, reflecting that $N \sim \Delta E$ is no longer valid as discussed above. An additional influence might result from the random disorder potential expected to have a larger amplitude in InGaAs alloy than in pure GaAs.

Finally we want to point out that the tunability of the IX density of up to $1.3 \times 10^{11} \frac{1}{\text{cm}^2}$ covers the regime of interest where the interexciton distance is still somewhat larger than the excitonic Bohr radius. In this regime, the thermal wavelength of excitons

can be expected to become comparable to their distance at temperatures of order 1 K and below. This motivates us strongly to carry out future experiments to lower temperatures.

5.7. Conclusion

In our present studies we have realized a trapping scheme for spatially indirect excitons in coupled quantum wells that is well suitable for the exploration of excitonic many-body and condensation phenomena. We generate spatially indirect excitons in the focal spot of a relatively low power laser and we use spatial control of the quantum confined Stark effect via suitable patterned and biased gates to transfer IX from the focal spot on the slide gate to an electrostatically tunable trap. The trap provides an attractive excitonic potential but prevents the accumulation of net charges. Using a guard gate surrounding both trap and slide allows us to control the effective excitonic trap depth and to realize efficient transfer of mobile IX from the illumination spot to the trap with well controllable excess energy. As the transfer time of IX to the trap of order 1 ns is significantly larger than the excitonic relaxation time via acoustic phonons we can expect the excitons in the trap to be in thermal equilibrium with the lattice. The achieved tunability of the IX density in the trap covers the regime in which we expect quasibosonic interaction of indirect excitons. Additional cooling of the experiment by about 1 order of magnitude in temperature, which now is within experimental reach, is likely to transform the indirect excitonic ensemble into a condensate. Nevertheless, an additional challenge remains in identifying suitable techniques such as spatial narrowing of the light emission [Balili et al. 2007; Keeling et al. 2004], spectral narrowing of the emission, interference phenomena [Kasprzak et al. 2006], superfluidity [Petrov et al. 2000; Balatsky et al. 2004], and vertices [Lagoudakis et al. 2008; Keeling et al. 2004] to detect the transition to a BEC-like condensate.

6. Many-body correlations of electrostatically trapped dipolar excitons

We study the photoluminescence (PL) of a two-dimensional liquid of oriented dipolar excitons in $In_xGa_{1-x}As$ coupled double quantum wells confined to a microtrap. Generating excitons outside the trap and transferring them at lattice temperatures down to $T = 240\,\mathrm{mK}$ into the trap we create cold quasi-equilibrium bosonic ensembles of some 1000 excitons with thermal de Broglie wavelengths exceeding the excitonic separation. With decreasing temperature and increasing density $n \lesssim 5 \times 10^{10} \frac{1}{\mathrm{cm}^2}$ we find an increasingly asymmetric PL lineshape with a sharpening blue edge and a broad red tail which we interpret to reflect correlated behavior mediated by dipolar interactions. From the PL intensity $I(E)$ below the PL maximum at E_0 we extract at $T < 5\,\mathrm{K}$ a distinct power law $I(E) \sim (E_0 - E)^{-|\alpha|}$ with -$|\alpha|$ ≈ -0.8 in the range $E_0 - E$ of 1.5-4 meV, comparable to the dipolar interaction energy.

6.1. Introduction

Weakly interacting bosons confined in an external potential and cooled to very low temperatures such that the thermal de Broglie wavelength becomes comparable to the inter-particle distance can form a Bose-Einstein condensate (BEC). In this new state of matter, a large fraction of the bosons condense into the energetically lowest quantum state of the external potential, and form a correlated state with a macroscopic wavefunction. BEC has been observed in different systems such as ultra cold diluted atomic gases [Davis et al. 1995; Anderson et al. 1995] or superfluids [Leggett 1999]. More recently, condensation of non-equilibrium quasi-particles in solids, namely cavity exciton polaritons [Kasprzak et al. 2006; Balili et al. 2007; Deng et al. 2010] and magnons [Demokritov et al. 2006], have been reported as other examples of BEC. In an effort to realize BEC of excitons in quasi-equilibrium, predicted already in the 1960s [Blatt et al. 1962; Keldysh et al. 1968], coupled double quantum wells containing two-dimensional systems of long-living and spatially indirect excitons (IX) have been intensively explored for more than a decade [see, e. g. [Butov et al. 1995; Butov et al. 2002; Larionov et al. 2002; Rapaport et al. 2005;

Vörös et al. 2005; Vörös et al. 2006; Yang et al. 2006; Stern et al. 2008a; Vögele et al. 2009a; High et al. 2009a; Alloing et al. 2011; Schinner et al. 2011a]], but fully convincing signatures of a BEC ground state are still missing. Such IX consist of an electron and a hole, spatially separated in the adjacent wells of coupled double quantum well (CDQW) heterostructures and bound by their Coulomb attraction. With their oriented dipolar nature they form a complex and rather strongly interacting bosonic systems with internal structure and not yet fully understood ground state properties. Only recently the influence of dipolar interactions on the ground state properties of such excitonic ensembles has been more intensely theoretically investigated [Laikhtman et al. 2009].

To achieve a quantum phase transition, an efficient trapping of suitable IX densities thermalized to cryogenic temperatures is needed [Petrov et al. 2000; Vörös et al. 2006]. Going beyond previous experiments, we made special efforts to avoid a thermal imbalance between the temperature of the trapped IX and the lattice. In choosing the InGaAs material systems and resonantly exciting direct excitons in the CDQW at an energy below the band gap of the GaAs substrate we assure that most absorption of laser light occurs only in CDQW under the tight focus of the exciting laser. In addition, our special micron scale trap design sketched in Fig. 6.1(a) serves to generate IX on the slide gate several micrometer away from the trap and collect only precooled and neutral bosonic IX under the trap gate. The electrostatic trap uses the in-plane variation of the quantum confined Stark effect (QCSE) to spatially separate the generation of IX from the IX recombination in the trap. This allows to cool the device in a ^{3}He refrigerator down to lattice temperatures of 240 mK and to study the photoluminescence (PL) of typically several 1000 trapped IX with high spatial, energetic, and temporal resolution. In the corresponding IX density regime and with decreasing temperature at which the thermal de Broglie wavelength becomes larger than the excitonic spacing, we observe the integrated intensity of the IX line to increase, while the linewidth narrows and a characteristic lineshape with a sharp blue edge develops. Since this happens at temperatures and IX densities, at which the kinetic energy of the dipolar excitons falls well below their repulsive interdipolar energies of typically 2 meV, we interpret the characteristic change in the PL lineshape and intensity as a signature of a correlated liquid of bosonic IX as theoretically discussed in Ref. [Laikhtman et al. 2009]. Increasing the IX density at lowest temperature by increasing the power of the incident laser we also observe an initial decrease of the PL linewidth combined with an increase of the PL intensity and lineshape asymmetry. Analyzing the PL lineshape $I(E)$ in the energy range $E_0 - E$ <1.5-4 meV below the PL maximum at E_0 we find a characteristic temperature-independent power law $I(E) \sim (E_0 - E)^{-|\alpha|}$, discernable at temperatures $T < 5$ K and moderate densities and indicating an edge-like singularity at E_0.

In our device two 7 nm thick $In_{0.11}Ga_{0.89}As$ quantum wells (QW), separated by a 10 nm thick GaAs barrier, are embedded between a n-doped GaAs back contact and

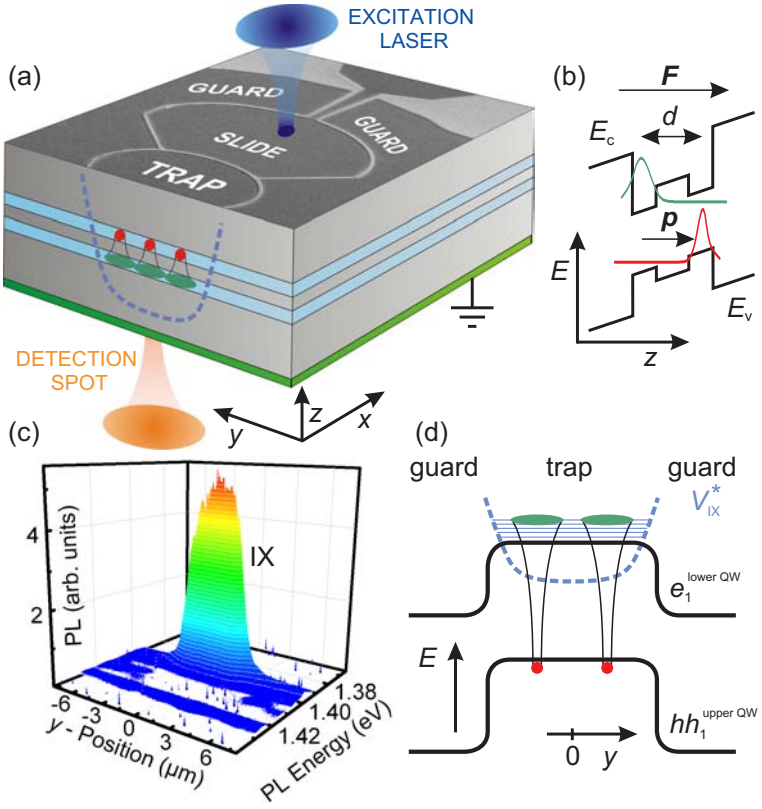

Figure 6.1.: (a) Sketch of the trapping device and detection scheme, incorporating the projection of a scanning electron micrograph of the trap (T) (with diameter of 6 μm), slide (S), and two guard gates (G). Voltages V_T, V_S and V_G are applied with respect to the back contact (green). (b) Schematic CDQW band diagram. E_c and E_v denote conduction and valence band. Electron and hole wavefunction of ground states $e_1^{lowerQW}$ and $hh_1^{upperQW}$ are indicated in green and red, respectively. (c) Pseudo-3D picture of excitonic PL from the trap with spatial and energetic resolution [$V_G = 0.70$ V, $V_T = 0.35$ V, and $V_S = 0.45$ V, $T_{Lattice} = 4$ K, $P_{Laser} = 8.0\,\mu$W, $E_{Laser} = 1.494$ eV]. (d) Corresponding ground state energies of electrons in the lower QW ($e_1^{lowerQW}$) and heavy holes in the upper QW ($hh_1^{upperQW}$) versus y-position across the trap. The IX trapping potential V^*_{IX} is shown containing a hybridized dipolar liquid.

6 nm thick semi-transparent titanium gate electrodes defined by e-beam lithography [Fig. 6.1(a)] [Schinner et al. 2011a]. Voltages applied to the gates define an electric field **F** perpendicular to the QW plane, and cause a red shift of the IX energy of $\Delta E_{IX} = -\mathbf{pF}$, with $\mid \mathbf{p} \mid = ed$ and d the electron-hole distance [Fig. 6.1(b)]. In-plane variation of **F** thus guides IX from the generation spot, where IX are generated via resonantly pumped direct intra well excitons (see Section 6.4), into

the tunable trap. Employing a confocal microscope with two objectives we can separate exciton generation and PL detection, measured in transmission, at different locations (see Chapter 4). An image of the PL intensity in Fig. 6.1(c) demonstrates the trapping efficiency. As sketched in Fig. 6.1(d), the trapping potential V_{IX}^{*} is attractive for neutral dipolar IX but it repels unbound electrons. The low mobility of holes at low temperatures combined with them being trapped by the in-plane disorder potential let us assume that holes are essentially localized. In contrast, the wavefunctions of lighter electrons, confined in the lower QW and bound to holes localized in the upper QW as IX, might overlap and hybridize as their effective Bohr radius $r_{\mathrm{e}} \approx 20\,\mathrm{nm}$ is comparable to half the excitonic separation d_{IX} ($d_{\mathrm{IX}}/2 \approx 28\,\mathrm{nm}$ at $n_{\mathrm{IX}} = n_{\mathrm{e}} = 4 \times 10^{10} \frac{1}{\mathrm{cm}^2}$ see Section 6.7) and the QW separation $d \approx 17\,\mathrm{nm}$, as indicated in Fig. 6.1(d). Caused by the repulsive dipolar interaction of the bound IX in the hybridized system one may expect correlated many-body behavior, similar to a Fermi edge singularity [Skolnick et al. 1987].

6.2. Temperature dependence of the correlated excitonic photoluminescence

The trap collects a cold IX ensemble of varying density and a typical lifetime of about 200 ns caused by the reduced overlap of the electron and hole wavefunctions forming the IX. To explore the exciton thermodynamics, we analyze the temperature dependence of the IX PL collected from the center of the trap. With decreasing temperature an increasingly asymmetric PL lineshape is observed as exemplarily shown in Fig. 6.2(a). As displayed in Fig. 6.2(b), we also observe a strong increase of the integrated PL intensity accompanied by a narrowing of the PL linewidth. From these experimental observations, we deduce that many-body correlations start to become important with decreasing temperature, finally resulting in an edge-like singularity. To achieve a deeper insight into the underlying exciton dynamics, we analyze the high (blue) and low (red) energy sides of the PL line separately. From the blue side of the PL lineshape we extract an apparent exciton gas temperature T_{app} inside the trap (see Section 6.10). To this end, we assume only temperature-induced broadening and neglect all other broadening, e.g., by disorder [Fig. 6.2(c)]. Using local resonant generation of direct excitons in the CDQW we minimize radiative heating (see Section 6.4). Since the thermal equilibration via phonons happens on time scales below 1 ns, much shorter than the IX lifetime, we estimate the real IX temperature in the trap to be much closer to T_{Lattice} than to T_{app}. The saturation of $T_{\mathrm{app}} \simeq 3\,\mathrm{K}$ at low temperatures, corresponding to energy of $\sim 0.3\,\mathrm{meV}$, is likely to be caused by inhomogeneous line broadening and temporal fluctuations.

Many-body processes can be observed in characteristic PL lineshapes [Skolnick et al. 1987; Citrin et al. 1977]. From recently published theoretical [Türeci et al. 2011]

and experimental works [Latta et al. 2011] on lineshapes in quantum structures, one can conclude that different many-body phenomena with distinct energy scales are

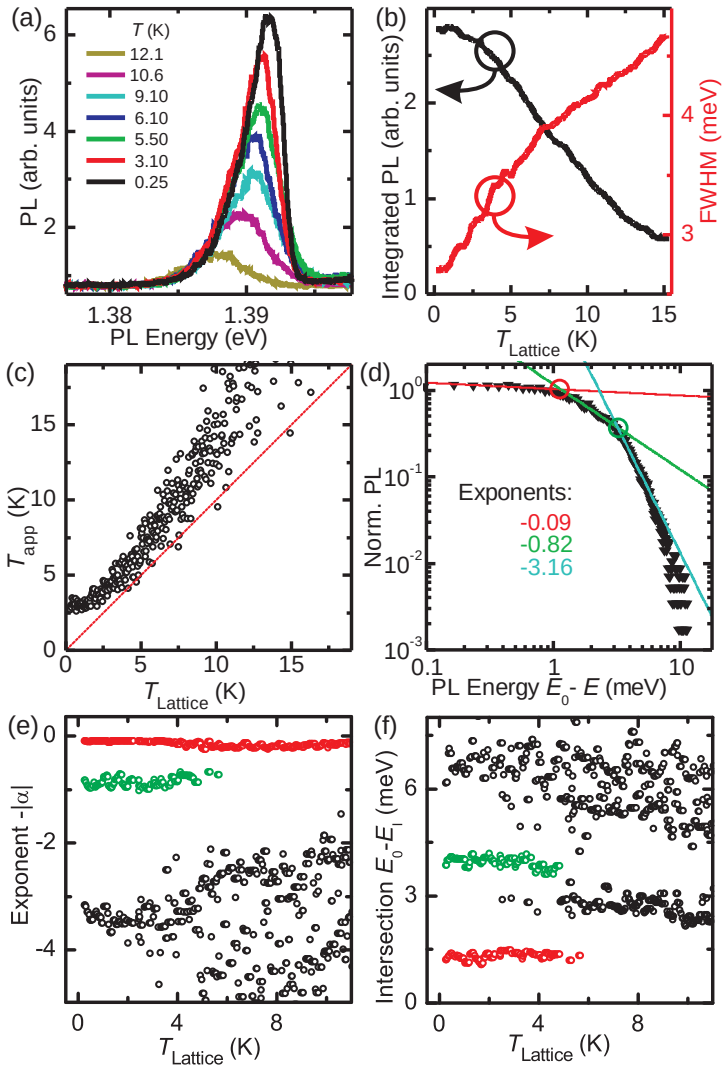

Figure 6.2.: (a) Energy-resolved PL spectra, for different lattice temperatures, detected from the center of the trap [$V_G = 0.70\,V$, $V_T = 0.32\,V$, and $V_S = 0.35\,V$, $P_{Laser} = 2.7\,\mu W$, $E_{Laser} = 1.4289\,eV$]. (b) Corresponding integrated PL intensity (left axis) and full linewidth at half maximum (right axis). (c) Exciton gas temperature T_{app} extracted from the blue tail of the PL line [$P_{Laser} = 1.4\,\mu W$]. (d) Red tail of PL normalized logarithmically plotted as a function of $E_0 - E$, with E_0 the energy of the PL maximum [$T_{Lattice} = 250\,mK$]. Color-coded (e) corresponding exponents and (f) intersection energies $E_0 - E_I$ at which the power laws in (d) change versus $T_{Lattice}$.

reflected by different power laws in the lineshape of discrete optical transitions at energy E. Such power laws correspond to different temporal dynamics, becoming faster with increasing $E_0 - E$ [Türeci et al. 2011], where E_0 denotes the energy of the PL maximum. In previous PL experiments, the red tail of the spectra was attributed to the random disorder potential [Kash et al. 1991; Duarte et al. 2008] or the interplay of disorder potential and BEC [Larionov et al. 2002]. As in Refs. [Türeci et al. 2011; Latta et al. 2011], we analyze the red tail of the PL lineshape by plotting the PL intensity logarithmically versus the logarithm of the PL energy in a $\log(I)$ vs. $\log(E_0 - E)$ diagram [Fig. 6.2(d)]. In the log-log display it is possible to identify power laws $I(E) \sim (E_0 - E)^{-|\alpha|}$ with different exponents α separated by kinks at which different power laws intersect (see Section 6.8). In Fig. 6.2(d), and (e), we identify three different exponents associated with characteristic energy intervals [Fig. 6.2(f)] related to specific interactions (see Section 6.8). The appearance of a few exponents in an optical correlation function seems to be typical for many-body correlated systems [Türeci et al. 2011]. The most interesting exponent is the second exponent showing values of about -0.8. We relate this to a correlated low temperature many body phase of a two-dimensional dipolar liquid of parallel oriented excitons as theoretically predicted in Ref. [Laikhtman et al. 2009]. This power law rather abruptly disappears at $T_{\mathrm{Lattice}} \gtrsim 5\,\mathrm{K}$ [Fig. 6.2(e)]. As predicted in Ref. [Laikhtman et al. 2009] a correlated dipolar liquid is expected only at sufficiently low temperature and high enough trapped IX densities and should exhibits a rather gradual transition.

6.3. Density dependence of the correlated excitonic photoluminescence

We further investigate the PL spectra as a function of the exciton density, varied by changing the exciting laser power. In Fig. 6.3(a), the PL intensity, normalized to the laser power, is plotted versus energy relative to the blue edge energy E_{E} at which the PL intensity drops to half of the maximum value (original spectra see Fig. 6.5(b)). Around the PL maximum, the intensity rises more steeply than laser power P_{Laser}. Using the blue shift ΔE of the PL maximum with increasing laser power as a measure of the exciton density, we obtain the density dependence of the integrated PL intensity shown in Fig. 6.3(b) (see Section 6.6). We point out that only a part of the nonlinear increasing PL intensity can be explained by a decreasing IX lifetime [Schinner et al. 2011a]. For $P_{\mathrm{Laser}} < 1.2\,\mu\mathrm{W}$, we observe a decreasing linewidth with rising exciton density [Fig. 6.3(c)]. A related observation in quantum wells was recently associated with screening of the disorder potential by repulsive IX-IX interaction [Alloing et al. 2011]. The density dependent decrease of the linewidth is accompanied by finding the exponent $-|\alpha| \approx -0.8$ in the log-log plot of the red tail

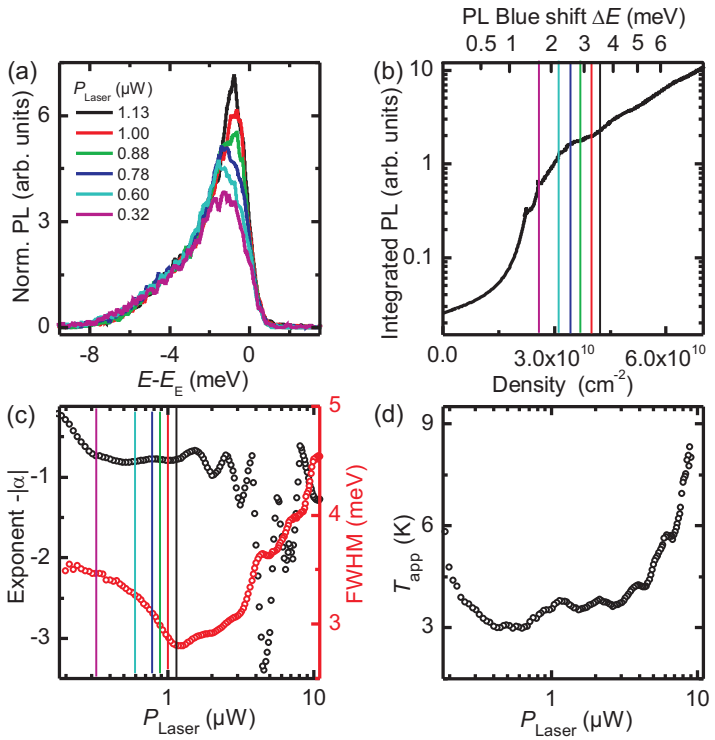

Figure 6.3.: (a) PL spectra, for different laser powers, detected from center of the trap. PL intensity is normalized to P_{Laser} and the spectra are energetically shifted such that the Fermi-edge-like steepest slope in the PL vs. E spectra is at $E_{\mathrm{E}} \approx 0$ (original spectra see Fig. 6.5(b)). (b) Integrated PL intensity plotted as a function of blue shift ΔE and corresponding density. Vertical lines in (b) and (c) are color-coded to reflect the different laser powers in (a). (c) Second exponent α (left axis) and linewidth (right axis) as a function of P_{Laser}. (d) An upper limit is shown for T_{app} [$V_{\mathrm{G}} = 0.70\,\mathrm{V}$, $V_{\mathrm{T}} = 0.32\,\mathrm{V}$, $V_{\mathrm{S}} = 0.35\,\mathrm{V}$, $T_{\mathrm{Lattice}} = 243\,\mathrm{mK}$, $E_{\mathrm{Laser}} = 1.4289\,\mathrm{eV}$].

[Fig. 6.3(c)]. In the same density regime we find at low temperatures the exponent -$|\alpha| \approx$ -0.8 in the temperature-dependent spectra [Fig. 6.2(e)] which supports the our that this power law is associated with a correlated dipolar liquid. With increasing exciton density the dipolar interaction energies of the IX sum up to the observed blue shift ΔE (see Section 6.6). The lineshape asymmetry thus can be interpreted as a broadened sum of individual excitonic transitions (see Chapter 7). In related studies on electrostatic traps fabricated on the same InGaAs heterostructure with an effective trap diameter of down to about 100 nm and thus a trap area of roughly 1000 times smaller than those considered here, we observe discrete individual lines of linewidth below 0.5 meV which dependent on laser power as characteristic for single excitons, biexcitons and triexcitons, respectively (see Section 7.3). Further

increasing the trap population, these merge at low temperatures into an asymmetric lineshape thus lending additional support to the interpretation given here in terms of correlated behavior. At high laser powers, the extracted exponent α starts to oscillate due to an interference substructure overlaying the PL lineshape [Fig. 6.3(c), for details see Section 6.9] and we see an expected homogeneous broadening [High et al. 2009a] of the PL line caused by exciton-exciton scattering with increasing exciton density. From the blue side of the PL lineshape we extract a rising upper limit for the apparent exciton gas temperature T_{app} [Fig. 6.3(d)].

6.4. Resonant exciton excitation

In our trapping configuration the exciton generation occurs on the slide gate typically spatially separated by 9 μm from the center of the trap and the exciton trap is filled only with indirect excitons, pre-cooled to lattice temperature [Schinner et al. 2011a]. To further reduce the radiative heating in the sample and the excitation of free charge carriers, we resonantly pump the intra well direct exciton with a tunable diode laser. The photon energy of the excitation laser is below the GaAs band gap and, apart from some absorption in the semitransparent metal gates, can be only absorbed in the coupled double quantum wells. Accordingly, only the energy of the direct to indirect exciton conversion is deposited in the phonon bath of the sample. In Fig. 6.4 a photoluminescence excitation (PLE) measurement at $T_{\mathrm{Lattice}} = 246\,\mathrm{mK}$ is shown. Here, the integrated PL intensity of the indirect excitons is plotted as a function of the laser excitation energy exciting direct excitons on an unstructured gate 10 μm away from the detection spot. In Fig. 6.4 we observe a strong IX PL when the

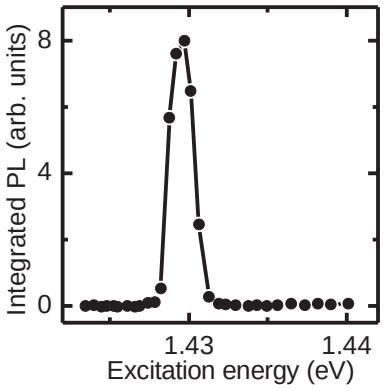

Figure 6.4.: **Photoluminescence excitation measurement.** Integrated PL intensity centered at 1.399 eV of the indirect excitons as a function of the laser excitation energy [$V_{\mathrm{Gate}} = 0.35\,\mathrm{V}$, $P_{\mathrm{Laser}}(E_{\mathrm{Laser}}) = 4.75\,\mu\mathrm{W}$, $T_{\mathrm{Lattice}} = 246\,\mathrm{mK}$].

direct exciton is resonant with the tunable laser energy and so direct excitons are efficiently pumped transforming into the detected indirect excitons.

6.5. Density dependence of the correlated excitonic photoluminescence

To explore the tunability of the exciton density in the trap with illumination intensity, we vary the incident laser power focused on the slide quasi-statically by tuning the power transmitted into the microscope with an acousto-optical modulator. Thus it is possible to change the excitation power by three orders of magnitude. Fig. 6.5(a) is identical to Fig. 6.3(a) and plots PL spectra, for different laser powers, detected from the center of the trap. The PL intensity is normalized to the excitation laser power and the spectra are energetically shifted such that the Fermi-edge-like steepest slopes in the PL vs. E are $E_{\mathrm{E}} \approx 0$. The corresponding original spectra are shown in Fig. 6.5(b). To obtain these spectra we integrate 55 seconds with a detection rate of 12.5 counts per second in the PL maximum at 1.0 μW.

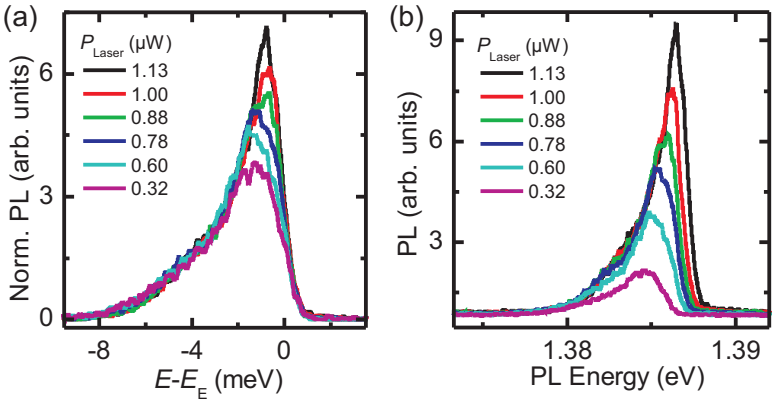

Figure 6.5.: **Laser power dependence of the PL lineshape normalized versus original spectra.** (a) Energy resolved PL spectra for different laser excitation powers (identical to Fig. 6.3(a)). The PL intensity is normalized to the excitation laser power and the spectra are energetically shifted to correct the density caused blue shift. In (b) the corresponding original spectra are shown [$V_{\mathrm{G}} = 0.70\,\mathrm{V}$, $V_{\mathrm{T}} = 0.32\,\mathrm{V}$, and $V_{\mathrm{S}} = 0.35\,\mathrm{V}$, $T_{\mathrm{Lattice}} = 243\,\mathrm{mK}$, $E_{\mathrm{Laser}} = 1.4289\,\mathrm{eV}$].

6.6. Conversion from blueshift to exciton density

The quantum confined Stark effect causes a red shift of the excitonic energy of $\Delta E_{\mathrm{IX}} = -\mathbf{pF}$ where $\mathbf{p}$ is the IX dipole moment and $\mathbf{F}$ the electric field perpendicular to the QW plane. In a trapped IX ensemble all individual dipoles $\mathbf{p} = e\mathbf{d}$ are aligned and perpendicular to the QW plane. The effective electric field, seen by the individual dipole moment of a single IX, is the sum of the externally applied electric field and the depolarizing dipole field of all other IX in the vicinity. With increasing exciton density the effective electric field decreases and causes a blue shift ΔE. For not too small densities n of $n \gtrsim 2.5 \times 10^{10} \frac{1}{\mathrm{cm}^2}$ the simplest approximation is that the blue shift is proportional to the exciton density $\Delta E = \frac{4\pi e^2 d}{\epsilon} n$ (see black line in Fig. 6.6) where ϵ is the dielectric constant. In the low-density limit the IX-IX interaction was theoretically investigated in Refs. [Zimmermann et al. 2007; Schindler et al. 2008; Laikhtman et al. 2009; Ivanov et al. 2010] and results in a density and temperature-dependent correction factor $f(T, n)$ in $\Delta E = \frac{4\pi e^2 d}{\epsilon} n f(T, n)$. From this formula we find a nonlinear relation between blue shift and density as plotted by the red curve in Fig. 6.6. The latter is used to convert blue shift ΔE to density in Fig. 6.3(b).

A third naive $T = 0$ approach to convert the measured blue shift into a trapped IX density is to sum up the dipole fields of the trapped indirect exciton ensemble acting

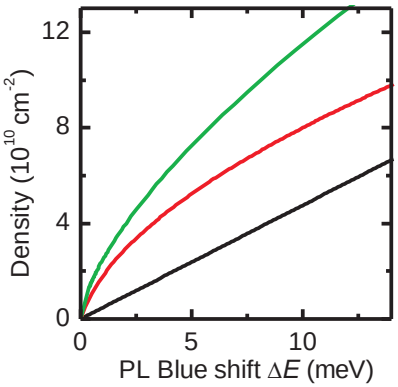

Figure 6.6.: **Conversion from blue shift to exciton density.** The black straight line shows the linear conversion between the blue shift ΔE of the PL maximum energy and the corresponding IX density. In the red curve a density dependent correction factor is included providing a better approximation of the real exciton density. The upper green curve show the conversion between blue shift and trapped IX density for a two-dimensional hexagonal ordered crystal of parallel oriented dipolar excitons.

on a single dipolar exciton. For this method it is assumed that the dipolar exciton liquid is ordered in a two-dimensional hexagonal crystal of dipoles arranged in parallel. A single dipolar exciton sees a blue shift, caused by another dipolar exciton in a distance $d_{\mathrm{IX-IX}}$, of $W = \frac{p^2}{\epsilon d^3_{\mathrm{IX-IX}}}$ where $p = ed$ is the IX dipole moment resulting from the electron-hole separation by a distance d in the two adjacent quantum wells and ϵ is the dielectric constant. The total blue shift ΔE for a single exciton with a next neighbor distance d_{IX} is calculated by summing up all contributions W of every trapped exciton. The next neighbor distance d_{IX} is converted by $n = \frac{3\sqrt{3}}{4d^2_{\mathrm{IX}}}$ in the corresponding trapped indirect exciton density n. The green curve in Fig. 6.6 shows the result.

6.7. Diamagnetic shift of the exciton energy in magnetic fields and relevant length scales

A magnetic field B applied in Faraday configuration perpendicular to the QW plane causes a diamagnetic quadratical shift of the electrostatically trapped IX energy by $\Delta E_{\mathrm{dia}} = \frac{e^2 r_{\mathrm{e}}^2}{8\mu c^2} B^2$ where r_{e} is the effective Bohr radius, μ the reduced mass of the exciton [Bugajski et al. 1986; Stern et al. 2008a]. In Fig. 6.7 the quadratic behavior of the PL maximum energy, detected from the center of the trap, is shown as a function of the magnetic field. Fitting the exciton diamagnetic shift we find a corrected effective Bohr radius of $r_{\mathrm{e}}^* = 20\,\mathrm{nm}$ [Walck et al. 1998]. If the hole is strongly localized, it is necessary to use the electron mass instead of the reduced

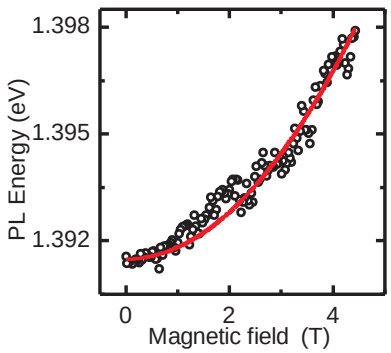

Figure 6.7.: **Magnetic field dependence.** The PL maximum detected in the center of the trap is plotted as a function of the magnetic field applied perpendicular to the QW plane. In addition, a quadratic fit for the diamagnetic shift is shown from which we find an effective Bohr radius $r_{\mathrm{e}} = 20\,\mathrm{nm}$ [$V_{\mathrm{G}} = 0.70\,\mathrm{V}$, $V_{\mathrm{T}} = 0.32\,\mathrm{V}$, and $V_{\mathrm{S}} = 0.35\,\mathrm{V}$, $T_{\mathrm{Lattice}} = 256\,\mathrm{mK}$, $E_{\mathrm{Laser}} = 1.4289\,\mathrm{eV}$, $P_{\mathrm{Laser}} = 3.5\,\mu\mathrm{W}$ circular polarization].

mass μ which results in an effective Bohr radius of $r_e^{**} = 16\,\text{nm}$. The quadratic diamagnetic shift shows that electrons and holes are excitonically bound. In our trapping configuration it is only possible to confine IX, free electrons are repelled. For free charge carriers or an electron-hole plasma different dependence of the PL line is reported, reflecting quantized Landau levels [Stern et al. 2008a; Kowalik-Seidl et al. 2011].

The thermal de Broglie wavelength λ_{dB} of a bosonic particle in two dimensions with a quadratic dispersion relation is given by $\lambda_{\text{dB}} = \frac{\hbar}{\sqrt{2m\pi kT}}$ where m is the total mass of the exciton (sum of electron and hole mass) [Yan 2000]. The interexcitonic distance d_{IX} in a two-dimensional exciton lattice hexagonal arrangement is given by $d_{\text{IX}} = \sqrt{\frac{3\sqrt{3}}{4n}}$. In the correlated many-body state the thermal de Broglie wavelength ($\approx 75\,\text{nm}$ at $2\,\text{K}$) is larger than the interexcitonic distance $d_{\text{IX}} \approx 57\,\text{nm}$ at $n = 4 \times 10^{10} \frac{1}{\text{cm}^2}$ and d_{IX} is similar to twice the effective Bohr radius $r_e \approx 20\,\text{nm}$.

6.8. Analysis of the red tail of the spectra

The analysis of the red tail of the photoluminescence spectra clearly showed the occurrence of different power laws with distinct exponents. The first exponent with a value of about -0.1 can be related to a low-energy excitation of up to 1.5 meV and reflects slow temporal behavior, possibly induced by thermal broadening. The second exponent shows values of about -0.8 describing a medium energy excitation of the IX ensemble in the energy interval between 1.5 and 4 meV. This power law rather abruptly disappears at $T_{\text{Lattice}} \gtrsim 5\,\text{K}$ [Fig. 6.2(e)] and we relate it to a correlated many-body phase of a liquid of parallel oriented dipolar excitons as theoretically predicted in Ref. [Laikhtman et al. 2009]. This correlated phase appears only at low temperatures and high enough trapped IX densities. The third exponent of about -3 is related to high-energy ($E_0 - E > 4\,\text{meV}$) excitations of the IX ensemble on a fast time scale. Most likely, phonon emission on a picosecond time scale and shake-up processes, in which the recombining exciton transfers part of its energy to a collective excitation of its interacting neighboring excitons, are responsible for this behavior.

In order to determine the exponent of the different power laws $I(E) \sim (E_0 - E)^{-|\alpha|}$ in the red tails of the PL lineshape in the log-log plots [Fig. 6.8(a), (b)] we employed the following numerical method. In Fig. 6.8 this method is shown exemplarily for one spectrum. In the first step the first derivative of the logarithmized data is calculated. Simply taking the difference between two neighboring data points would yield a very noisy result. For a fixed energy $E_0 - E$ a linear fit is done over $\pm i$ neighboring data points. The slope obtained by the linear fit over the $2i+1$ data points gives the value of the first derivative for this energy. This is repeated successively for each energy

point. The result is shown in Fig. 6.8(c). The second derivative is calculated in the same way from data points of the first derivative. All data pairs whose values of the second derivative are in a range of ±0.5 are considered as having a constant slope. These data points are between the two horizontal lines in Fig. 6.8(d). If the slopes of two or more data points differ less than 0.1 for the first slope and 0.5 for all other slopes these slopes and their corresponding energies are averaged. The previous values provide the best results but small variations do not change the exponents of the power laws. In contrast to Fig. 6.2(d) in Fig. 6.8(a) the logarithmized data are plotted to illustrate that in our numerical method a linear fit of the logarithmized data is done.

We used a second method as a consistency check by performing a linear fit over $\pm i$ neighboring data points. If none of the $2i + 1$ residues is larger than a predefined

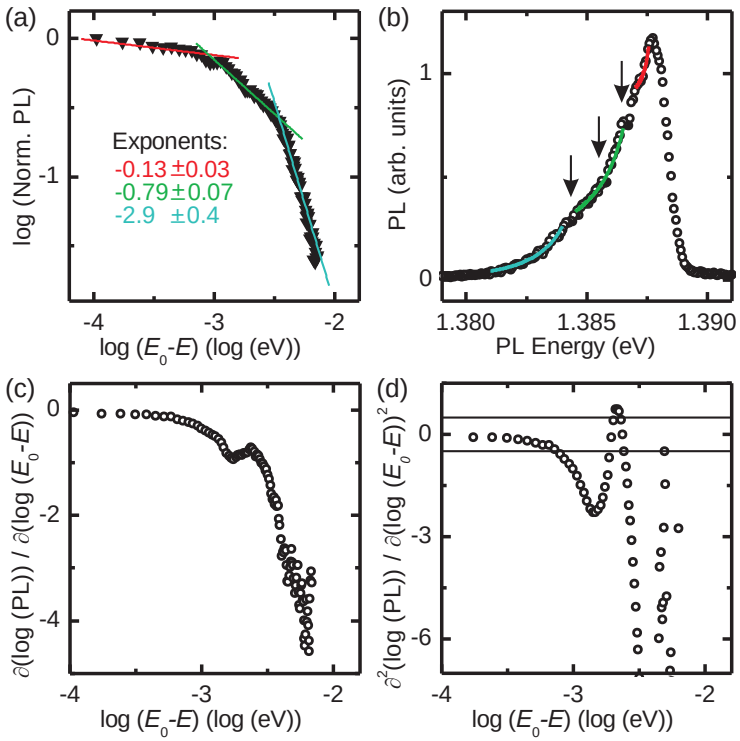

Figure 6.8.: **Analysis of the red tail of the spectra in a log-log diagram.** (a) log-log plot of one typical spectrum. The slopes are determined by the numerical method described in the text [$V_G = 0.70\,V$, $V_T = 0.32\,V$, and $V_S = 0.34\,V$, $P_{Laser} = 1.69\,\mu W$, $T_{Lattice} = 248\,mK$, $i = 5$]. (b) Original spectrum with power laws determined by the slopes. (c) First derivative of the logarithmized data. (d) Second derivative of the logarithmized data. The values between the two horizontal lines represent data points which were used to calculate the slopes.

value, these data points are considered as having a constant slope. This procedure is also repeated successively for each energy point, and data points with similar slopes are averaged in the same way as described above. Both methods yield comparable results. However, the first method turned out to be more general since the signal-to-noise ratios of our spectra differ substantially and the residues depend strongly on the signal-to-noise ratio.

6.9. Interference substructure superimposed on the PL lineshape

Photoluminescence spectra having many photon counts and correspondingly large signal-to-noise ratio show a pronounced substructure in the form of energetically equidistant shoulders. In Fig. 6.8(b) this shoulders are marked with arrows. While the spectra shift with changing IX density the substructure is fixed on an absolute energy scale. We identify the energetic periodicity of the substructure as an interference effect inside the heterostructure, where a cavity is formed between the top and the bottom surface of the sample. A similar interference effect has been reported in [Latta et al. 2011]. We found that the slopes are influenced by the substructure and the slope starts to oscillate. Nevertheless, the data at low densities yield a convincing evidence that the power law with -$|\alpha|$ $\approx$ -0.8 is an intrinsic and characteristic feature and is not caused by such interference effects. All temperature-dependent measurements show that the slope slightly lower than 1 disappears for temperatures $T \gtrsim 5\,\mathrm{K}$. This suggests a breakdown of the correlation effect and cannot be explained with an interference effect. In log-log-plots of spectra with normal signal-to-noise ratios we observe no pinning of the boundary point positions on the interference substructure. We explain this with the absence of the substructure due to the lower signal-to-noise ratio.

6.10. Indirect exciton gas temperature

We use two different methods to determine the apparent exciton gas temperature T_{app} [see also Fig. 6.2(c) and Fig. 6.3(c)] from the blue tail of the PL spectrum. In the first method the exciton gas temperature is extracted from the exponential Boltzmann-like behavior of the blue tail. Therefore the natural logarithm of the PL intensity is calculated and the slope of the linear regime is determined with the same numerical method as described above. One slope obtained with this method is shown in Fig. 6.9(a) together with the logarithmically plotted spectrum. Using logarithmic data for the fit has the advantage that data with low intensity away

from the PL maximum are weighted more strongly compared to an exponential regression of the original data. In this regime the assumption of a Maxwell-Boltzmann distribution is approximately valid. The exciton gas temperature can be calculated directly from this slope. Our second approach is to multiply a Gaussian distribution with a Fermi-Dirac distribution. The Gaussian distribution is introduced to reflect broadening of the PL line by (i) the energy dependent density of states of the interacting IX dipoles in the trap (ii) the random disorder potential in the CDQW and (iii) effects of time-dependent spectral diffusion as the displayed spectra are accumulated over approximately 1 minute. The Fermi-Dirac distribution is used as a cutoff function, reflecting the thermal smearing of the filling of the trap with the dipolar

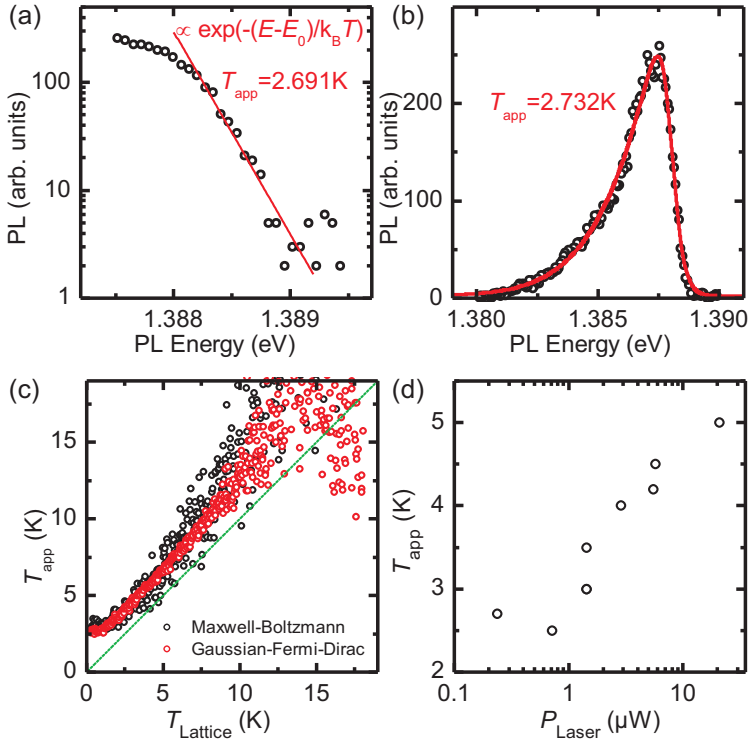

Figure 6.9.: **Extraction of an apparent exciton gas temperature.** (a) Natural logarithm plot of the blue side of one spectrum. The red line is obtained by the numerical method described in the text [$V_G = 0.70\,V$, $V_T = 0.32\,V$, and $V_S = 0.35\,V$, $P_{Laser} = 1.4\,\mu W$, $T_{Lattice} = 285\,mK$, $i = 5$]. (b) PL spectrum from the same data as in (a). The red curve represents a "Gauss-Fermi-Fit", which is described in the text. (c) Fit results of a temperature dependent measurement. Both methods are in good agreement. (d) Saturation temperatures of T_{app} for different excitation powers extracted from different temperature sweeps like those displayed in (c) [$V_G = 0.70\,V$, $V_T = 0.32\,V$, and $V_S = 0.35\,V$].

exciton liquid. In combination the Gaussian distribution describes the red tail of the spectrum while the Fermi-Dirac distribution describes the temperature-broadened steep decrease on the blue tail of the spectrum. In the case of the bosonic dipolar liquid the strong spatial dipolar repulsion replaces the role of the Pauli principle in the Fermi-Dirac distribution. One spectrum together with its fit is shown in Fig. 6.9(b). Although the assumption of a Fermi sea can only be considered approximatively since we have an IX ensemble with hybridized electrons and no free electrons, the results of this method are in good agreement with the exciton gas temperatures obtained by the first method. The temperatures extracted by the Fermi-Dirac distribution scatter less than these using the Maxwell-Boltzmann fit. Both fits show a constant offset to the lattice temperature [green line in Fig. 6.9(c)] which at least in part can result from the broadening contributions discussed above which persist to lower lattice temperatures. Additional temperature independent broadening of the blue tail of the excitonic emission, not included in the modeling, is likely to result from scattering events or shake-up processes and may be an essential contribution to this constant offset of the exciton gas temperature extracted from the fits. Hence T_{app} should be considered as an upper limit of the IX temperature whereas the real IX temperature is likely to be considerably closer to the lattice temperature. For a lattice temperature $T_{\mathrm{Lattice}} \lesssim 1$ to 2 K, we observe a saturation of the T_{app} [Fig. 6.9(c)] corresponding to an upper bound of the apparent exciton gas temperature at $T_{\mathrm{app}} = 3$ K. Fig. 6.9(d) shows the saturation temperatures of several temperature sweeps with different excitation powers. This plot indicates that the saturation temperature decreases exponentially with decreasing excitation power.

6.11. Conclusion

In conclusion, at temperatures and densities at which the thermal de Broglie wavelength (≈ 75 nm at 2 K) is larger than the interexcitonic distance $d_{\mathrm{IX}} \approx 57$ nm at $n = 4 \times 10^{10} \frac{1}{\mathrm{cm}^2}$ we observe a characteristic temperature and density-dependent transition to a specific quantum state of the IX ensemble. In this regime, d_{IX} is comparable to twice the effective excitonic Bohr radius $r_{\mathrm{e}} \approx 20$ nm as well as the QW separation ($d \approx 17$ nm). From the appearance of the strongly increasing integrated PL intensity as well as a PL linewidth decreasing with increasing density, we conclude that this state reflects a correlated many-body state mediated by dipole-dipole interactions. In the analysis of the red tail of the PL lineshape we observe at $T_{\mathrm{Lattice}} \lesssim 5$ K a characteristic power law dependence of the PL intensity reflected in exponent -$|\alpha|$ $\approx$ -0.8, associated with an energy between 1.5 meV and 4 meV. This we interpret as a generic fingerprint of dipolar many-body correlations. A theoretical understanding of this power law cannot be given at present but this very interesting observation in our opinion should motivate further theoretical and experimental studies in the field.

7. Single exciton control in gate-defined quantum traps

With gate-defined electrostatic traps fabricated on a double quantum well we are able to realize an optically active and voltage-tunable quantum dot confining individual, long-living, spatially indirect excitons. We study the transition from multi excitons down to a single indirect exciton. In the few exciton regime, we observe discrete emission lines reflecting the interplay of dipolar interexcitonic repulsion and spatial quantization. The quantum dot states are tunable by gate voltage and employing a magnetic field results in a diamagnetic shift. The scheme introduces a new gate-defined platform for creating and controlling optically active quantum dots and opens the route to lithographically defined coupled quantum dot arrays with tunable in-plane coupling and voltage-controlled optical properties of single charge and spin states.

7.1. Introduction

Trapping atoms or ions with tailored electromagnetic fields as on microfabricated chips [Riedel et al. 2010; Blatt et al. 2008] or in optical lattices [Weitenberg et al. 2011] and thus controlling their position and number down to single particles has enabled detailed studies of quantum systems such as Bose Einstein condensates [Riedel et al. 2010], coupled ion arrays [Blatt et al. 2008] and atomic Mott insulators [Weitenberg et al. 2011]. This allowed particle entanglement [Riedel et al. 2010; Blatt et al. 2008] and yielded insight into light matter-interactions with individual quantum objects with unprecedented precision. In solid state devices, similarly, single electron manipulation in charge quantum dots [Hanson et al. 2007; Holleitner et al. 2002; Hu et al. 2007; Hermelin et al. 2011] or Bose-Einstein condensation of two-dimensional bosonic systems in equilibrium both require a trapping potential [Hohenberg 1967]. So far, optically active quantum dots, trapping few excitons, rely on three dimensional material modulation as in self-assembled quantum dots [Drexler et al. 1994; Warburton et al. 2000; Latta et al. 2011], providing limited control of confinement potential and position. Here, we demonstrate in tuneable nanoscale traps that tight electrostatic confinement of excitons creates discrete excitonic transitions observable down to a single confined exciton. Such traps combine a double quantum well with

gate-defined electrostatic potentials resulting in individual three-dimensional traps for spatially indirect dipolar excitons [Schinner et al. 2011a]. With their electron and hole confined to a different quantum well, these excitons exhibit a large dipole moment and long lifetimes. Reducing the electrostatic confinement to nanoscale dimensions we enter the few exciton regime and observe discrete spectral features, reflecting interexcitonic dipolar repulsion to cause molecular-like spatial arrangements of two and three excitons, respectively. The excitonic transitions are tuneable by gate voltages and magnetic fields and are well reproduced by a straightforward model. The scheme introduces a new gate-defined platform for creating and controlling single exciton traps and opens the route to lithographically defined arrays of artificial atoms with tuneable in-plane coupling and voltage-controlled optical properties of single charge and spin states.

In solids quantum confinement of charge carriers in all three spatial directions results in so-called quantum dots (QD), artificial atoms with discrete energy spectra. Charge quantum dots, containing unipolar charges and studied via electronic transport spectroscopy, usually utilize electrostatic fields to completely confine charge carriers of a two-dimensional (2D) electron system at a heterojunction interface [Hanson et al. 2007; Holleitner et al. 2002; Hermelin et al. 2011] or in an one-dimensional (1D) nanowire [Hu et al. 2007; Hermelin et al. 2011]. In contrast, optically active quantum dots, containing both conduction band electrons and valence band holes so far require three-dimensional material modulation by suitable growth methods as in widely studied self-assembled quantum dots [Drexler et al. 1994; Warburton et al. 2000; Latta et al. 2011] in order to confine both, electrons and holes, in the same nanoscale region as bound excitonic pairs. Thereby it is difficult to control their position to achieve scalable QD circuits and their confining potential. However, introducing charge tuneability via field-effect has enabled to visualize shell structure of single electron states and precision optical spectroscopy on individual self-assembled quantum dots in emission [Warburton et al. 2000] and absorption [Högele et al. 2004] and continues to reveal new many-body quantum phenomena [Latta et al. 2011].

In an effort to combine the advantages of the above approaches we present a scheme to define optically active quantum traps confining individual indirect dipolar excitons (IX) by electrostatic fields provided via lithographically fabricated nano-scale gates on a suitably designed double quantum well (DQW) heterostructure. By reducing the trap area and the corresponding IX occupation about 1000-fold in comparison to previous studies [Schinner et al. 2011a; High et al. 2009a] we achieve the single exciton limit for electrostatically trapped and long-living dipolar excitons. We thus are able to observe discrete emission lines for the 1 IX, 2 IX and 3 IX states reflecting quantum dot behavior dominated by the effect of dipolar repulsion between individual excitons, in excellent agreement with a model of interacting IX in a tight parabolic confinement potential. This enables position control of such QDs with lithographic precision as in charge and spin QDs. In addition, it permits electrical

tuneability of the excitonic confining potential, photoluminescence (PL) energy and lifetime, and the exciton population down to a single exciton. Based on our approach one can envision the control of individual excitons in the DQW plane within QDs or in QD arrays with gate-controlled in-plane coupling as needed for implementation in quantum information processing circuits [Loss et al. 1998; Imamoglu et al. 1999; Burkard et al. 1999; Li et al. 2003]. Furthermore IX are particularly attractive for coherent manipulation, because of their long charge and spin lifetimes [Vörös et al. 2009b; Kowalik-Seidl et al. 2010].

7.2. The quantum traps

The 3D confining scheme in the IX quantum traps is based on gate control of the Quantum Confined Stark Effect (QCSE) in the plane of a DQW as illustrated in Fig. 7.1. The electric field component $\mathbf{F}_z$ in the growth direction (z) of the coupled DQW consisting of two adjacent 7 nm wide $In_{0.11}Ga_{0.89}As$ QWs separated by center to center distance of $d = 17$ nm is tuned by a voltage V applied to semi-transparent titanium gates with respect to a n-doped GaAs back contact with Fermi-energy E_F^0 as shown in the energy diagram in Fig. 7.1(a). The e-h separation causes a red shift $\Delta E_{IX} = -\mathbf{pF}_z$ of the IX energy where $\mathbf{p} = e\mathbf{d}$ is the IX dipole moment oriented along z. The parabolic confinement V_{IX} in the $x-y$-plane (Fig. 7.1(b)) is achieved by biasing the trap gate (Fig. 7.1(c)) with a diameter of 600 nm at a negative voltage V_T with respect to the guard gate. The latter is biased close to the flat-band voltage V_{FB} at which the built-in field caused by surface states is canceled by the gate voltage. Coulomb attraction by the hole, localized beneath the center of the trap gate, binds the electron with a typical binding energy of 3 meV and prevents excitonic ionization by the external in-plane electric field. The spatial separation of the electron and hole along z reduces the overlap of the corresponding wavefunctions (Fig. 7.1(a)) resulting in a radiative lifetime of order 100 ns for the IX (see Section 7.9). Filling the QD with an increasing number of individual IXs allows the investigation of the interplay between dipolar IX-IX repulsion and spatial quantization in the QD. In addition, raising the number of hydrogen-like bosonic IXs, one enters the interesting regime, where excitonic Bose-Einstein condensation (BEC) is expected as predicted in the1960s [Blatt et al. 1962]. Recently, micrometer scale electrostatic trapping configurations were reported to realize a cooled ensemble of indirect excitons with high densities in order to implement a BEC (see Section 7.4) [Schinner et al. 2011a; Schinner et al. 2011b].

The devices are investigated in a low temperature microscope with two diffraction limited confocal objectives that can be independently positioned in a ^{3}He refrigerator at 240 mK. Using the upper objective, we create IXs under the guard gate with laser light 1.2 μm away from the trap center. The quantum trap is thus only filled with

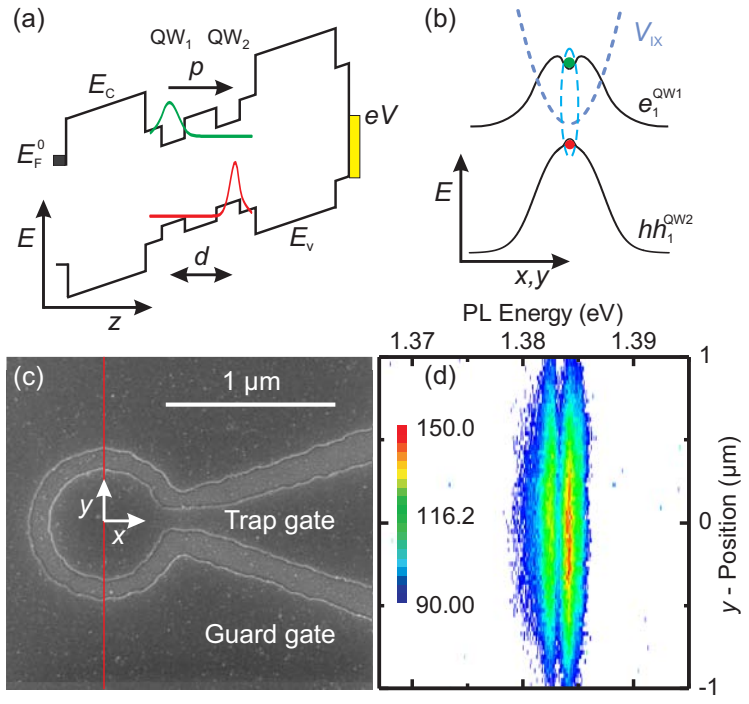

Figure 7.1.: **Trapping principle.** (a) Depicts a schematic of the DQW band gap within a field-effect device. E_c and E_v denote the conduction and valence band edge, respectively. The electron and hole wavefunction of the ground states hh_1^{QW2} and e_1^{QW1} are indicated. Note that flat band occurs at $V_T \simeq V_G \simeq 0.8\,V$ [Schinner et al. 2011a]. (b) In-plane energy of the hh_1^{QW2} and e_1^{QW1} ground state and the resulting confinement potential V_{IX} for the IX in the quantum dot. (c) Displays a scanning electron microscope (SEM) image of the gate pattern defining the quantum dot via the trap and guard gate. In (d) is shown the PL intensity in a logarithmic color scale as a function of the PL energy and y-position along a cut through the middle of the trap as indicated by the red line in (c) [$V_G = 0.75\,V$, $V_T = 0.25\,V$, $T_{Lattice} = 242\,mK$, $P_{Laser} = 2.8\,nW$, $E_{Laser} = 1.494\,eV$].

IXs pre-cooled to lattice temperatures, whereas free electrons are unable to enter the trap [Schinner et al. 2011a]. The emitted PL light is collected in transmission with a second objective located below the device and analyzed in a spectrometer. An image of the PL intensity (Fig. 7.1(d)) shows two discrete energy-resolved lines, emitted from a single exciton (1 IX) and a biexciton (2 IX) as discussed below, located in the center of the trap. They are spatially diffraction broadened to 900 nm full width at half maximum, comparable to the emitted PL wavelength.

7.3. The quantum dot trap populated with few excitons

The population of the QD can be varied by changing the laser power exciting IXs in the vicinity of the QD (Fig. 7.2(a)). For excitation laser powers up to 300 pW incident on the sample surface we observe a single narrow PL line, which we associate with an individual IX. Increasing the laser power generates two discrete PL lines (see also Fig. 7.1(d)), demonstrating the occupation of the QD with a biexciton decaying via a single IX. A further increase in excitation power creates in addition triexcitons and so on. The discrete PL lines are narrow (∼0.4 meV) but orders of magnitude broader than expected from the radiative lifetime of 300 ns. This we attribute to temporal spectral fluctuations happening during the long integration times of order 200 seconds necessary for detection. The dependence of the PL intensity on the laser

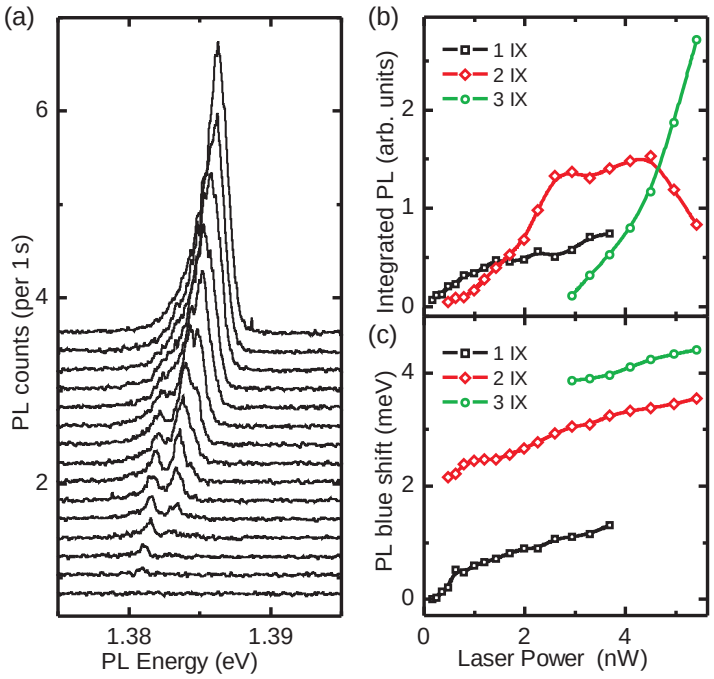

Figure 7.2.: **Laser power dependence.** (a) Illustrates typical PL spectra for different occupations of the quantum dot nonlinearly changed by laser power between 55 pW and 10 nW. In comparison to the emission from individual self-assembled InGaAs quantum dots PL counts in the single exciton limit are typically found to be 1000-fold lower, reflecting the correspondingly increased radiative lifetime of IX. The corresponding integrated PL intensity and PL blue shift is shown in (b) and (c) [V_G = 0.65 V, V_T = 0.30 V, $T_{Lattice}$ = 245 mK, E_{Laser} = 1.494 eV].

power shown in (Fig. 7.2(b)) is characteristic for a QD populated with multiexcitons [Brunner et al. 1994], rising e.g. quadratically in laser power for a biexciton. The center energies of the discrete PL lines, plotted in (Fig. 7.2(c)), reflect the interplay between dipolar interexcitonic repulsion and spatial quantization leading to a splitting of nearly 2 meV between the single exciton and biexciton configuration.

Based on a semiclassical model (see Section 7.8), we can describe the level structure by the following scenario. With the heavy hole fixed in space by the gate-induced electrostatic confining potential, somewhat roughened by the random disorder potential, the light electron in the adjacent QW is electrostatically bound to the hole via Coulomb attraction (Fig. 7.1(b)). Filling an additional IX into the narrow lateral confining potential of the QD trap causes strong excitonic repulsion by dipolar interaction. The repulsive energy of about 2 meV at a lateral interexcitonic distance of about 34 nm (see Section 7.8) dominates the energy splitting between the single IX and biexciton. Adding the third exciton yields a somewhat reduced additional repulsion of about 0.7 meV at a distance of 37 nm if we assume a triangular ordering of the excitons in the trap (see Section 7.8). The strong dipolar interactions between the few excitons in the quantum dot cause spatial order of the excitons [Laikhtman et al. 2009], in analogy to Wigner-crystal-like states expected in charge quantum dots [Bedanov et al. 1994]. This spatial order results in an excitonic Wigner-molecule (Fig. 7.3(a), (b)) and is likely to be assisted by the fact that the external excitonic potential V_{IX} has a significantly larger spatial extend than the excitons confined to Bohr radii. In addition, screening of the bare trap potential V_{IX} by adding dipolar excitons will modify the effective potential landscape. Increasing the laser power increases the time-averaged population of the trap with biexcitons and triexcitons. The resulting dipolar screening causes a blue shift ΔE, reflecting the increasing many-body interactions between the IXs and their temporal dynamics (Fig. 7.2(c)). A further increase of the laser power causes the QD to sequentially fill up to about 100 IXs (see Section 7.6). For high populations we observe an unstructured asymmetric PL lineshape characterized by a steep blue side and a long red tail (Fig. 7.2(a)). The development of the PL lineshape in Fig. 7.2(a) with the trapped exciton density shows clearly that the asymmetric PL line results from the sum of individual exciton PL lines and ends in an edge-like singularity [Skolnick et al. 1987; Hawrylak 1991] for a high density cold dipolar liquid [Schinner et al. 2011b; Laikhtman et al. 2009].

In the quantum trap device we anticipate to observe correlations because the expected excitonic coherence length [Yang et al. 2006] exceeds the diameter of the trap which is also smaller than the emitted PL wavelength. Furthermore, at low temperature (240 mK), the thermal de Broglie wavelength λ_{dB} of the bosonic particles ($\lambda_{\mathrm{dB}} = \frac{\hbar}{\sqrt{2M\pi kT}}$ where $M = m_{\mathrm{e}}^* + m_{\mathrm{hh}}^*$ is the total mass of the exciton) is a few times larger than the interexcitonic distance which is similar to the effective Bohr radius $r_{\mathrm{e}} \approx 20\,\mathrm{nm}$.

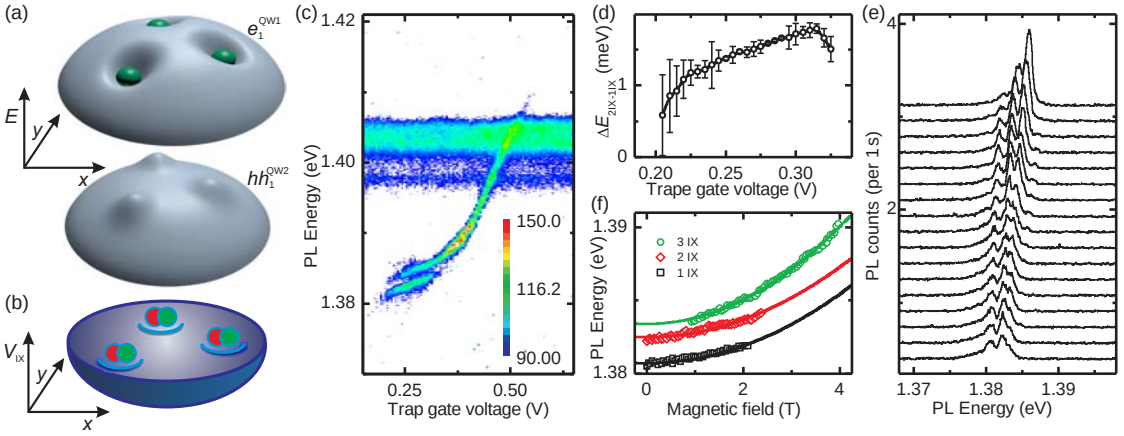

Figure 7.3.: **Wigner-molecule, trap gate and magnetic field dependence.** (a) Shows the formation of a triangular excitonic Wigner-molecule built up of three equidistantly spaced dipolar excitons confined in the QD like in Fig. 7.1(b). (b) Illustrates the corresponding confinement potential V_{IX} containing 3 IX. (c) depicts the PL intensity in a logarithmic color scale as a function of the trap gate voltage and the PL energy. With decreasing trap gate voltage the PL line splits in two. This splitting as a function of the trap gate voltage is shown in (d) [$V_{\mathrm{G}} = 0.55\,\mathrm{V}$, $T_{\mathrm{Lattice}} = 244\,\mathrm{mK}$, $P_{\mathrm{Laser}} = 2.8\,\mathrm{nW}$, $E_{\mathrm{Laser}} = 1.494\,\mathrm{eV}$]. (e) Shows characteristic spectra for different magnetic fields in equidistant steps from 0 T (bottom) to 2.5 T (top). The corresponding diamagnetic shifts of the different PL lines (symbols) and the quadratic fit (solid line) are shown in (f). From the quadratic fit we can extract an effective Bohr radius r_{e} ($r_{\mathrm{e}}^{1\mathrm{IX}} = 18.3\,\mathrm{nm}$, $r_{\mathrm{e}}^{2\mathrm{IX}} = 18.4\,\mathrm{nm}$ and $r_{\mathrm{e}}^{3\mathrm{IX}} = 21.7\,\mathrm{nm}$) [$V_{\mathrm{G}} = 0.75\,\mathrm{V}$, $V_{\mathrm{T}} = 0.25\,\mathrm{V}$, $T_{\mathrm{Lattice}} = 242\,\mathrm{mK}$, $P_{\mathrm{Laser}} = 2.8\,\mathrm{nW}$, $E_{\mathrm{Laser}} = 1.494\,\mathrm{eV}$].

The excitonic QD potential V_{IX} is tuneable by gate voltage (Fig. 7.3(c)). With decreasing trap gate voltage, the trap gets deeper and we expect a narrowing of the lateral confinement down to about 100 nm, inducing a splitting of the PL line in two discrete lines (see Section 7.5). The latter reflects an occupation of the trap with two exciton states. In Fig. 7.3(d), the energetic splitting between exciton and biexciton state is plotted versus the trap gate voltage. We interpret the lowering of the energetic spacing $E_{2\mathrm{IX}} - E_{1\mathrm{IX}}$ with decreasing trap gate voltage by the observation that the time-averaged excitonic population of the quantum trap with biexcitons, deduced from the decreasing intensity of the 2 IX PL in Fig. 7.3(c), and thus the corresponding effective excitonic repulsion weakens and overcompensates the effect of a somewhat increasing electrostatic potential V_{IX}. The splitting is accompanied by a change in the slope of the QCSE (Fig. 7.3(c)). Here, we insured that leakage currents entering the trap gate are negligibly small in the corresponding voltage regime (see Section 7.11). In traps with a larger trap gate diameter we are able to

observe a gate-voltage-dependent depletion zone of width ranging between 250 nm and 500 nm around the trap perimeter (see Section 7.5) [Schinner et al. 2011a]. Correspondingly, we expect for the trap depicted in Fig. 7.1(c) the resulting curvature of the electrostatically induced trap potential V_{IX} to dominate the random disorder potential. Generally, at a trap gate voltage $V_{\mathrm{T}} \gtrsim V_{\mathrm{G}}$, the exciton trap converts into a depopulated antitrap and we do no longer detect any PL from IXs within the trap area.

Additional manifestation of the quantum dot behavior can be deduced from the difference in the diamagnetic energy shifts of the discrete excitonic lines in a magnetic field B applied in Faraday configuration perpendicular to the QW plane. Fig. 7.3(e) displays exemplary PL spectra as a function of $\mathbf{B}$. With increasing magnetic field we observe a diamagnetic shift of the excitonic emission with the center energies plotted in Fig. 7.3(f). In addition, we observe an increasing PL intensity and the appearance of a triexciton line at higher field. Both findings reflect an increasing stabilization of excitons by the magnetic field. Without magnetic field, a large in-plane component of the electrostatic field near the trap perimeter can cause ionization of the IX. As experimentally observed inside QWs [Zimmermann et al. 1997] and theoretically predicted [Govorov et al. 1998], such radial tunneling of the excitonically bound electrons out of their pocket in the binding potential (Fig. 7.1(b) and Fig. 7.3(a)) can be suppressed by a magnetic field along z. For the spectra in Fig. 7.3(e), this causes both the observed increase in PL intensity and the appearance of a strong triexciton line with increasing $\mathbf{B}$. The resulting quadratic diamagnetic shift of the trapped IXs energies (plotted in Fig. 7.3(f)) is given by $\Delta E_{\mathrm{dia}} = \frac{e^2 r_{\mathrm{e}}^2}{8\mu c^2} B^2$ where r_{e} is the effective Bohr radius and μ the reduced mass of the exciton [Stern et al. 2008a]. With increasing exciton number, we see an increase in r_{e} because the effective confining potential is broadened by screening and strong IX interactions.

7.4. The electrostatic trapping principle of the quantum traps

To create electrostatic traps we use the in-plane variation of the local Stark electric field $\mathbf{F}_{\mathrm{z}}(x, y)$ acting perpendicular to the double quantum well (DQW) in order to generate a potential landscape for the indirect excitons (IXs). Such highly tuneable traps were realized in various geometries [Zimmermann et al. 1997; Zimmermann et al. 1998; Huber et al. 1998; Rapaport et al. 2005; Timofeev et al. 2007; Hammack et al. 2006a; Chen et al. 2006; High et al. 2009a; High et al. 2009b; Schinner et al. 2011a]. Other possibilities to realize three-dimensional exciton confinement are: strain-induced traps [Trauernicht et al. 1983; Kash et al. 1988; Negoita et al. 1999], magnetic traps [Christianen et al. 1998], natural traps due to random disorder in the QW-plane [Butov et al. 2002] or silicon-dioxide traps [Gärtner et al. 2007; Vögele et

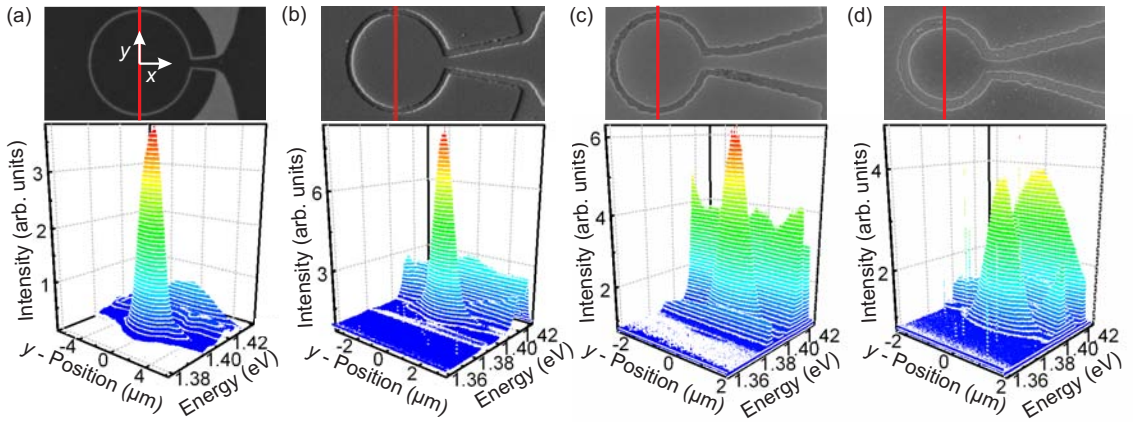

Figure 7.4.: **Circular traps with different diameters.** The figure shows a series of scanning electron microscope (SEM) images of circular traps consisting of a central trap gate, with different diameters d_{trap}, which are surrounded by a guard gate. In the lower row of pseudo-3D pictures, the photoluminescence intensity is shown energetically and spatially resolved. The cuts are taken along the y-direction through the middle of the trap as indicated by the red line in the SEM images. The exciton generation by a focused pump laser occurs a distance x_{Laser} left of the trap center below the guard gate. (a) [d_{trap} = 4000 nm, x_{Laser} = -5 μm, V_{G} = 0.60 V, V_{T} = 0.35 V, T_{Lattice} = 4 K, E_{Laser} = 1.959 eV, P_{Laser} = 10 μW]; (b) [d_{trap} = 1800 nm, x_{Laser} = -5 μm, V_{G} = 0.55 V, V_{T} = 0.20 V, T_{Lattice} = 8 K, E_{Laser} = 1.959 eV, P_{Laser} = 2 μW]; (c) [d_{trap} = 1000 nm, x_{Laser} = -4 μm, V_{G} = 0.55 V, V_{T} = 0.20 V, T_{Lattice} = 245 mK, E_{Laser} = 1.959 eV, P_{Laser} = 2 μW]; (d) [d_{trap} = 800 nm, x_{Laser} = -1.8 μm, V_{G} = 0.55 V, V_{T} = 0.20 V, T_{Lattice} = 247 mK, E_{Laser} = 1.494 eV, P_{Laser} = 2 μW].

al. 2009a]. Electrostatic traps exhibit the highest tunability and trapping efficiency. To achieve a quantitative understanding in the functionality of our gate-defined traps we investigated a series of circular traps with gate diameters of the central trap gate ranging from 24 μm down to 90 nm. The gate layout of the circular traps is always comparable and is patterned by e-beam lithography. The central circular trap gate is surrounded by a guard gate which is separated from a trap gate by a 100 nm narrow (slit) ungated region for insulation. Suitably biased by voltage V_{G} below the flat band voltage of V_{FB} it defines the outside surface potential to enable the formation of IXs and creates a depletion zone [Wiemann et al. 1998; Hermelin et al. 2011] around the trap gate perimeter, thus providing the confinement for IX. Fig. 7.4 shows a series of circular traps with diameters of 4000 nm, 1800 nm, 1000 nm

and 800 nm. The semitransparent gates are 6 nm thick evaporated Ti films. The traps are investigated in a fiber based low temperature microscope, composed of two diffraction limited confocal objectives, embedded in a ^{3}He refrigerator at variable temperatures down to 240 mK [Schinner et al. 2011b]. The exciton generation by a focused pump laser occurs left of the trap on the guard gate. After a short relaxation and cool-down time of less than 1 ns a large fraction of the equilibrated indirect exciton gas enters the energetically favorable trap area for $V_T < V_G$ [Hammack et al. 2009]. The trapping potential is attractive for indirect excitons but repels unbound electrons [Schinner et al. 2011a]. The pseudo-3D pictures in Fig. 7.4 display the measured PL intensity as a function of the PL energy and y-direction in a cut through the middle of the trap as indicated by the red line in the corresponding scanning electron microscope picture. The PL light is collected in transmission with a second confocal objective positioned below the sample. As reflected by the strong indirect exciton PL signal from the trapping area the trap provides a perfect confinement for indirect excitons.

7.5. Confinement potential of circular traps

To characterize the confinement potential for IXs in a typical trap, we first discuss spatially resolved images of the PL energy of the trap with $d_{\mathrm{trap}} = 4000$ nm (Fig. 7.5(a)), a diameter well above the resolution limit of our confocal optics which is comparable to the PL wavelength. In the case of a deep trap with a confinement of 25 meV caused by a low trap gate voltage a parabolic confinement potential is observed (Fig. 7.5(a)). For a shallow trap (6 meV), with a relatively high trap gate voltage and a small voltage difference between the guard and trap gate, a box-like trapping potential is measured (Fig. 7.5(b)), as predicted by simple electrostatic calculations (Fig. 7.5(c)). For circular traps with a diameter exceeding 4000 nm a box-like indirect exciton potential with flat bottom is observed as expected [High et al. 2009b; Schinner et al. 2011a]. The potential landscape resulting from a given gate layout is strongly influenced by the thickness and the position of the coupled double quantum well (DQW) plane inside the field effect device [Rapaport et al. 2005]. We positioned the DQW in the middle of the field-effect device. A position close to the heterostructure surface causes strong lateral electric fields in the quantum well plane resulting in exciton ionization on the trap perimeter. With increasing distance from surface gates, defining the trap geometry, the in-plane potential is blurred because of the exponential decay of the Fourier components [Laux et al. 1988]. Solving the Laplace equation for a 4000 nm diameter circular trap depicts a box-like excitonic potential (Fig. 7.5(c)). In deeper traps an increasing depletion around the trap perimeter is calculated (Fig. 7.5(c)). The boundary condition for these calculations is a homogenous dielectric medium between a metallic infinite back-contact and the top gate structure. The real excitonic potential plotted in Fig.

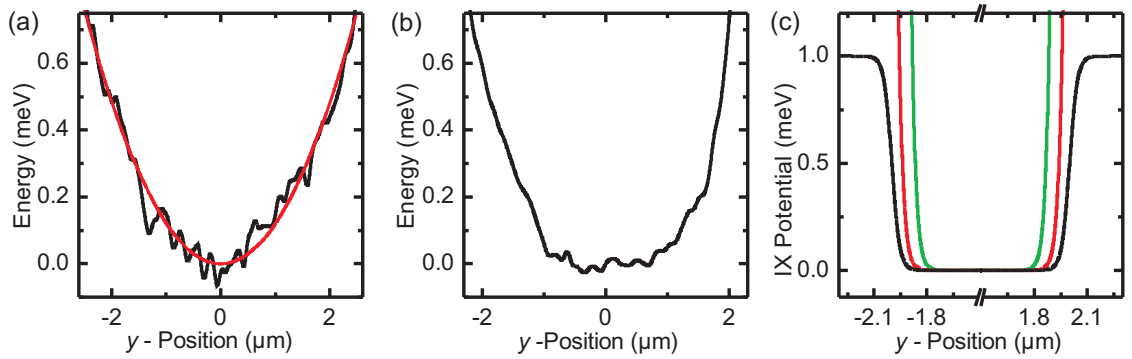

Figure 7.5.: **Confinement potential of a circular trap.** In (a) the measured confinement potential of a 25 meV deep trap and a corresponding parabolic fit of a circular trap with a diameter of 4000 nm (see Fig. 7.4(a)) is plotted [$d_{\mathrm{trap}} = 4000\,\mathrm{nm}$, $x_{\mathrm{Laser}} = \text{-}5\,\mu\mathrm{m}$, $V_{\mathrm{G}} = 0.60\,\mathrm{V}$, $V_{\mathrm{T}} = 0.20\,\mathrm{V}$, $T_{\mathrm{Lattice}} = 4\,\mathrm{K}$, $E_{\mathrm{Laser}} = 1.959\,\mathrm{eV}$, $P_{\mathrm{Laser}} = 9\,\mu\mathrm{W}$]. (b) Shows the measured confinement potential of the same trap with 6 meV energy difference between guard and trap exciton potential [$V_{\mathrm{G}} = 0.60\,\mathrm{V}$, $V_{\mathrm{T}} = 0.50\,\mathrm{V}$ and all other parameters like (a)]. (c) Shows the calculated confinement potential of a comparable trap with a deepness of 1 meV (black), 8 meV (red) and 40 meV (green).

7.5(a) shows a stronger depletion, as theoretically expected, resulting in a parabolic confinement potential in the case of a deep trap. The reason for the differences to the calculated trapping potential is that the assumptions for the numeric solution disregard that we have a semiconductor layer system with an unknown background doping and a doped semiconductor back-contact containing a finite charge carrier density. In the case of the back-contact, it is expected that the applied electric field causes a depletion. We point out that the depletion around the perimeter of the trap gate is the reason that no leakage of indirect excitons at the trap gate lead is observed. In two samples with a circular trap having a diameter of 600 nm we measured a comparable quantum dot confinement. We further find experimentally that circular traps with diameters equal and smaller than 400 nm are not able to trap excitons within the studied gate-voltage regime.

7.6. The quantum dot trap populated with many excitons

An energetically deep circular trap with a trap gate diameter of 600 nm (Fig. 7.6(a)) results in a quantum dot, for low exciton population. In Fig. 7.6(b), (c) the energet-

ically and spatially resolved PL intensity is logarithmically color coded. The cuts are taken in x- and y-direction through the middle of the trap center. The exciton generation occurs by a strongly focused pump laser about 1.2 μm away from the trap center below the guard gate. The energetically highest PL signal in Fig. 7.6 is PL light emitted from direct quantum well excitons at $\sim$ 1.425 eV. They have a short lifetime, recombining on a nanoseconds time scale [Feldmann et al. 1987].

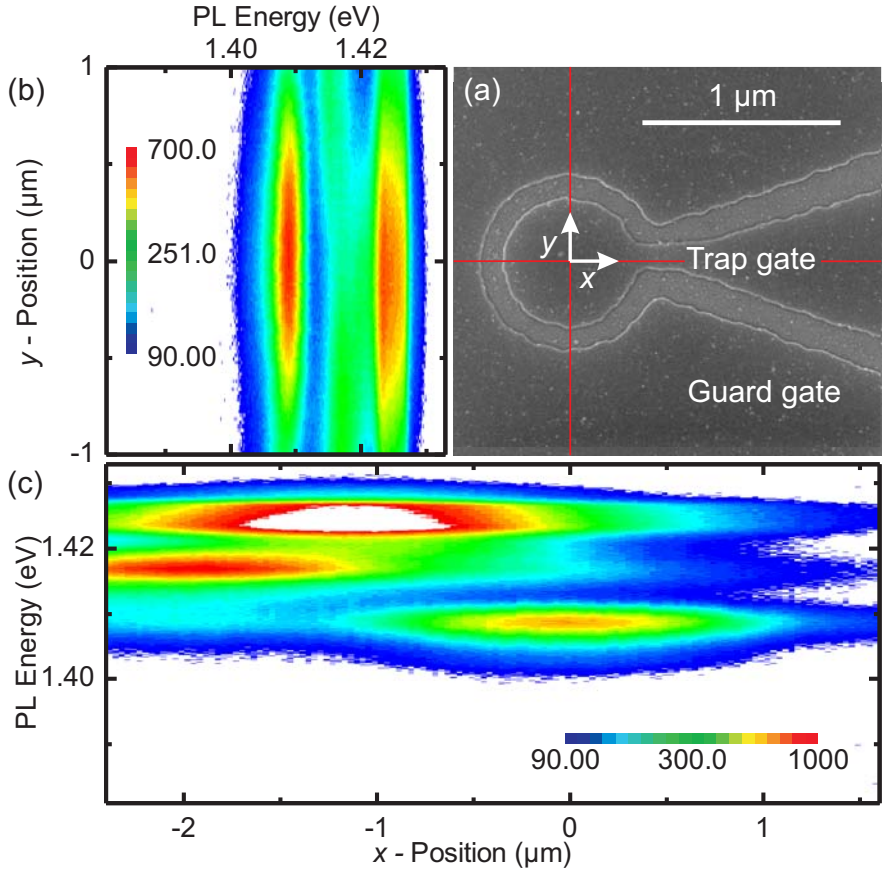

Figure 7.6.: **The figure shows spatially and energy resolved measurements of the exciton distribution in the quantum dot trap populated with many excitons.** In (b) and (c) cuts are shown of the PL intensity in a logarithmic color scale, given by the scale bar, as a function of the position and PL energy. The data are measured along cuts indicated by the red lines in the scanning electron micrograph shown in (a) of the QD trap with a trap gate diameter of 600 nm [$d_{\mathrm{trap}} = 600\,\mathrm{nm}$, $x_{\mathrm{Laser}} =$ -1.2 μm, $V_{\mathrm{G}} = 0.65\,\mathrm{V}$, $V_{\mathrm{T}} = 0.40\,\mathrm{V}$, $T_{\mathrm{Lattice}} = 245\,\mathrm{mK}$, $E_{\mathrm{Laser}} = 1.494\,\mathrm{eV}$, $P_{\mathrm{Laser}} = 200\,\mathrm{nW}$].

Hence, they exist only in the vicinity of the generation focus. The PL energetically below the direct exciton PL at ∼1.417 eV results from indirect excitons under the guard gate. The energetically lowest PL light is emitted from long living IXs trapped in the high populated quantum dot at ∼1.409 eV. The areal distribution of the trapped IX PL is spatially diffraction broadened to 1200 nm full width at half maximum. This value is about 300 nm broader than the spatial width observed for occupying the QD with a single IX (see Fig. 7.1(d)). We expect that the electrostatic trapping potential is modified by screening effects via the aligned dipole moments of the trapped indirect exciton ensemble. The consequence is a broadening of the trapping potential, and the population of the QD with many excitons results in a strong blue shift leading to a more shallow trapping potential.

A change of the QD population can easily be studied by changing the excitation laser power. In Fig. 7.7 the overall integrated trap PL intensity is displayed logarithmically as a function of the PL blue shift ΔE as well as a rough estimate of the corresponding exciton density as detailed below. The blue shift ΔE is measured relative to the PL energy of a single indirect exciton. For higher populations of the QD, the maximum PL energy of the strongest emitting PL line is used to calculate the blue shift belonging to the total intensity detected from the QD. The lowest PL intensity is emitted from a single 1 IX which experiences only the electric field created by the gates and causing the confinement potential. A biexciton 2 IX in the QD produces a step like increase in the PL maximum energy by about 2 meV via dipolar repulsion (Fig. 7.7 or Fig. 7.2(c)). The dipole moments of all trapped individual

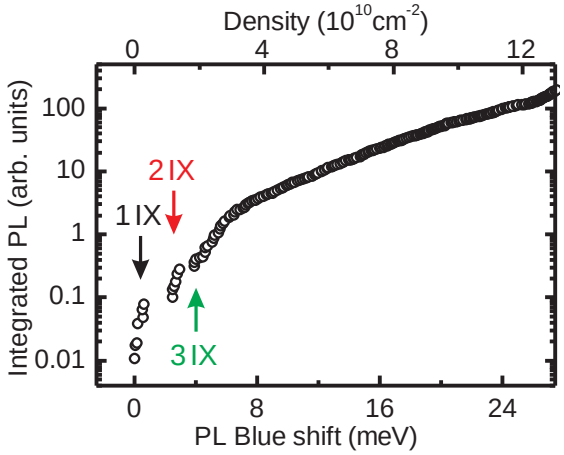

Figure 7.7.: **Emitted PL intensity versus PL blue shift.** The integrated PL intensity is logarithmically plotted as a function of the PL blue shift and the corresponding calculated trapped indirect exciton density [d_{trap} = 600 nm, x_{Laser} = -1.2 μm, V_{G} = 0.65 V, V_{T} = 0.30 V, T_{Lattice} = 247 mK, P_{Laser} = 150 pW...850 nW, E_{Laser} = 1.494 eV].

IXs are aligned and perpendicular to the QW-plane. From the dipole interaction energy of 2 meV, a lateral interexcitonic distance $r_{\mathrm{IX}} = 26\,\mathrm{nm}$ is calculated by using $W = \frac{p^2}{\epsilon r_{\mathrm{IX}}^3}$ where $\mathbf{p} = e\mathbf{d}$ is the IX dipole moment resulting from the electron-hole separation by a distance $\mathbf{d}$ in the two adjacent quantum wells and ϵ is the dielectric constant. r_{IX} is slightly larger than the effective Bohr radius $r_{\mathrm{e}} = 21.7\,\mathrm{nm}$ which is extracted from the diamagnetic energy shift by a quadratic fit (see Fig. 7.3(f)). For a QD populated with a triexciton 3 IX a blue shift of 3 meV is measured (Fig. 7.7 or Fig. 7.2(c)). Taking the assumption that all three excitons are equidistantly spaced an interexcitonic distance of $r_{\mathrm{IX}} = 28\,\mathrm{nm}$ is calculated. And for 3 IX an effective Bohr radius of $r_{\mathrm{e}} = 21.7\,\mathrm{nm}$ is found (Fig. 7.3(f)).

The strong dipolar interactions between the trapped IXs in the quantum dot can cause spatial order of the excitons, in analogy to a Wigner-crystal. This spatial order is likely to be assisted by the fact that the external excitonic potential has a significantly larger spatial extent than the excitons confined to the Bohr radii. In the case that the electron wavefunctions show a strong overlap for $r_{\mathrm{e}} > r_{\mathrm{IX}}/2$, one can anticipate to observe correlations because the expected excitonic coherence length [Yang et al. 2006] exceeds the diameter of the trap. Furthermore, the thermal de Broglie wavelength λ_{dB} of the bosonic particles is larger than r_{IX} which is similar to the effective Bohr radius r_{e}.

For higher exciton populations of the QD, the effective electric field, seen by the individual dipolar indirect exciton is the sum of the externally applied electric field and the depolarizing dipole field of all other IXs in the vicinity. With increasing exciton density, the effective electric field decreases due to screening and causes a blue shift ΔE. From ΔE it is possible to calculate the corresponding exciton density. The simplest approach is that the indirect exciton density is given by $n = \frac{\epsilon}{4\pi e^2 d}\Delta E$ [Schinner et al. 2011a]. This equation likely underestimates the density, especially in the low density limit as theoretically calculated by [Zimmermann et al. 2007; Schindler et al. 2008; Ivanov et al. 2010]. In the special case of the QD, however, we used this formula to convert the blue shift in the density given on top of Fig. 7.7.

We expect that the electrostatic trapping potential is modified by the screening effects caused by the aligned dipole moments of the trapped indirect exciton ensemble. The consequence is a broadening of the trapping potential and a more shallow confinement potential. In the case of a high exciton density in the quantum dot (Fig. 7.6), a populated trap area with a diameter of about 300 nm is estimated. Electrostatic calculations show a trap diameter of 350 nm to 400 nm. From these values we calculate a maximum QD population of approximately 90 up to 150 trapped indirect excitons at high laser powers.

In Fig. 7.7 the trapped exciton number increases by a factor of 10^2. In contrast, the emitted PL intensity changes by more than a factor 10^4 and it shows two different slopes. A part of this exponential increasing intensity as a function of the raising

trapped exciton number can be explained with a decreasing lifetime [Schinner et al. 2011a]. The rest is associated with a collective behavior of the exciton ensemble and we believe that correlations in the bosonic exciton gas start to be important.

7.7. Asymmetry of the lineshape at large exciton occupation

At the low temperatures of our experiment the kinetic energy of the excitons is negligible in comparison to the typical energies of interexcitonic dipolar repulsion [Yoshioka et al. 1990; Laikhtman et al. 2009]. At $T = 0\,\mathrm{K}$ this repulsion causes the exciton state with the highest occupation N to have the highest transition energy and strongest oscillator strength and defines the blue edge of the total IX emission. States of $N - M$ excitons with $M = 1, 2, \ldots N$ excitons occur with increasing M at successively lower energies but still contribute to the emission spectrum via the recombination cascade. Assuming constant dipolar repulsion this results in a two-dimensional exciton systems with a joint optical density of states proportional to energy $E_N - E_0$. Furthermore, one can expect the radiative lifetime of the $N - M$ state to rise with increasing M, thus causing a strongly asymmetric $T = 0$ lineshape. Additional inhomogeneous broadening caused by temporal fluctuation of the electrostatic background will smear the blue edge and merge the energetically lower lying transitions in the recombination cascade without much affecting the red tail of the PL lineshape.

7.8. Modeling the energy spectra in a few-exciton trap

We now estimate optical energies of few-exciton states in a trap by using the Wigner-crystal-like model (Fig. 7.8). Such a model has been applied to few-electron states in electron quantum dots [Bedanov et al. 1994; Wendler et al. 1996] and is extended here to parallel aligned and spatially ordered dipolar excitons [Yoshioka et al. 1990; Laikhtman et al. 2009]. In this quasi-classical approach, in which overlap of the excitonic wavefunctions is neglected, the total exciton energy in a trap is written in the following way:

$$E_{\mathrm{exc},\,N_{\mathrm{exc}}} = N_{\mathrm{exc}} E^0_{\mathrm{IX}} + \sum_i \frac{M\Omega^2_{\mathrm{exc}}}{2} r_i^2 + \sum_{\substack{i<j \\ i,j=1\ldots N_{\mathrm{exc}}}} \frac{p^2}{\epsilon r_{ij}^3}, \tag{7.1}$$

where N_{exc} is the number of excitons in a trap, E^0_{IX} is the optical energy of the exciton in an uniform 2D well, Ω_{exc} is the characteristic confinement frequency of

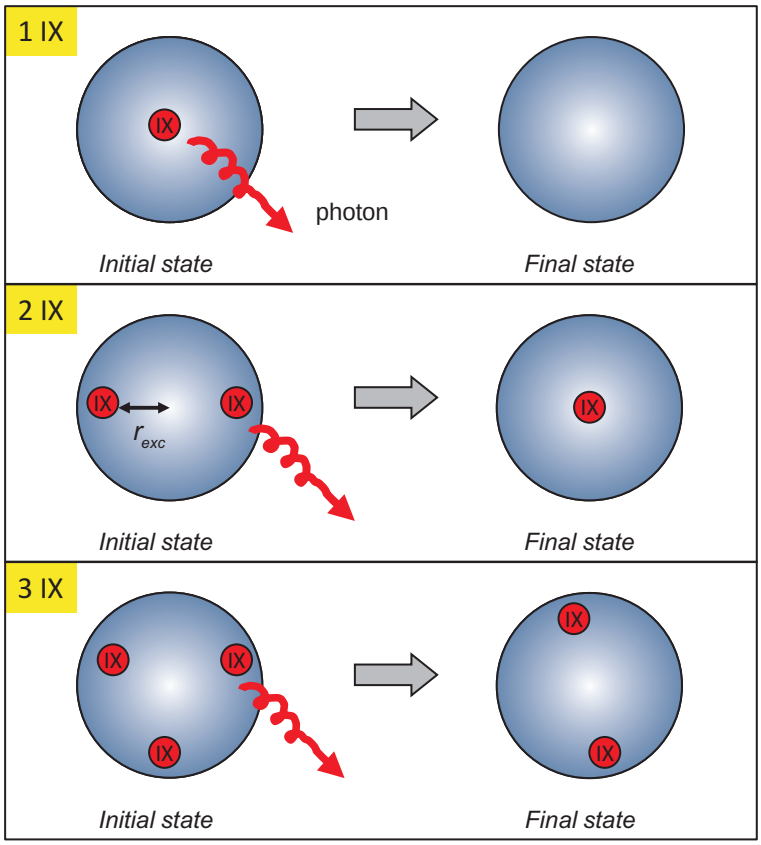

Figure 7.8.: **Wigner-molecule representation of exciton complexes.** An emission process brings a multiple exciton (2 IX, 3 IX, ...) into a long-lived, fully-relaxed ground state.

an exciton in a parabolic trap, $M = m_e^* + m_{hh}^*$ is the exciton mass, p is the exciton dipole, and r_i is a coordinate of i-exciton in a trap. Then, the ground state should be found as a minimum of the total energy $E_{\mathrm{exc},N_{\mathrm{exc}}}$. Since excitons have enough time to relax, this ground state should be considered and it is the initial state for the photon emission process (Fig. 7.8). For the first three excitonic complexes ($N_{\mathrm{exc}} = 1 - 3$), the ground states are shown in Fig. 7.8 and they can easily be calculated from Eq. 7.1. The equilibrium positions of correlated excitons are determined by the interplay of the parabolic confining potential and the dipole repulsion. The emission process can be considered as a fast removal of one of the correlated excitons and ends in a final state of $(N_{\mathrm{exc}} - 1)$ IX. Now we calculate the emission energy of N_{exc} IX which is an energy difference

$$\hbar\omega_{N_{\mathrm{exc}}} = E_{\mathrm{initial},\,N_{\mathrm{exc}}}(r_{i,\,N_{\mathrm{exc}}}) - E_{\mathrm{final},\,N_{\mathrm{exc}}-1}(r_{i,\,N_{\mathrm{exc}}-1}), \tag{7.2}$$

where $E_{\mathrm{initial},\,N_{\mathrm{exc}}}$ is the energy found as the minimum of Eq. 7.1 and $r_{i,\,N_{\mathrm{exc}}}$ are the equilibrium positions of the excitons in the initial state with a minimized energy.

$E_{\text{final},\,N_{\text{exc}}-1}$ is the total energy of the final state calculated as a minimum of Eq. 7.1 for the system of $(N_{\text{exc}}-1)$ excitons with positions $r_{i,\,N_{\text{exc}}-1}$. Figure 7.8 illustrates the physical situation.

The initial state of 1 IX is a single exciton localized in the center of trap, whereas the final state of 1 IX after the emission process is, of course, a band structure ground state. This case is really simple and its emission energy is: $\hbar\omega_{N_{\text{exc}}=1} = E^0_{\text{IX}}$. For 2 IX, we should first minimize the total energy and find the equilibrium positions of the excitons. Then, we can find the emission energy. The calculations along these lines yield:

$$r_{\text{exc},\,N_{\text{exc}}=2} = \sqrt[5]{\frac{3}{16\epsilon}\frac{p^2}{M\Omega^2_{\text{exc}}}}, \tag{7.3}$$

$$E_{\text{initial},\,N_{\text{exc}}=2}(r_i) = E_{\text{exc},\,N_{\text{exc}}=2} = 2E^0_{\text{IX}} + 2\frac{M\Omega^2_{\text{exc}}}{2}r^2_{\text{exc},\,N_{\text{exc}}=2} + \frac{p^2}{8\epsilon r^3_{\text{exc},\,N_{\text{exc}}=2}}. \tag{7.4}$$

The final state energy is

$$E_{\text{final},\,N_{\text{exc}}=1}(r_i) = E^0_{\text{IX}}. \tag{7.5}$$

Then, the optical emission energy becomes:

$$\hbar\omega_{N_{\text{exc}}=2} = E^0_{\text{IX}} + 2\frac{M\Omega^2_{\text{exc}}}{2}r^2_{\text{exc},\,N_{\text{exc}}=2} + \frac{p^2}{8\epsilon r^3_{\text{exc},\,N_{\text{exc}}=2}}. \tag{7.6}$$

For 3 IX, the ground-state configuration is of triangular geometry. The corresponding parameters of the exciton complex are

$$E_{\text{exc},\,N_{\text{exc}}=3} = 3E^0_{\text{IX}} + 3\frac{M\Omega^2_{\text{exc}}}{2}r^2_{\text{exc},\,N_{\text{exc}}=3} + 3\frac{p^2}{\alpha^3\epsilon r^3_{\text{exc},\,N_{\text{exc}}=3}}, \tag{7.7}$$

$$r_{\text{exc},\,N_{\text{exc}}=3} = \sqrt[5]{\frac{3}{\alpha^3\epsilon}\frac{p^2}{M\Omega^2_{\text{exc}}}}, \tag{7.8}$$

where $\alpha = \sqrt{3}$. The optical energy becomes:

$$\begin{aligned}\hbar\omega_{N_{\text{exc}}=3} &= E_{\text{exc},\,N_{\text{exc}}=3} - E_{\text{exc},\,N_{\text{exc}}=2} \\ &= E^0_{\text{IX}} + \frac{M\Omega^2_{\text{exc}}}{2}(3r^2_{\text{exc},\,N_{\text{exc}}=3} - 2r^2_{\text{exc},\,N_{\text{exc}}=2}) + 3\frac{p^2}{\alpha^3\epsilon r^3_{\text{exc},\,N_{\text{exc}}=3}} - \frac{p^2}{8\epsilon r^3_{\text{exc},\,N_{\text{exc}}=2}}.\end{aligned} \tag{7.9}$$

We now can calculate the optical energies for the three complexes. Using the overall realistic parameters, $\Omega_{\text{exc}} = 0.8\,\text{meV}$ and $M = 0.5\,m_0$, $\frac{p}{|e|} = 17\,\text{nm}$, and $\epsilon = 12$, we can obtain a reasonable agreement with the experimental data for the emission spectrum:
$\hbar\omega_{N_{\text{exc}}=1} = E^0_{\text{IX}}$
$\hbar\omega_{N_{\text{exc}}=2} = E^0_{\text{IX}} + 2.1\,\text{meV}$

$\hbar\omega_{N_{\mathrm{exc}}=3} = E^0_{\mathrm{IX}} + 2.8\,\mathrm{meV}$.
We note that the only fitting parameter here was the confining potential, $\Omega_{\mathrm{exc}} = 0.8\,\mathrm{meV}$. The corresponding radii of exciton complexes are:
$r_{\mathrm{exc},\,N_{\mathrm{exc}}=1} = 0$
$r_{\mathrm{exc},\,N_{\mathrm{exc}}=2} = 34.5\,\mathrm{nm}$
$r_{\mathrm{exc},\,N_{\mathrm{exc}}=3} = 37.5\,\mathrm{nm}$.
The above numbers exceed an estimated Bohr radius of an exciton thus validating our model. We see that the energy spacing between the consequent excitonic states decreases (Fig. 7.9). This is a property of a parabolic trap. For a hard-wall trap, we obtain a qualitatively different spectrum. In a hard-wall trap due to the Coulomb repulsion, the radial coordinates of excitons for 2 IX and 3 IX are fixed by the hard walls, $r_i = R_{\mathrm{trap}}$. The excitons tend to be as far as possible from each other and, therefore, they are located at the walls. The ground state configurations are a diatomic molecule and a triangle (like in Fig. 7.8). Then, the optical energies are calculated as:
$\hbar\omega_{N_{\mathrm{exc}}=1} - E^0_{\mathrm{IX}} = 0$
$\hbar\omega_{N_{\mathrm{exc}}=2} - E^0_{\mathrm{IX}} = \frac{p^2}{8\epsilon R^3_{\mathrm{trap}}} \approx 1.97\,\mathrm{meV}$
$\hbar\omega_{N_{\mathrm{exc}}=3} - E^0_{\mathrm{IX}} = 2\frac{p^2}{\alpha^3\epsilon R^3_{\mathrm{trap}}} \approx 7.1\,\mathrm{meV}$
assuming the trap diameter $2R_{\mathrm{trap}} = 26\,\mathrm{nm}$. We see here a striking difference to the case of parabolic trap. The energy intervals for the consequent exciton lines increase with the number of excitons (Fig. 7.9). In a hard-wall trap, the Coulomb repulsion energy builds up with increase of number of excitons since the exciton system should occupy a fixed area. Therefore, the inter-particle distance decreases and Coulomb

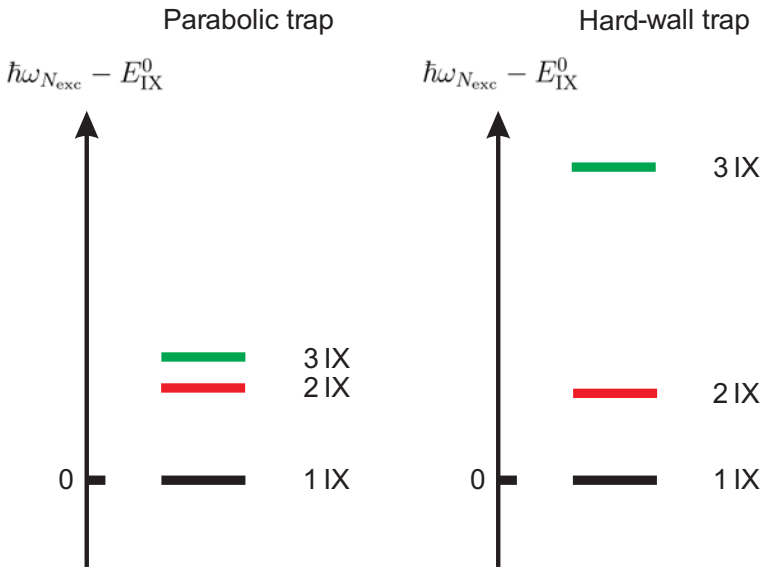

Figure 7.9.: **Quantum dot level structure.** Qualitative diagrams for the spectra of excitons, N_{exc} IX, confined in the parabolic and hard-wall traps.

correlations grow. As a result, the energy interval between the excitonic peaks in a spectrum increases with N_{exc}. In contrast, a parabolic trap has "soft" walls and the size of an excitonic complex increases with the number of excitons in a trap. Therefore, the increase in the correlation energy is somewhat smaller after addition of an exciton. This results in a different multi-exciton spectrum in which an energy interval decreases with increasing the exciton number (Fig. 7.9). A qualitative agreement between the theory and the experiment gives us another argument that the traps in our experimental samples are parabolic-like.

7.9. Lifetime of trapped indirect excitons

The lifetime of an indirect exciton depends strongly on the overlap of the tails of the electron and hole wavefunction forming the IX. We explore the temporal dynamics of the trapped indirect exciton ensemble in time resolved PL spectra. Replacing the continuous-wave laser by a pulsed laser with the same emission wavelength, we excite excitons in the vicinity of the trap under the guard gate as in Fig. 7.6. From the time-resolved PL spectra the PL maximum energy is extracted in order to calculate the trapped exciton density, as a function of delay time, by using the simple equation mentioned above with $n(t) \sim \Delta E(t)$ (Fig. 7.10(a)). The density shows an exponential decay with a time constant $\tau_{\mathrm{n}} = (302 \pm 7)\,\mathrm{ns}$. The corresponding PL intensity in Fig. 7.10(b) shows a decay constant of $\tau_{\mathrm{I}} = (99 \pm 5)\,\mathrm{ns}$, a factor 3 different from τ_{n}. In the time-resolved measurements, our sensitivity is too low to detect the few-exciton regime and therefore we expect that the real exciton density is 30% higher. The long IX lifetimes also demonstrate that even in the narrow confinement potential exciton ionization is rather unlikely. One reason for the different time constants is that with decreasing density, corresponding to $\Delta E(t)$, the indirect exciton lifetime increases. According to Ref. [Schinner et al. 2011a], it is possible to define a time-dependent effective lifetime $\tau_{\mathrm{eff}}(t) \sim n(t)/I(t)$ as the ratio of density and emitted intensity. In Fig. 7.10(c) this effective lifetime increases with raising delay time and accordingly with decreasing trapped exciton density. The effective lifetime as a function of the exciton density is shown in Fig. 7.10(d). To extract $\tau_{\mathrm{eff}}(n)$ the continuous-wave excitation data illustrated in Fig. 7.7 are used. With increasing exciton density the ratio of density and intensity and hence $\tau_{\mathrm{eff}}(n)$ decreases over more than two orders of magnitude. From the result that τ_{eff} increases with decreasing exciton densities (Fig. 7.10(c), (d)) we anticipate that for a few trapped IXs the lifetime is much longer than the observed one. An increasing exciton density (Fig. 7.10(d)) is accompanied by a strong blue shift caused by the screening of the external applied electrical field. This reduction in the effective Stark field causes a strongly increasing overlap of the tails of the electron and hole wavefunctions forming the IX thus increasing the oscillator strength, and decreasing the lifetime $\tau_{\mathrm{eff}}(n)$. In addition, one can expect that at high exciton densities, collective properties and

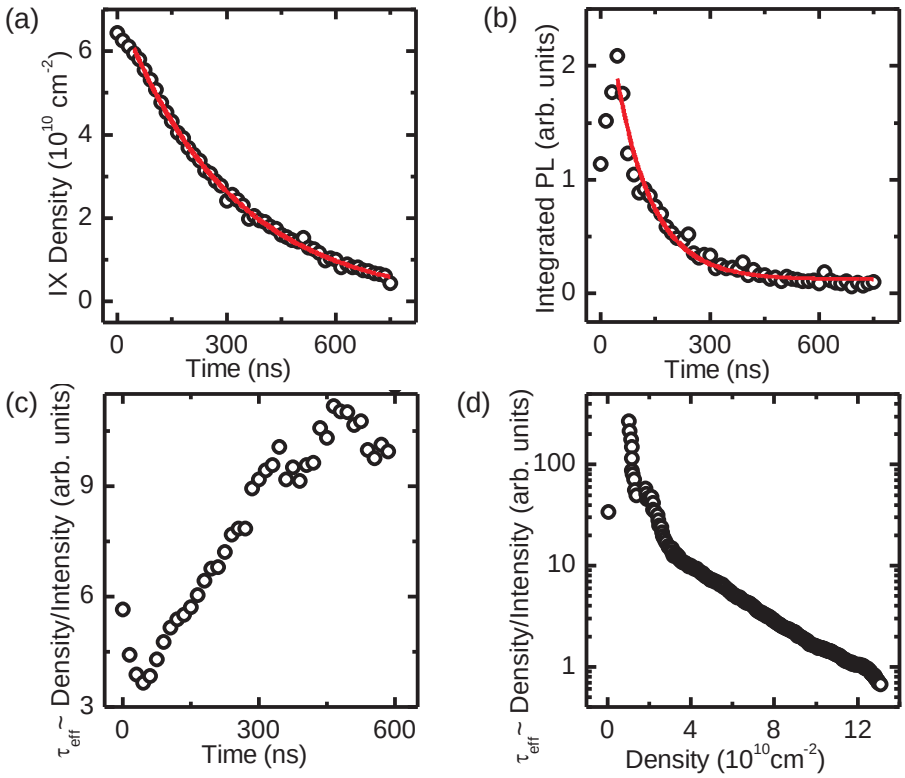

Figure 7.10.: **Time resolved measurement of the exciton population.** It is plotted the decay of the exciton density in (a), and in (b) the decay of the integrated PL intensity, as a function of time after a 40 ns excitation laser pulse. Red lines are mono exponential decay fits. In (c) the effective exciton lifetime extracted from the data shown in (a) and (b) as a function of time is plotted. The effective exciton lifetime, extracted from the data shown in Fig. 7.7, is plotted as a function of the trapped exciton density in (d) [$d_{\mathrm{trap}} = 600\,\mathrm{nm}$, $x_{\mathrm{Laser}} = \text{-}1.2\,\mu\mathrm{m}$, repetition rate 500 kHz, $V_{\mathrm{G}} = 0.65\,\mathrm{V}$, $V_{\mathrm{T}} = 0.25\,\mathrm{V}$, $T_{\mathrm{Lattice}} = 250\,\mathrm{mK}$, $P^{\mathrm{cw}}_{\mathrm{Laser}} = 1.8\,\mu\mathrm{W}$, $E_{\mathrm{Laser}} = 1.494\,\mathrm{eV}$].

correlated behavior, induced by the low temperatures (240 mK), modify the emission properties of the trapped excitonic ensemble similar to the nonlinear gain observed in exciton-polariton condensates [Balili et al. 2007].

7.10. Temperature dependence

Comparable to gate defined charge quantum dots with a small charging energy, the quantum dot characteristics are only visible at low temperatures. In Fig. 7.11 the

temperature dependence of the photoluminescence spectra emitted from the quantum dot is plotted. With increasing temperature, the discrete PL lines broaden and merge, resulting in an unstructured somewhat asymmetric PL lineshape. At elevated temperatures, thermally activated scattering processes are expected. Possible interactions are IX-phonon scattering, IX-IX scattering and shake up processes, causing the broadened spectra. In addition, as the thermal energy gets comparable to the characteristic spatial quantization energy of the IX, the IX become increasingly delocalized in the trap. The Wigner-molecule unbinds, causing a broadening of the PL lineshape, particularly on the high energy side.

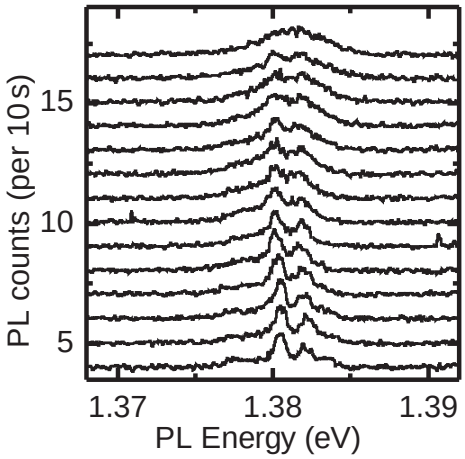

Figure 7.11.: **Temperature dependence of the quantum dot photoluminescence.** Energy resolved PL spectra for different temperatures in equidistant steps from 250 mK (bottom) to 6.75 K (top) are shown [V_G = 0.55 V, V_T = 0.25 V, P_{Laser} = 3 nW, E_{Laser} = 1.494 eV].

7.11. Leakage currents

With decreasing trap gate voltage we observe an unexpected kink in the slope of the quantum-confined Stark effect (see Fig. 7.3(c)). Therefore, the current flow from the trap gate to the back gate is measured to exclude leakage currents as the origin (Fig. 7.12). However, leakage currents entering the trap gate are negligibly small in the corresponding voltage regime where the PL is emitted. The absolute value of the current has an unknown constant offset of only a few pA. Thus, it is reasonable to assume that the externally applied voltages fully reflect the potentials applied at the gates in the relevant range of trap gate voltages. The kink in the slope of the quantum-confined Stark effect is expected to be a consequence of the narrowing of the quantum dot potential with increasing trap depth. In turn, the PL line of both

a 1 IX and a 2 IX are detected. Only for a trap gate voltage smaller than 0.06 V, a significant current starts to flow through the diode structure (Fig. 7.12).

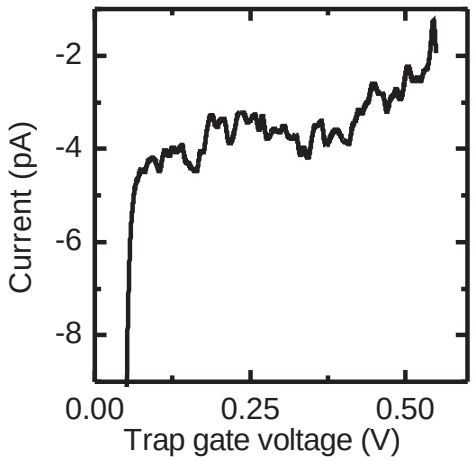

Figure 7.12.: **The current flow on the trap gate.** The current flow from the trap gate to the back gate is plotted versus trap gate voltage [$V_{\mathrm{G}} = 0.65\,\mathrm{V}$, $T_{\mathrm{Lattice}} = 244\,\mathrm{mK}$, $P_{\mathrm{Laser}} = 2.8\,\mathrm{nW}$, $E_{\mathrm{Laser}} = 1.494\,\mathrm{eV}$]

7.12. Conclusion

In conclusion, we realized individual optically active, gate-defined and voltage-controlled quantum traps for spatially indirect excitons in which a tuneable potential causes excitonic confinement in the DQW-plane. The population of such a QD can be tuned from a single exciton to a multi exciton state of above 100 IXs. With our device we introduce a gate-defined platform for creating and controlling optically active quantum dots with possible applications in fundamental quantum physics and quantum computing. This provides the possibility of lithographically defined coupled quantum dot arrays with voltage-controlled optical properties and tuneable in-plane coupling.

8. Quantum Hall effects of dipolar Mahan excitons

We explore the photoluminescence of spatially indirect, dipolar Mahan excitons in a gated double quantum well diode containing a mesoscopic electrostatic trap for neutral dipolar excitons at low temperatures down to 250 mK and in quantizing magnetic fields. Mahan excitons in the surrounding of the trap, consisting of individual holes interacting with a degenerate two-dimensional electron system confined in one of the quantum wells, exhibit strong quantum Hall effects at both integer and fractional filling factors of $\nu = \frac{2}{3}, \frac{3}{5}$, and $\frac{1}{2}$. Interactions across the trap perimeter are found to influence the energy of the confined neutral dipolar excitons by the presence of the quantum Hall effects in the two-dimensional electron system surrounding the trap.

8.1. Introduction

Interband optical excitations in solids containing degenerate electron systems provide a probe for many body interactions as reflected for example in the so-called Mahan exciton observed in degenerate semiconductors [Mahan 1967]. There, many body interactions between an exciton and remaining free electrons in the Fermi sea cause a so-called Fermi edge singularity of the optical absorption or emission, similar to singularities observed in the X-ray photoemission spectra of metals [Citrin et al. 1977]. Mahan excitons have been studied extensively in doped quantum wells containing a two-dimensional electron system (2DES) [Skolnick et al. 1987] and were found to also exhibit both integer [Klitzing et al. 1980] and fractional [Tsui et al. 1982] Quantum Hall Effects (QHE) in quantizing magnetic field [Turberfield et al. 1990; Goldberg et al. 1990; Yusa et al. 2001; Byszewski et al. 2006]. Coupled double quantum wells (CDQW), exhibiting long-living spatially indirect excitons, are of particular interest for the study of many body interactions between dipolar excitons, in part to explore potential Bose-Einstein condensation of excitons [Yang et al. 2006; Timofeev et al. 2007; Snoke 2011] predicted several decades ago [Blatt et al. 1962] but also to study the role of the strong dipolar interactions between excitons [Vögele et al. 2009a; Rapaport et al. 2005; Schinner et al. 2011b; Schinner et al. 2011a]. A related CDQW system, composed of two adjacent 2DES, are the bilayer

quantum Hall systems in which excitonic quasi-particles are formed in the ground state around half-filling of Landau levels (LLs) and investigated via magnetotransport experiments [Finck et al. 2011; Yoon et al. 2010].

Here we report on luminescence studies of excitons in a CDQW, consisting of an individual hole in one QW and a voltage-controlled 2DES in the other QW. Such type of dipolar quasi-particles we introduce as Mahan-like indirect excitons (MIX). In the presence of a quantizing magnetic field we find such MIX to exhibit both strong integer and fractional QHE. Furthermore, at the perimeter of an electrostatically created circular excitonic trap we find the QHE of the MIX located outside the trap perimeter to influence the energies of neutral dipolar excitons confined within the trap, thus reflecting non-local interactions across the trap perimeter. Our studies enable new insights into complex many body interactions in systems with restricted dimensionalities.

Dipolar excitons are spatially indirect excitons (IX) [Lozovik et al. 1976], i. e. bound pairs consisting of an electron and a hole, spatially separated in two adjacent CDQW [Rapaport et al. 2005; Butov et al. 1995; Vörös et al. 2005; Stern et al. 2008a]. In the absence of excess carriers neutral dipolar IX in a magnetic field B applied perpendicularly to the plane of the quantum wells exhibit a diamagnetic energy shift of $\Delta E_{\mathrm{dia}} \sim \frac{r_{\mathrm{e}}^2}{\mu} B^2$ with r_{e} the effective Bohr radius and μ the reduced mass of the excitons [Lozovik et al. 2002a; Bugajski et al. 1986]. A qualitatively different behavior is observed when the CDQW contains excess carriers [Kowalik-Seidl et al. 2011] or an electron-hole plasma of density above the Mott transition [Stern et al. 2008a]. In this case LL features increasing in energy in proportion to the magnetic field are observed, reflecting free carrier behavior.

8.2. Voltage-controlled 2DES exciton coupling

The CDQW device studied here is a diode structure which can be voltage tuned via the quantum confined Stark effect (QCSE). It contains two 7 nm thick $\mathrm{In}_x\mathrm{Ga}_{1-x}\mathrm{As}$ QWs ($x = 0.11$) separated by a 10 nm thick GaAs tunnel barrier. To achieve field-effect tunability the CDQW is embedded between a degenerately n-doped GaAs back contact and 6 nm thick semi-transparent titanium top gates [for further details see [Schinner et al. 2011a]]. The QCSE tunes the dipolar IX energy $\Delta E_{\mathrm{IX}} = -p^{\mathrm{IX}} F$ where $p^{\mathrm{IX}} = e d_{\mathrm{z}}^{\mathrm{IX}}$ is the IX dipole moment and $d_{\mathrm{z}}^{\mathrm{IX}}$ the electron-hole separation. $F = \frac{1}{l_0}(V_{\mathrm{FB}} - V)$ is the electric field perpendicular to the QW-plane where V is the applied gate voltage, V_{FB} is the flat-band gate voltage at which the built-in electric field is compensated, and l_0 denotes the distance between the gate electrode and the back contact. The QCSE allows the tuning of the electron states in the CDQW relative to the pinned Fermi energy of the back contact. As can be seen in Fig. 8.1(a), in the high field case, the quantum well QW_1 is occupied only by neutral

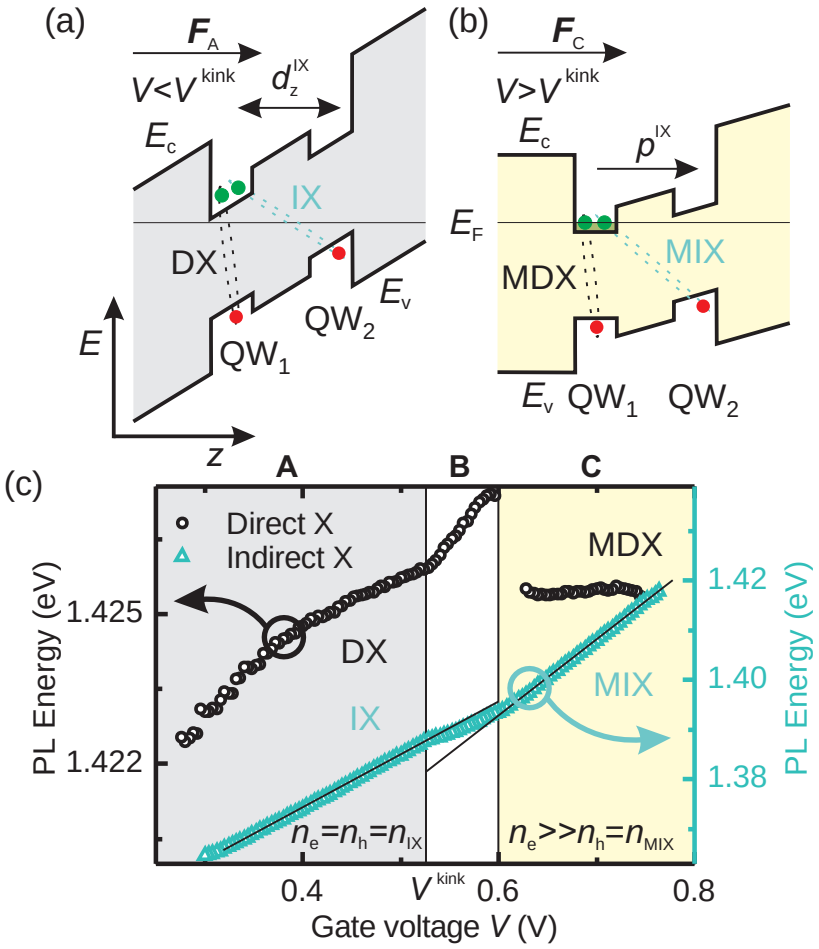

Figure 8.1.: (a) Schematic of the CDQW band gap within a field-effect device for a high electric field $\mathbf{F}_\mathrm{A}$ ($V < V^\mathrm{kink}$). (b) Sketch for the case of low electric field $\mathbf{F}_\mathrm{C}$ where QW_1 contains a degenerate electron gas. E_c and E_v denote the conduction and valence band edge, respectively. (c) Energy of the PL maximum of direct excitons (black circles on the left axis) and indirect excitons (blue triangles on the right axis) as a function of the gate voltage applied between the back contact and a large unstructured surface top gate. [$T_\mathrm{Lattice} = 4\,\mathrm{K}$, $E_\mathrm{Laser} = 1.494\,\mathrm{eV}$, $P_\mathrm{Laser} = 300\,\mathrm{nW}$].

direct (DX). Both, DX and IX interact predominantly via dipolar interactions. In the low field case, excess electrons occupy one of the quantum wells (QW_1) and the CDQW is populated with Mahan-like direct (MDX) and indirect excitons as illustrated in Fig. 8.1(b).

Employing a versatile confocal microscope with two objectives embedded in a ^{3}He refrigerator with a base temperature below 250 mK we study the photoluminescence (PL) from the InGaAs CDQW in Faraday geometry [Schinner et al. 2011b]. With the focus of the exciting laser at energy of 1.494 eV positioned on a macroscopic gate area and collecting PL with the second objective from this focus we measure PL spectra as a function of gate voltage and observe at 4 K the center energies shown in Fig. 8.1(c). At gate voltages $V < V^{\mathrm{kink}}$ (Fig. 8.1(a) and region A in Fig. 8.1(c)), only neutral excitons occupy the CDQW and the IX exhibit a linear QCSE with slope 0.105 eV/V corresponding to $d_{\mathrm{z}}^{\mathrm{IX}} = 15$ nm. Here the QCSE of the DX emitted from QW_1 is quadratic since the electron-hole separation of the DX increases with increasing Stark field, i. e. decreasing gate voltage [open circles in Fig. 8.1(c), for $V < V^{\mathrm{kink}}$]. Note that the DX luminescence is dominated by excitons in QW_1 since optically excited electrons in QW_2 tunnel efficiently into QW_1. For $V > V^{\mathrm{kink}}$ [region B in Fig. 8.1(c)] QW_1 is successively filled with electrons once the QW_1 ground state drops below the Fermi energy of the back contact. At $V > V^{\mathrm{kink}}$ excess electrons can be injected into QW_1 via the Ohmic contact region from the heterostructure surface to the back contact that penetrates both QWs. In addition, the effective Stark field acting in QW_1 decreases faster with increasing gate voltage as reflected by the increased slope of the DX PL energy. At the transition of region B to region C the QCSE in QW_1 becomes fully suppressed and at higher gate voltage, QW_1 acts effectively as the back contact. This causes an increased slope of the QCSE acting on the IX for $V > 0.6$ V, reflecting the reduced distance between gate and the new back contact. Simultaneously, a 2DES is formed in QW_1 and both excitons now become Mahan-like MDX and MIX. In region C the density of the 2DES is $n_{\mathrm{e}} = 1.06 \times 10^{11} \frac{1}{\mathrm{cm}^2}$ as further discussed below and provided by the donors of the originally, epitaxially doped GaAs back contact. For our experimental conditions n_{e} is independent of the laser power and large compared to the exciton density of $n_{\mathrm{MIX}} \lesssim 3 \times 10^{10} \frac{1}{\mathrm{cm}^2}$. Note that the MDX energy is lowered with respect to the DX one by renormalization effects caused by the presence of the 2DES.

To study the non-local interaction between charged and neutral areas of our heterostructure diode, the trap displayed in Fig. 8.2 is used. The trapping configuration contains two gates that can be independently biased, namely a guard gate (biased with V_{G}) defining a tunable surface potential and a trap gate usually biased at voltages $V_{\mathrm{T}} < V_{\mathrm{G}} < V_{\mathrm{FB}}$, in order to form an attractive trap for neutral IX while acting repulsively for excess electrons [Schinner et al. 2011a]. The trap gate has a diameter of 4 μm and is separated for insulation from the guard gate by a 100 nm narrow ungated region. Such traps are required to study two-dimensional bosonic ensembles of neutral IX at higher densities and thermalized to low temperatures of

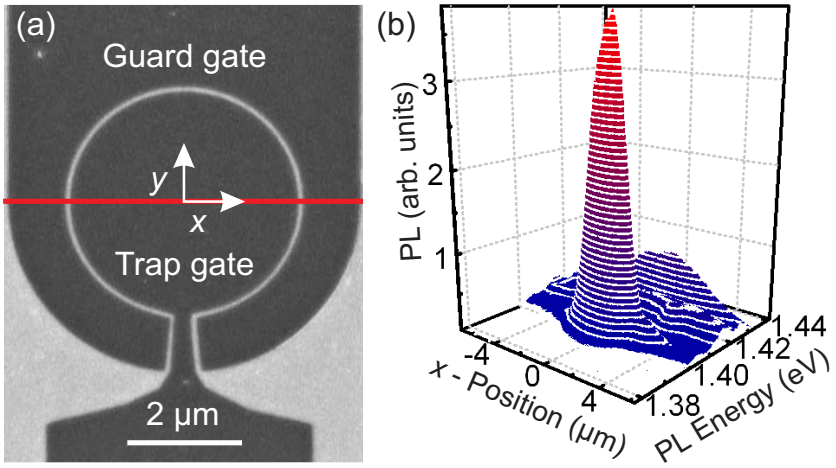

Figure 8.2.: (a) The scanning electron microscope (SEM) image of a circular trap consisting of a central trap gate, with a diameter of $d_{\mathrm{trap}} = 4\,\mu$m, which is surrounded by a guard gate. (b) Pseudo-3D picture of the PL intensity energetically and spatially resolved. The cut is taken along the x-direction through the middle of the trap as indicated by the red line in the SEM image (a). The exciton generation by a focused pump laser occurs below the guard gate at a distance $y_{\mathrm{Laser}} = 5\,\mu$m from of the trap center. [$V_{\mathrm{G}} = 0.60\,\mathrm{V}$, $V_{\mathrm{T}} = 0.35\,\mathrm{V}$, $T_{\mathrm{Lattice}} = 4\,\mathrm{K}$, $E_{\mathrm{Laser}} = 1.959\,\mathrm{eV}$, $P_{\mathrm{Laser}} = 10\,\mu\mathrm{W}$].

about 1 K or below, at which the thermal de Broglie wavelength of IX exceeds the interexcitonic spacing, and they are utilized to search for coherent excitonic phases at low temperatures [Yang et al. 2006; Timofeev et al. 2007; Snoke 2011]. Here we employ such a trap to study Mahan-like MDX and MIX close to the edge of a 2DES in quantizing magnetic field causing integer and fractional QHE. Quite unexpectedly, the neutral IX confined in the trap are found to exhibit features caused by the QHE in their surrounding, in addition to the expected diamagnetic energy shifts.

From now on the upper objective of our confocal microscope on top of the sample serves to generate electron-hole pairs with laser radiation focused at a distance of $y = 5\,\mu$m from the trap center. The second objective below the sample is used to collect the PL light in transmission. The pseudo-3D picture in Fig. 8.2(b) displays the measured PL intensity as a function of the PL energy along the x-direction in a cut through the middle of the trap [indicated by red line in Fig. 8.2(a)]. As reflected by the strong PL signal the trap provides a perfect spatial confinement for the IX [Fig. 8.2(b)] [Schinner et al. 2011a].

8.3. Mahan excitons in a quantizing magnetic field

In the following, we discuss the excitonic PL for the situation where the trap only contains neutral excitons ($V_\mathrm{T} < V_\mathrm{trap}^\mathrm{kink} < V_\mathrm{G}$, with $V_\mathrm{trap}^\mathrm{kink} = 0.40\,\mathrm{V}$ for the trap sample [Fig. 8.2 and below]). The trap is surrounded by a 2DES, supporting MDX and MIX under the guard gate (V_G biased in region C). Figure 8.3(a) sketches the corresponding energy landscape in the QW-plane in a quantizing magnetic field applied perpendicular to it [Chklovskii et al. 1992]. The electron states e_1^QW1 in QW_1 and hole states hh_1^QW2 in QW_2 form dipolar excitons after excitation of MDX in the laser focus. With increasing B both hole and electron states become quantized into LLs and excitonic transitions under the guard gate increase by $\Delta E(B) \simeq (n_\mathrm{LL} + \frac{1}{2})\hbar\omega_\mathrm{c}$, where $\omega_\mathrm{c} = \frac{eB}{\mu}$ is the cyclotron frequency with μ the reduced excitonic mass. With increasing magnetic field more and more LLs in the 2DES become depopulated. The

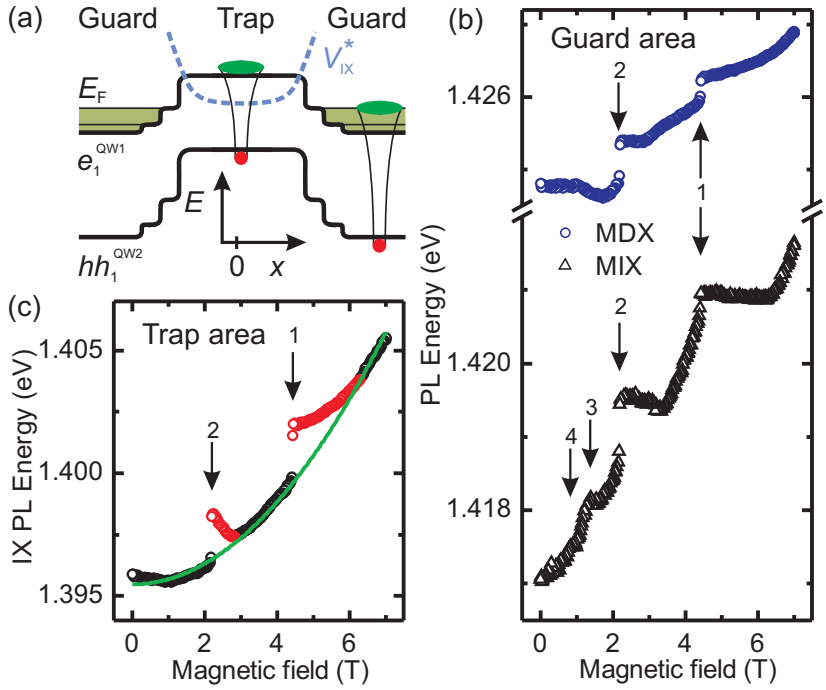

Figure 8.3.: (a) Ground state energies of electrons in QW_1 (e_1^QW1) and heavy holes in QW_2 (hh_1^QW2) versus x-position across the trap. The trap area is surrounded by a Landau quantized 2DES and the IX trapping potential V_IX^* is shown. (b) Energy of the PL maximum of direct MDX and indirect MIX versus B (arrows mark filling factors). (c) Diamagnetic shift of trapped IX. For the quadratic fit only the black data points are used. [$V_\mathrm{G} = 0.60\,\mathrm{V}$, $V_\mathrm{T} = 0.05\,\mathrm{V}$, $T_\mathrm{Lattice} = 250\,\mathrm{mK}$, $E_\mathrm{Laser} = 1.959\,\mathrm{eV}$, $P_\mathrm{Laser} = 9\,\mu\mathrm{W}$].

energy evolution of MDXs under the guard gate exhibits discontinuities associated with integer filling factors of LLs [Fig. 8.3(b)]. These direct excitons exist only in the vicinity of the exciting laser focus because of their short lifetime [Schinner et al. 2011a]. The MIXs under the guard gate surrounding the trap [Figs. 8.2(a), 8.3(a)] show energy plateaus of the PL maximum [Fig. 8.3(b)] at the same filling factors as the MDXs (marked in Figs. 8.3(b) 8.3(c) by arrows) and below, whenever a LL gets depopulated. In the PL indications are found which can be associated with higher LLs. The excitonic character of the MIX and MDX is completely different. The latter exists in the QW_1 containing the 2DES where Coulomb interactions are more important. In the case of MIX the hole is localized in QW_2, spatially separated from the 2DES, and the observed energy shift $\Delta E(B)$ fits very well to the one of the lowest LL ($n_{\mathrm{LL}} = 0$) of $\frac{1}{2}\hbar\omega_c$. A completely different picture is observed in the trap containing an ensemble of neutral IX, which shows a diamagnetic shift [Fig. 8.3(c)] from which an effective Bohr radius of $r_{\mathrm{e}} \approx 16\,\mathrm{nm}$ is extracted. In addition, signatures of the QHE modulate the parabolic diamagnetic shift. The trap gate is surrounded by the quantized edge states of the LL in the 2DES and their population modulates both, the potential at the trap perimeter [Fig. 8.3(a)] and the feeding of the trap with MIXs. Entering the trap area a MIX becomes a neutral indirect exciton. This conversion and hence the filling of the trap works best in the case of a depopulated LL. The observed blue shift of the IX PL energy in the trap reflects the increased IX population. Since all IX dipoles are aligned perpendicular to the QW-plane, the effective electric field, seen by an individual dipolar IX, is the sum of the externally applied electric field and the depolarizing dipolar field of all other IX in the vicinity. With increasing exciton density the effective electric field decreases and causes a blue shift ΔE, which in simplest approximation is proportional to the exciton density [Schinner et al. 2011b].

The density of the 2DES in the guard area for $0.5\,\mathrm{V} < V_{\mathrm{G}} < 0.8\,\mathrm{V}$ is independent of the guard gate voltage and the irradiated laser power. Both parameters are varied for each trace of Fig. 8.4(a), but still the plateaus are observed at the same magnetic fields. From the $1/B$ periodicity a constant electron density of $n_{\mathrm{e}} = 1.06 \times 10^{11} \frac{1}{\mathrm{cm}^2}$ is extracted, corresponding to a Fermi energy of $E_{\mathrm{F}} = 3.8\,\mathrm{meV}$ in QW_1. The energetic shift of the two traces in Fig. 8.4(a) relative to each other is caused by the QCSE. In this regime the QW_1 serves as back contact charged with electrons from the back contact. Only a finite number of electrons from the back contact is able to enter the QW_1 before a "charge equilibrium" arises.

At high magnetic fields extra kinks and plateaus of $\frac{2}{3}$, $\frac{3}{5}$ and $\frac{1}{2}$ fractional states appear in the MIX PL in addition to the integer QHE plateaus, see Fig. 8.4(a). These fractional states reflect Mahan like dipolar excitons which involve composite fermions in QW_1 interacting with individual holes in QW_2. This indicates that the $In_{0.11}Ga_{0.89}As$ CDQW device exhibit a very high electron and likely also exciton mobility. In Fig. 8.4(b) the $\frac{2}{3}$ fractional state is reflected in an energetic jump of the MDX PL at $T_{\mathrm{Lattice}} = 0.25\,\mathrm{K}$. With increasing temperature fractional states

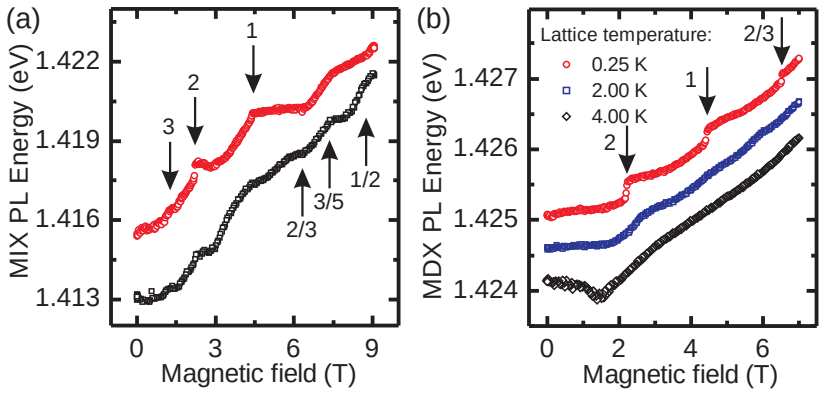

Figure 8.4.: (a) Energy of the PL maximum of MIX influenced by FQHE at T_{Lattice} = 250 mK for two configurations [red circles: $V_{\mathrm{G}} = 0.60\,\mathrm{V}$, $V_{\mathrm{T}} = 0.10\,\mathrm{V}$, $E_{\mathrm{Laser}} = 1.959\,\mathrm{eV}$, $P_{\mathrm{Laser}} = 9\,\mu\mathrm{W}$, black squares: $V_{\mathrm{G}} = 0.50\,\mathrm{V}$, $V_{\mathrm{T}} = 0.20\,\mathrm{V}$, $E_{\mathrm{Laser}} = 1.959\,\mathrm{eV}$, $P_{\mathrm{Laser}} = 14\,\mu\mathrm{W}$]. (b) Temperature dependence of the energy of the PL maximum of MDX as a function of B. The $T_{\mathrm{Lattice}} = 2\,\mathrm{K}$ and 4 K traces have an offset of -0.5 meV and -1 meV respectively [red circles: $T_{\mathrm{Lattice}} = 250\,\mathrm{mK}$, blue squares: $T_{\mathrm{Lattice}} = 2\,\mathrm{K}$, black diamonds: $T_{\mathrm{Lattice}} = 4\,\mathrm{K}$, $V_{\mathrm{G}} = 0.60\,\mathrm{V}$, $V_{\mathrm{T}} = 0.10\,\mathrm{V}$, $E_{\mathrm{Laser}} = 1.959\,\mathrm{eV}$, $P_{\mathrm{Laser}} = 9\,\mu\mathrm{W}$].

disappear first as expected, and at $T_{\mathrm{Lattice}} = 2\,\mathrm{K}$ only the integer QHE is still weakly visible. At $T_{\mathrm{Lattice}} = 4\,\mathrm{K}$ the signatures of the QHE are no longer observed.

8.4. Conclusion

In conclusion, magnetophotoluminescence spectroscopy on an exciton trapping device reveals the formation of Mahan-like excitons and their quantum Hall effect at sub-Kelvin temperatures. Although the excitons in the trap are neutral, their emission reflects the QHE nature of the surrounding quantum fluid, mediated by long range interactions across the trap perimeter. At integer filling factors, whenever a LL is depopulated we observe a sudden blue shift of the luminescence energy, reflecting an increased filling of the trap with neutral excitons. We wish to point out that the dipolar Mahan exciton is an ideal model system to investigate Mahan excitons with reduced Coulomb interaction.

9. Outlook

The presented experiments have demonstrated full control of the in-plane exciton dynamics via voltage controlled electrostatic potential landscapes for excitons. This outcome has been achieved due to the newly introduced exciton trap structures in combination with the modified heterostructure as well as the novel introduced detection scheme. The lasting success of the quantum trap introduced in Chapter 7 stimulates a series of further experiments. The gate defined quantum dots can straightforwardly be extended to coupled double dots [Holleitner et al. 2002] or to arrays of quantum traps. Additionally, it is possible to introduce the control of the filling of the quantum dots via gate electrodes and the combination of exciton flow control in excitonic integrated circuits [High et al. 2008] with gate defined quantum dots. Another interesting experiment is to perform resonant transmission experiments on the new quantum dots, up to now measured only on two-dimensional excitons and self-assembled quantum dots [Latta et al. 2011]. A final very interesting experiment is to investigate the intensity correlations $g^2(\tau)$ as a function of the exciton density confined in the quantum trap. Here it should be possible to observe the disappearance of the photon antibunching and a transition to the intensity correlations of a large excitonic ensemble.

By the creation of the quantum dot a dimensional crossover from the two-dimensional laterally unconfined exciton system to a zero-dimensional quantum trap has been established. Thereby the one-dimensional quantum point contact [van Wees et al. 1988; Wharam et al. 1988] is skipped. A potential realization of an excitonic quan-

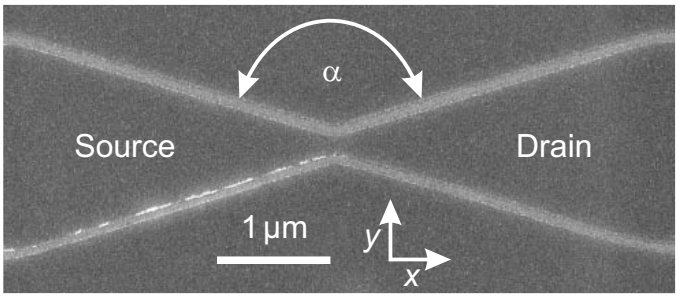

Figure 9.1.: **Excitonic quantum point contact.** A scanning electron microscope picture of a possible excitonic quantum point contact is shown. It is expected that the exciton flow from the left to right side is quantized.

tum point contact is shown in Fig. 9.1. Here the source and drain gates are connected, which allows its use as a resistive gate [Gärtner et al. 2006]. But one can imagine gate layouts with a split source and drain gate as well as a smaller angular α. This narrow constriction can additionally be used as a test leak for a potential proof of a superfluid exciton quantum phase [Lozovik et al. 1975].

In the case of large trapped and thermalized excitonic ensembles it would be instructive to measure the first order temporal coherence $g^1(\tau)$ as well as the first order spatial coherence $g^1(r_1, r_2)$ as a function of the trapped exciton density and the exciton ensemble temperature. The spatial correlation mapping could manifest a long-range order and phase coherence due to the massive occupation of a macroscopic bosonic ground state like in atomic Bose-Einstein condensation [Andrews et al. 1997; Bloch et al. 2000].

A. Publications

Chronologically sorted:

- *Phonon-mediated nonequilibrium interaction between nanoscale devices*
  G.J. Schinner, H.P. Tranitz, W. Wegscheider, J.P. Kotthaus, and S. Ludwig
  Phys. Rev. Lett. **102**, 186801 (2009)

- *Electron-avalanche amplifier based on the electronic Venturi effect*
  D. Taubert, **G.J. Schinner**, H.P. Tranitz, W. Wegscheider, C. Tomaras, S. Kehrein, and S. Ludwig
  Phys. Rev. B **82**, 161416 (2010)

- *Electrostatically trapping indirect excitons in coupled $In_xGa_{1-x}As$ quantum wells*
  G.J. Schinner, E. Schubert, M.P. Stallhofer, J.P. Kotthaus, D. Schuh, A.K. Rai, D. Reuter, A.D. Wieck, A.O. Govorov, and J.P. Kotthaus
  Phys. Rev. B **83**, 165308 (2011)

- *An electron jet pump: The Venturi effect of a Fermi liquid*
  D. Taubert, **G.J. Schinner**, C. Tomaras, H.P. Tranitz, W. Wegscheider, and S. Ludwig
  Journal of Applied Physics **109**, 102412 (2011)

- *Relaxation of hot electrons in a degenerate two-dimensional electron system: Transition to one-dimensional scattering*
  D. Taubert, C. Tomaras, **G.J. Schinner**, H.P. Tranitz, W. Wegscheider, S. Kehrein, and S. Ludwig
  Phys. Rev. B **83**, 235404 (2011)

- *Many-body correlations of electrostatically trapped dipolar excitons*
  G.J. Schinner, J. Repp, E. Schubert, A.K. Rai, D. Reuter, A.D. Wieck, A.O. Govorov, A.W. Holleitner, and J.P. Kotthaus
  ArXiv 1111.7175 (2011), under review at *Phys. Rev. Lett.*

- *Tunable photoemission from an excitonic antitrap*
  K. Kowalik-Seidl, X. Vögele, B. Rimpfl, **G.J. Schinner**, D. Schuh, W. Wegscheider, A.W. Holleitner, and J.P. Kotthaus
  Nano Letters **12** 326 (2012)

- *Single exciton control in gate-defined quantum traps*
  G.J. Schinner, J. Repp, E. Schubert, A.K. Rai, D. Reuter, A.D. Wieck, A.O. Govorov, A.W. Holleitner, and J.P. Kotthaus
  under review at *Phys. Rev. Lett.*
- *Quantum Hall signatures of dipolar Mahan excitons*
  G.J. Schinner, J. Repp, K. Kowalik-Seidl, E. Schubert, M.P. Stallhofer, A.K. Rai, D. Reuter, A.D. Wieck, A.O. Govorov, A.W. Holleitner, and J.P. Kotthaus
  under review at *Phys. Rev. Lett.*

B. Samples

B.1. Heterostructure

Layer	**Thickness and material**
capping layer	5 nm GaAs
blocking barrier	30 nm $Al_{0.41}Ga_{0.59}As$ in wafer A or 50 nm superlattice GaAs/AlAs in wafer B
double QW	5 nm GaAs
	7 nm $In_{0.11}Ga_{0.89}As$
	10 nm GaAs
	7 nm $In_{0.11}Ga_{0.89}As$
	5 nm GaAs
blocking barrier	30 nm $Al_{0.41}Ga_{0.59}As$ in wafer A or 50 nm superlattice GaAs/AlAs in wafer B
back contact	10 nm Si:GaAs in wafer A or 25 nm Si:GaAs in wafer B
buffer layer	500 nm GaAs
	120 nm superlattice GaAs/AlAs
	50 nm GaAs
substrate	GaAs (100)

B.2. Parameters of sample fabrication

Cleaning the sample

Step	Parameter
remove protective lacquer	60 min in warm acetone wipe with lens cleaning tissues
cleaning	in warm acetone

Ohmic contacts

Step	Parameter
spin-coating	Shipley Microposit 1813 photoresist
	3 s 800 min^{-1}
	30 s 4500 min^{-1}
	3 s 8000 min^{-1}
bake	100 s 115 °C
exposure	41 s Hg-light
develop	41 s developer ($\frac{\mathrm{Microposit351developer}}{\mathrm{H_2O}} = \frac{1}{3}$)
	20 s H_2O 1
	20 s H_2O 2
oxygen plasma	20 s 200 W 1 Torr O_2
evaporate	600 Å AuGe
	100 Å Ni
	600 Å AuGe
lift-off	30 min in warm acetone inclusive acetone blow
annealing	5 min 110 °C (remove residues)
	4 min 360 °C (melt)
	1 min 40 s 420 °C (alloy)

Coarse gold gate structures

Step	Parameter
spin-coating	Shipley Microposit 1813 photoresist
	1 s 800 min^{-1}
	30 s 6000 min^{-1}
	2 s 8000 min^{-1}
bake	90 s 115 °C
exposure	28 s Hg-light
develop	28 s developer ($\frac{\mathrm{Microposit351developer}}{\mathrm{H_2O}} = \frac{1}{3}$)
	15 s H_2O 1
	15 s H_2O 2
oxygen plasma	20 s 200 W
evaporate	50 Å Ti
	900 Å Au
lift-off	60 min in warm acetone inclusive acetone blow

Electron-beam lithography of fine gold gates

Step	Parameter
spin-coating	PMMA-500k (Polymethylmethacrylat)
	1 s 800 min^{-1}
	30 s 5000 min^{-1}
bake	100 s 170 °C
electron-beam lithography	acceleration voltage: 5 kV
	aperture: 10 μm
	$T = 21.7$ °C
	average dose: 45 $\frac{\mu\mathrm{C}}{\mathrm{cm}^2}$
develop	50 s PMMA-developer ($\frac{\mathrm{MIBK}}{\mathrm{IPA}} = \frac{\mathrm{Methylisobutylketon}}{\mathrm{Isopropanol}} = \frac{1}{3}$)
	50 s Isopropanol
evaporate	30 Å Ti
	300 Å Au
lift-off	60 min in warm acetone inclusive acetone blow

Electron-beam lithography of fine titanium gates

Step	Parameter
spin-coating	PMMA-500k (Polymethylmethacrylat)
	1 s 800 min^{-1}
	30 s 5000 min^{-1}
bake	100 s 170 °C
electron-beam lithography	acceleration voltage: 5 kV
	aperture: 10 μm
	$T = 21.3\,°\mathrm{C}$
	average dose: 44.5 $\frac{\mu\mathrm{C}}{\mathrm{cm}^2}$
develop	50 s PMMA-developer ($\frac{\mathrm{MIBK}}{\mathrm{IPA}} = \frac{\mathrm{Methylisobutylketon}}{\mathrm{Isopropanol}} = \frac{1}{3}$)
	50 s Isopropanol
oxygen plasma	20 s 200 W
evaporate	60 Å Ti
lift-off	75 min in warm acetone inclusive acetone blow

B.3. Used clean room equipment

Equipment	Type
spin coater	WS400B-6NPP/LITE/IND, Co. Laurell (optical lithography)
	1001S - ST146, Co. Convac (SEM lithography)
scanning electron microscope	System 982, Co. Raith LEO
	Co. Raith e LINE
mask aligner	MBJB3, Co. Karl Suss
microscope	BH-2 UMA, Co. Olympus
high vacuum coating plant	Co. BesTec
O_2 plasma	100-E Plasma System, Co. Technics Plasma GmbH
annealing–stove	Biorad, Co. Microscience Division
wedge bonder	MEI 1204W Hybrid Wedge Bonder, Co. Marpet Enterprises

Bibliography

[Alexandrou et al. 1990]
A. Alexandrou, J. A. Kash, E. E. Mendez, M. Zachau, J. M. Hong, T. Fukuzawa, and Y. Hase, "Electric-field effects on exciton lifetimes in symmetric coupled GaAs/$Al_{0.3}Ga_{0.7}$As double quantum wells", *Phys. Rev. B* **42**, 9225–9228 (1990).

[Allen et al. 1938]
J. F. Allen and H. Jones, "New Phenomena Connected with Heat Flow in Helium II", *Nature* **141**, 243–244 (1938).

[Alloing et al. 2011]
M. Alloing, A. Lematre, and F. Dubin, "Quantum signature blurred by disorder in indirect exciton gases", *EPL (Europhysics Letters)* **93**, 17007 (2011).

[Alloing et al. 2012a]
M. Alloing, A. Lemaitre, E. Galopin, and F. Dubin, "Non-linear dynamics and inner-ring photoluminescence pattern of indirect excitons", *ArXiv 1202.1985* (2012).

[Alloing et al. 2012b]
M. Alloing, A. Lemaitre, E. Galopin, and F. Dubin, "On-demand confinement of semiconductor excitons by all-optical control", *ArXiv 1202.3301* (2012).

[Anderson et al. 1995]
M. H. Anderson, J. R. Ensher, M. R. Matthews, C. E. Wieman, and E. A. Cornell, "Observation of Bose-Einstein Condensation in a Dilute Atomic Vapor", *Science* **269**, 198–201 (1995).

[Andrews et al. 1997]
M. R. Andrews, C. G. Townsend, H.-J. Miesner, D. S. Durfee, D. M. Kurn, and W. Ketterle, "Observation of Interference Between Two Bose Condensates", *Science* **275**, 637–641 (1997).

[Andrews et al. 1988]
S. R. Andrews, C. M. Murray, R. A. Davies, and T. M. Kerr, "Stark effect in strongly coupled quantum wells", *Phys. Rev. B* **37**, 8198–8204 (1988).

[Aoki 1979]
H Aoki, "Effect of coexistence of random potential and electron-electron interaction

in two-dimensional systems: Wigner glass", *Journal of Physics C: Solid State Physics* **12**, 633 (1979).

[Bagnato et al. 1991]
V. Bagnato and D. Kleppner, "Bose-Einstein condensation in low-dimensional traps", *Phys. Rev. A* **44**, 7439–7441 (1991).

[Balatsky et al. 2004]
A. V. Balatsky, Y. N. Joglekar, and P. B. Littlewood, "Dipolar Superfluidity in Electron-Hole Bilayer Systems", *Phys. Rev. Lett.* **93**, 266801 (2004).

[Balili et al. 2007]
R. Balili, V. Hartwell, D. Snoke, L. Pfeiffer, and K. West, "Bose-Einstein Condensation of Microcavity Polaritons in a Trap", *Science* **316**, 1007–1010 (2007).

[Bardeen et al. 1957a]
J. Bardeen, L. N. Cooper, and J. R. Schrieffer, "Microscopic Theory of Superconductivity", *Phys. Rev.* **106**, 162–164 (1957).

[Bardeen et al. 1957b]
J. Bardeen, L. N. Cooper, and J. R. Schrieffer, "Theory of Superconductivity", *Phys. Rev.* **108**, 1175–1204 (1957).

[Bastard et al. 1982]
G. Bastard, E. E. Mendez, L. L. Chang, and L. Esaki, "Exciton binding energy in quantum wells", *Phys. Rev. B* **26**, 1974–1979 (1982).

[Basu et al. 1992]
P. K. Basu and P. Ray, "Energy relaxation of hot two-dimensional excitons in a GaAs quantum well by exciton-phonon interaction", *Phys. Rev. B* **45**, 1907–1910 (1992).

[Bedanov et al. 1994]
V. M. Bedanov and F. M. Peeters, "Ordering and phase transitions of charged particles in a classical finite two-dimensional system", *Phys. Rev. B* **49**, 2667–2676 (1994).

[Berezinskiĭ 1971]
V. L. Berezinskiĭ, "Destruction of Long-range Order in One-dimensional and Two-dimensional Systems having a Continuous Symmetry Group I. Classical Systems", *Soviet Journal of Experimental and Theoretical Physics* **32**, 493 (1971).

[Berezinskiĭ 1972]
V. L. Berezinskiĭ, "Destruction of Long-range Order in One-dimensional and Two-dimensional Systems Possessing a Continuous Symmetry Group. II. Quantum Systems", *Soviet Journal of Experimental and Theoretical Physics* **34**, 610 (1972).

[Berman et al. 2007]
O. L. Berman, Y. E. Lozovik, D. W. Snoke, and R. D. Coalson, "Superfluidity of 'dirty' indirect magnetoexcitons in coupled quantum wells in high magnetic field", *Journal of Physics: Condensed Matter* **19**, 386219 (2007).

[Berman et al. 2008a]
O. L. Berman, Y. E. Lozovik, and G. Gumbs, "Bose-Einstein condensation and superfluidity of magnetoexcitons in bilayer graphene", *Phys. Rev. B* **77**, 155433 (2008).

[Berman et al. 2008b]
O. L. Berman, R. Y. Kezerashvili, and Y. E. Lozovik, "Collective properties of magnetobiexcitons in quantum wells and graphene superlattices", *Phys. Rev. B* **78**, 035135 (2008).

[Berman et al. 2008c]
O. L. Berman, Y. E. Lozovik, and D. W. Snoke, "Theory of Bose-Einstein condensation and superfluidity of two-dimensional polaritons in an in-plane harmonic potential", *Phys. Rev. B* **77**, 155317 (2008).

[Berman et al. 2012]
O. L. Berman, R. Y. Kezerashvili, and K. Ziegler, "Superfluidity of dipole excitons in the presence of band gaps in two-layer graphene", *Phys. Rev. B* **85**, 035418 (2012).

[Blatt et al. 1954]
J. M. Blatt and S. T. Butler, "Superfluidity of a Boson Gas", *Phys. Rev.* **96**, 1149–1150 (1954).

[Blatt et al. 1962]
J. M. Blatt, K. W. Böer, and W. Brandt, "Bose-Einstein Condensation of Excitons", *Phys. Rev.* **126**, 1691–1692 (1962).

[Blatt et al. 2008]
R. Blatt and D. Wineland, "Entangled states of trapped atomic ions", *Nature* **453**, 1008–1015 (2008).

[Bloch et al. 2000]
I. Bloch, T. W. Hänsch, and T. Esslinger, "Measurement of the spatial coherence of a trapped Bose gas at the phase transition", *Nature* **403**, 166–170 (2000).

[Blom et al. 1993]
P. W. M. Blom, P. J. van Hall, C. Smit, J. P. Cuypers, and J. H. Wolter, "Selective exciton formation in thin GaAs/$Al_xGa_{1-x}As$ quantum wells", *Phys. Rev. Lett.* **71**, 3878–3881 (1993).

[Bose 1924]
Bose, "Plancks Gesetz und Lichtquantenhypothese", *Zeitschrift für Physik* **26**, 178–181 (1924).

[Boyer de la Giroday et al. 2010]
A. Boyer de la Giroday, A. J. Bennett, M. A. Pooley, R. M. Stevenson, N. Sköld, R. B. Patel, I. Farrer, D. A. Ritchie, and A. J. Shields, "All-electrical coherent control of the exciton states in a single quantum dot", *Phys. Rev. B* **82**, 241301 (2010).

[Boyer de la Giroday et al. 2011]
A. Boyer de la Giroday, N. Sköld, R. M. Stevenson, I. Farrer, D. A. Ritchie, and A. J. Shields, "Exciton-Spin Memory with a Semiconductor Quantum Dot Molecule", *Phys. Rev. Lett.* **106**, 216802 (2011).

[Brunner et al. 1994]
K. Brunner, G. Abstreiter, G. Böhm, G. Tränkle, and G. Weimann, "Sharp-Line Photoluminescence and Two-Photon Absorption of Zero-Dimensional Biexcitons in a GaAs/AlGaAs Structure", *Phys. Rev. Lett.* **73**, 1138–1141 (1994).

[Bugajski et al. 1986]
M. Bugajski, W. Kuszko, and K. Reginski, "Diamagnetic shift of exciton energy levels in GaAs-$Ga_{1-x}Al_xAs$ quantum wells", *Solid State Communications* **60**, 669 –673 (1986).

[Burkard et al. 1999]
G. Burkard, D. Loss, and D. P. DiVincenzo, "Coupled quantum dots as quantum gates", *Phys. Rev. B* **59**, 2070–2078 (1999).

[Butov et al. 1994]
L. V. Butov, A. Zrenner, G. Abstreiter, G. Böhm, and G. Weimann, "Condensation of Indirect Excitons in Coupled AlAs/GaAs Quantum Wells", *Phys. Rev. Lett.* **73**, 304–307 (1994).

[Butov et al. 1995]
L. V. Butov, A. Zrenner, A. V. Abstreiter G. Petinova, and K. Eberl, "Direct and indirect magnetoexcitons in symmetric $In_xGa_{1-x}As$/GaAs coupled quantum wells", *Phys. Rev. B* **52**, 12153 –12157 (1995).

[Butov et al. 2001]
L. V. Butov, A. L. Ivanov, A. Imamoglu, P. B. Littlewood, A. A. Shashkin, V. T. Dolgopolov, K. L. Campman, and A. C. Gossard, "Stimulated Scattering of Indirect Excitons in Coupled Quantum Wells: Signature of a Degenerate Bose-Gas of Excitons", *Phys. Rev. Lett.* **86**, 5608–5611 (2001).

[Butov et al. 2002]
L. V. Butov, C. W. Lai, A. L. Ivanov, A. C. Gossard, and D. S. Chemla, "Towards Bose-Einstein condensation of excitons in potential traps", *Nature* **417**, 47 (2002).

[Byszewski et al. 2006]
M. Byszewski, B. Chwalisz, D. K. Maude, M. L. Sadowski, M. Potemski, T. Saku, Y. Hirayama, S. Studenikin, D. G. Austing, A. S. Sachrajda, and P. Hawrylak, "Optical probing of composite fermions in a two-dimensional electron gas", *Nature Physics* **2**, 239–243 (2006).

[Casella 1963]
R. C. Casella, "A Criterion for Exciton Binding in Dense Electron—Hole Systems—Application to Line Narrowing Observed in GaAs", *Journal of Applied Physics* **34**, 1703–1705 (1963).

[Charbonneau et al. 1988]
S. Charbonneau, M. L. W. Thewalt, E. S. Koteles, and B. Elman, "Transformation of spatially direct to spatially indirect excitons in coupled double quantum wells", *Phys. Rev. B* **38**, 6287–6290 (1988).

[Chen et al. 2006]
G. Chen, R. Rapaport, L. N. Pffeifer, K. West, P. M. Platzman, S. Simon, Z. Vörös, and D. Snoke, "Artificial trapping of a stable high-density dipolar exciton fluid", *Phys. Rev. B* **74**, 045309 (2006).

[Chen et al. 2005]
Q. Chen, J. Stajic, S. Tan, and K. Levin, "BCS BEC crossover: From high temperature superconductors to ultracold superfluids", *Phys. Rep.* **412**, 1–88 (2005).

[Chen et al. 1987]
Y. J. Chen, E. S. Koteles, B. S. Elman, and C. A. Armiento, "Effect of electric fields on excitons in a coupled double-quantum-well structure", *Phys. Rev. B* **36**, 4562–4565 (1987).

[Chklovskii et al. 1992]
D. B. Chklovskii, B. I. Shklovskii, and L. I. Glazman, "Electrostatics of edge channels", *Phys. Rev. B* **46**, 4026 and 15606 (1992).

[Christianen et al. 1998]
P. C. M. Christianen, F. Piazza, J. G. S. Lok, J. C. Maan, and W. van der Vleuten, "Magnetic trap for excitons", *Physica B: Condensed Matter* **249-251**, 624 –627 (1998).

[Citrin et al. 1977]
P. H. Citrin, G. K. Wertheim, and Y. Baer, "Many-body processes in x-ray photoe-

mission line shapes from Li, Na, Mg, and Al metals", *Phys. Rev. B* **16**, 4256–4282 (1977).

[Cladé et al. 2009]
P. Cladé, C. Ryu, A. Ramanathan, K. Helmerson, and W. D. Phillips, "Observation of a 2D Bose Gas: From Thermal to Quasicondensate to Superfluid", *Phys. Rev. Lett.* **102**, 170401 (2009).

[Dalfovo et al. 1999]
F. Dalfovo, S. Giorgini, L. P. Pitaevskii, and S. Stringari, "Theory of Bose-Einstein condensation in trapped gases", *Rev. Mod. Phys.* **71**, 463–512 (1999).

[Damen et al. 1990]
T. C. Damen, J. Shah, D. Y. Oberli, D. S. Chemla, J. E. Cunningham, and J. M. Kuo, "Dynamics of exciton formation and relaxation in GaAs quantum wells", *Phys. Rev. B* **42**, 7434–7438 (1990).

[Davis et al. 1995]
K. B. Davis, M. O. Mewes, M. R. Andrews, N. J. van Druten, D. S. Durfee, D. M. Kurn, and W. Ketterle, "Bose-Einstein Condensation in a Gas of Sodium Atoms", *Phys. Rev. Lett.* **75**, 3969–3973 (1995).

[De Broglie 1924]
L. de Broglie, "A tentative theory of light quanta", *Philos. Mag.* **47**, 446–458 (1924).

[Demokritov et al. 2006]
S. O. Demokritov, V. E. Demidov, O. Dzyapko, G. A. Melkov, A. A. Serga, B. Hillebrands, and A. N. Slavin, "Bose-Einstein condensation of quasi-equilibrium magnons at room temperature under pumping", *Nature* **443**, 430–433 (2006).

[Deng et al. 2010]
H. Deng, H. Haug, and Y. Yamamoto, "Exciton-polariton Bose-Einstein condensation", *Rev. Mod. Phys.* **82**, 1489–1537 (2010).

[Dingle et al. 1975]
R. Dingle, A. C. Gossard, and W. Wiegmann, "Direct Observation of Superlattice Formation in a Semiconductor Heterostructure", *Phys. Rev. Lett.* **34**, 1327–1330 (1975).

[Drexler et al. 1994]
H. Drexler, D. Leonard, W. Hansen, J. P. Kotthaus, and P. M. Petroff, "Spectroscopy of Quantum Levels in Charge-Tunable InGaAs Quantum Dots", *Phys. Rev. Lett.* **73**, 2252–2255 (1994).

[Duarte et al. 2008]
J. L. Duarte, L. C. Poças, E. Laureto, I. F. L. Dias, E. M. Lopes, S. A. Lourenço,

and J. C. Harmand, "Competition between confinement potential fluctuations and band-gap renormalization effects in InGaAs / InGaAlAs single and double quantum wells", *Phys. Rev. B* **77**, 165322 (2008).

[Eccleston et al. 1991]
R. Eccleston, R. Strobel, W. W. Rühle, J. Kuhl, B. F. Feuerbacher, and K. Ploog, "Exciton dynamics in a GaAs quantum well", *Phys. Rev. B* **44**, 1395–1398 (1991).

[Einstein 1924]
A. Einstein, "Quantentheorie der einatomigen idealen Gase", *Sitzungsber. K. Preuss. Akad. Wiss., Phys. Math. Kl* **261** (1924).

[Einstein 1925]
A. Einstein, "Quantentheorie des einatomigen idealen Gases. II", *Sitzungsber. K. Preuss. Akad. Wiss., Phys. Math. Kl* **3** (1925).

[Eisenstein et al. 2004]
J. P. Eisenstein and A. H. MacDonald, "Bose-Einstein condensation of excitons in bilayer electron systems", *Nature* **432**, 691–694 (2004).

[Feldmann et al. 1987]
J. Feldmann, G. Peter, E. O. Göbel, P. Dawson, K. Moore, C. Foxon, and R. J. Elliot, "Linewidth Dependence of Radiative Exciton Lifetimes in Quantum Wells", *Phys. Rev. Lett.* **59**, 2337 –2340 (1987).

[Fermi 1926]
E. Fermi, "Zur Quantelung des idealen einatomigen Gases", *Zeitschrift fur Physik* **36**, 902–912 (1926).

[Finck et al. 2010]
A. D. K. Finck, J. P. Eisenstein, L. N. Pfeiffer, and K. W. West, "Quantum Hall Exciton Condensation at Full Spin Polarization", *Phys. Rev. Lett.* **104**, 016801 (2010).

[Finck et al. 2011]
A. D. K. Finck, J. P. Eisenstein, L. N. Pfeiffer, and K. W. West, "Exciton Transport and Andreev Reflection in a Bilayer Quantum Hall System", *Phys. Rev. Lett.* **106**, 236807 (2011).

[Fortin et al. 1993]
E. Fortin, S. Fafard, and A. Mysyrowicz, "Exciton transport in Cu_2O: Evidence for excitonic superfluidity?", *Phys. Rev. Lett.* **70**, 3951–3954 (1993).

[Fukuzawa et al. 1990]
T. Fukuzawa, E. E. Mendez, and J. M. Hong, "Phase transition of an exciton system in GaAs coupled quantum wells", *Phys. Rev. Lett.* **64**, 3066–3069 (1990).

[Gärtner et al. 2006]
A. Gärtner, A. W. Holleitner, J. P. Kotthaus, and D. Schuh, "Drift mobility of long-living excitons in coupled GaAs quantum wells", *Applied Physics Letters* **89**, 052108 (2006).

[Gärtner et al. 2007]
A. Gärtner, L. Prechtel, D. Schuh, A. W. Holleitner, and J. P. Kotthaus, "Micropatterned electrostatic traps for indirect excitons in coupled GaAs quantum wells", *Phys. Rev. B* **76**, 085304 (2007).

[Gergel et al. 1968]
V. A. Gergel, R. F. Kazarinov, and R. A. Suri, "Optical properties of an exciton condensate in a semiconductor", *Soviet Physics JETP* **26**, 354 (1968).

[Giorgini et al. 2008]
S. Giorgini, L. P. Pitaevskii, and S. Stringari, "Theory of ultracold atomic Fermi gases", *Rev. Mod. Phys.* **80**, 1215–1274 (2008).

[Goldberg et al. 1990]
B. B. Goldberg, D. Heiman, A. Pinczuk, L. Pfeiffer, and K. West, "Optical investigations of the integer and fractional quantum Hall effects: Energy plateaus, intensity minima, and line splitting in band-gap emission", *Phys. Rev. Lett.* **65**, 641–644 (1990).

[Gorbunov et al. 2006]
A. V. Gorbunov and V. B. Timofeev, "Collective state in a Bose gas of interacting interwell excitons", *Soviet Journal of Experimental and Theoretical Physics Letters* **83**, 146–151 (2006).

[Govorov et al. 1998]
A. O. Govorov and W. Hansen, "Tunnel ionization of quantum-well magnetoexcitons localized in a lateral trap", *Phys. Rev. B* **58**, 12980–12985 (1998).

[Greiner et al. 2003]
M. Greiner, C. A. Regal, and D. S. Jin, "Emergence of a molecular Bose-Einstein condensate from a Fermi gas", *Nature* **426**, 537–540 (2003).

[Griffin 1999]
A. Griffin, "A Brief History of Our Understanding of BEC: From Bose to Beliaev", *eprint arXiv:cond-mat/9901123* (1999).

[Grosso et al. 2009]
G. Grosso, J. Graves, A. T. Hammack, A. A. High, L. V. Butov, M. Hanson, and A. C. Gossard, "Excitonic switches operating at around 100 K", *Nature Photonics* **3**, 577–580 (2009).

[Gulia et al. 1997]
M. Gulia, F. Rossi, E. Molinari, P. E. Selbmann, and P. Lugli, "Phonon-assisted exciton formation and relaxation in GaAs/$AlxGa1 - x$As quantum wells", *Phys. Rev. B* **55**, R16049–R16052 (1997).

[Hadzibabic et al. 2006]
Z. Hadzibabic, P. Krüger, M. Cheneau, B. Battelier, and J. Dalibard, "Berezinskii-Kosterlitz-Thouless crossover in a trapped atomic gas", *Nature* **441**, 1118–1121 (2006).

[Hakioglu et al. 2007]
T. Hakioglu and M. Sahin, "Excitonic Condensation under Spin-Orbit Coupling and BEC-BCS Crossover", *Phys. Rev. Lett.* **98**, 166405 (2007).

[Hammack et al. 2006a]
A. T. Hammack, N. A. Gippius, S. Yang, G. O. Andreev, L. V. Butov, M. Hanson, and A. C. Gossard, "Excitons in electrostatic traps", *Journal of Applied Physics* **99**, 066104 (2006).

[Hammack et al. 2006b]
A. T. Hammack, M. Griswold, L. V. Butov, L. E. Smallwood, A. L. Ivanov, and A. C. Gossard, "Trapping of Cold Excitons in Quantum Well Structures with Laser Light", *Phys. Rev. Lett.* **96**, 227402 (2006).

[Hammack et al. 2009]
A. T. Hammack, L. V. Butov, J. Wilkes, L. Mouchliadis, E. A. Muljarov, A. L. Ivanov, and A. C. Gossard, "Kinetics of the inner ring in the exciton emission pattern in coupled GaAs quantum wells", *Phys. Rev. B* **80**, 155331 (2009).

[Hanson et al. 2007]
R. Hanson, L. P. Kouwenhoven, J. R. Petta, S. Tarucha, and L. M. K. Vandersypen, "Spins in few-electron quantum dots", *Rev. Mod. Phys.* **79**, 1217–1265 (2007).

[Hawrylak 1991]
P. Hawrylak, "Optical properties of a two-dimensional electron gas: Evolution of spectra from excitons to Fermi-edge singularities", *Phys. Rev. B* **44**, 3821–3828 (1991).

[Hermelin et al. 2011]
S. Hermelin, S. Takada, M. Yamamoto, S. Tarucha, A. D. Wieck, L. Saminadayar, C. Bäuerle, and T. Meunier, "Electrons surfing on a sound wave as a platform for quantum optics with flying electrons", *Nature* **477**, 435–438 (2011).

[High et al. 2007]
A. A. High, A. T. Hammack, L. V. Butov, M. Hanson, and A. C. Gossard, "Exciton optoelectronic transistor", *Opt. Lett.* **32**, 2466–2468 (2007).

[High et al. 2008]
A. A. High, E. E. Novitskaya, L. V. Butov, M. Hanson, and A. C. Gossard, "Control of Exciton Fluxes in an Excitonic Integrated Circuit", *Science* **321**, 1157845 (2008).

[High et al. 2009a]
A. A. High, A. T. Hammack, L. V. Butov, L. Mouchliadis, A. Ivanov, M. Hanson, and A. C. Gossard, "Indirect Excitons in Elevated Traps", *Nano Letters* **9**, 2094–2098 (2009).

[High et al. 2009b]
A. A. High, A. K. Thomas, G. Grosso, M. Remeika, A. T. Hammack, A. D. Meyertholen, M. M. Fogler, L. V. Butov, M. Hanson, and A. C. Gossard, "Trapping Indirect Excitons in a GaAs Quantum-Well Structure with a Diamond-Shaped Electrostatic Trap", *Phys. Rev. Lett.* **103**, 087403 (2009).

[Högele et al. 2004]
A. Högele, S. Seidl, M. Kroner, K. Karrai, R. J. Warburton, B. D. Gerardot, and P. M. Petroff, "Voltage-Controlled Optics of a Quantum Dot", *Phys. Rev. Lett.* **93**, 217401 (2004).

[Högele et al. 2008]
A. Högele, S. Seidl, M. Kroner, K. Karrai, C. Schulhauser, O. Sqalli, J. Scrimgeour, and R. J. Warburton, "Fiber-based confocal microscope for cryogenic spectroscopy", *Review of Scientific Instruments* **79**, 023709 (2008).

[Hohenberg 1967]
P. C. Hohenberg, "Existence of Long-Range Order in One and Two Dimensions", *Phys. Rev.* **158**, 383 –386 (1967).

[Holland et al. 2001]
M. Holland, S. J. J. M. F. Kokkelmans, M. L. Chiofalo, and R. Walser, "Resonance Superfluidity in a Quantum Degenerate Fermi Gas", *Phys. Rev. Lett.* **87**, 120406 (2001).

[Holleitner et al. 2002]
A. W. Holleitner, R. H. Blick, A. K. Hüttel, K. Eberl, and J. P. Kotthaus, "Probing and Controlling the Bonds of an Artificial Molecule", *Science* **297**, 70–72 (2002).

[Hu et al. 2007]
Y. Hu, H. O. H. Churchill, D. J. Reilly, J. Xiang, C. M. Lieber, and C. M. Marcus, "A

Ge/Si heterostructure nanowire-based double quantum dot with integrated charge sensor", *Nature Nanotechnology* **2**, 622–625 (2007).

[Huber et al. 1998]
T. Huber, A. Zrenner, W. Wegscheider, and M. Bichler, "Electrostatic Exciton Traps", *Physica Status Solidi Applied Research* **166**, 5 (1998).

[Hulin et al. 1980]
D. Hulin, A. Mysyrowicz, and C. B. à la Guillaume, "Evidence for Bose-Einstein Statistics in an Exciton Gas", *Phys. Rev. Lett.* **45**, 1970–1973 (1980).

[Imamoglu et al. 1999]
A. Imamoglu, D. D. Awschalom, G. Burkard, D. P. DiVincenzo, D. Loss, M. Sherwin, and A. Small, "Quantum Information Processing Using Quantum Dot Spins and Cavity QED", *Phys. Rev. Lett.* **83**, 4204–4207 (1999).

[Ivanov 2002]
A. L. Ivanov, "Quantum diffusion of dipole-oriented indirect excitons in coupled quantum wells", *EPL (Europhysics Letters)* **59**, 586 (2002).

[Ivanov et al. 1997]
A. L. Ivanov, C. Ell, and H. Haug, "Phonon-assisted Boltzmann kinetics of a Bose gas: Generic solution for $T \leqslant T_c$", *Phys. Rev. E* **55**, 6363–6369 (1997).

[Ivanov et al. 1999]
A. L. Ivanov, P. B. Littlewood, and H. Haug, "Bose-Einstein statistics in thermalization and photoluminescence of quantum-well excitons", *Phys. Rev. B* **59**, 5032–5048 (1999).

[Ivanov et al. 2010]
A. L. Ivanov, E. A. Muljarov, L. Mouchliadis, and R. Zimmermann, "Comment on "Photoluminescence Ring Formation in Coupled Quantum Wells: Excitonic Versus Ambipolar Diffusion"", *Phys. Rev. Lett.* **104**, 179701 (2010).

[J. Fernandez-Rossier 1997]
C. T. J. Fernandez-Rossier, "Spin Degree of Freedom in Two Dimensional Exciton Condensates", *Phys. Rev. Lett.* **78**, 4809 –4812 (1997).

[Jochim et al. 2003]
S. Jochim, M. Bartenstein, A. Altmeyer, G. Hendl, S. Riedl, C. Chin, J. Hecker Denschlag, and R. Grimm, "Bose-Einstein Condensation of Molecules", *Science* **302**, 2101–2103 (2003).

[Kane et al. 1967]
J. W. Kane and L. P. Kadanoff, "Long-Range Order in Superfluid Helium", *Phys. Rev.* **155**, 80–83 (1967).

[Kapitza 1938]
P. Kapitza, "Viscosity of Liquid Helium below the λ-Point", *Nature* **141**, 74 (1938).

[Kash et al. 1991]
J. A. Kash, M. Zachau, E. E. Mendez, J. M. Hong, and T. Fukuzawa, "Fermi-Dirac distribution of excitons in coupled quantum wells", *Phys. Rev. Lett.* **66**, 2247–2250 (1991).

[Kash et al. 1988]
K. Kash, J. M. Worlock, M. D. Sturge, P. Grabbe, J. P. Harbison, A. Scherer, and P. S. D. Lin, "Strain-induced lateral confinement of excitons in GaAs-AlGaAs quantum well microstructures", *Applied Physics Letters* **53**, 782–784 (1988).

[Kasprzak et al. 2006]
J. Kasprzak, M. Richard, S. Kundermann, A. Baas, P. Jeambrun, J. M. J. Keeling, F. M. Marchetti, M. H. Szymańska, R. André, J. L. Staehli, V. Savona, P. B. Littlewood, B. Deveaud, and L. S. Dang, "Bose-Einstein condensation of exciton polaritons", *Nature* **443**, 409–414 (2006).

[Keeling et al. 2004]
J. Keeling, L. S. Levitov, and P. B. Littlewood, "Angular Distribution of Photoluminescence as a Probe of Bose Condensation of Trapped Excitons", *Phys. Rev. Lett.* **92**, 176402 (2004).

[Keldysh et al. 1968]
L. V. Keldysh and A. N. Kozlov, "Collective Properties of Excitons in Semiconductors", *Soviet Physics JETP* **27**, 251–254 (1968).

[Ketterle et al. 1996]
W. Ketterle and N. J. van Druten, "Bose-Einstein condensation of a finite number of particles trapped in one or three dimensions", *Phys. Rev. A* **54**, 656–660 (1996).

[Klitzing et al. 1980]
K. v. Klitzing, G. Dorda, and M. Pepper, "New Method for High-Accuracy Determination of the Fine-Structure Constant Based on Quantized Hall Resistance", *Phys. Rev. Lett.* **45**, 494–497 (1980).

[Kosterlitz et al. 1973]
J. M. Kosterlitz and D. J. Thouless, "Ordering, metastability and phase transitions in two-dimensional systems", *Journal of Physics C: Solid State Physics* **6**, 1181 (1973).

[Kotthaus 2006]
J. P. Kotthaus, "Manipulating luminescence in semiconductor nanostructures via

field-effect-tuneable potentials", *Physica Status Solidi B Basic Research* **243**, 3754–3763 (2006).

[Kowalik-Seidl et al. 2010]
K. Kowalik-Seidl, X. P. Vögele, B. N. Rimpfl, S. Manus, J. P. Kotthaus, D. Schuh, W. Wegscheider, and A. W. Holleitner, "Long exciton spin relaxation in coupled quantum wells", *Appl. Phys. Lett.* **97**, 011104 (2010).

[Kowalik-Seidl et al. 2011]
K. Kowalik-Seidl, X. P. Vögele, F. Seilmeier, D. Schuh, W. Wegscheider, A. W. Holleitner, and J. P. Kotthaus, "Forming and confining of dipolar excitons by quantizing magnetic fields", *Phys. Rev. B* **83**, 081307 (2011).

[Kowalik-Seidl et al. 2012]
K. Kowalik-Seidl, X. P. Voegele, B. N. Rimpfl, G. J. Schinner, D. Schuh, W. Wegscheider, A. W. Holleitner, and J. P. Kotthaus, "Tunable Photoemission from an Excitonic Antitrap", *Nano Letters* **12**, 326–330 (2012).

[Krauss et al. 2004]
J. Krauss, J. P. Kotthaus, A. Wixforth, M. Hanson, D. C. Driscoll, A. C. Gossard, D. Schuh, and M. Bichler, "Capture and release of photonic images in a quantum well", *Applied Physics Letters* **85**, 5830–5832 (2004).

[Kubouchi et al. 2005]
M. Kubouchi, K. Yoshioka, R. Shimano, A. Mysyrowicz, and M. Kuwata-Gonokami, "Study of Orthoexciton-to-Paraexciton Conversion in Cu_2O by Excitonic Lyman Spectroscopy", *Phys. Rev. Lett.* **94**, 016403 (2005).

[Kukushkin et al. 2011]
I. V. Kukushkin, A. V. Rossokhaty, S. Schmult, and K. von Klitzing, "Binding energy of indirect excitons in asymmetric double quantum wells", *Semiconductor Science and Technology* **26**, 014023 (2011).

[Kuznetsova et al. 2010]
Y. Y. Kuznetsova, M. Remeika, A. A. High, A. T. Hammack, L. V. Butov, M. Hanson, and A. C. Gossard, "All-optical excitonic transistor", *Opt. Lett.* **35**, 1587–1589 (2010).

[Kuznetsova et al. 2012]
Y. Y. Kuznetsova, J. R. Leonard, L. V. Butov, J. Wilkes, E. A. Muljarov, K. L. Campman, and A. C. Gossard, "Excitation Energy Dependence of the Exciton Inner Ring", *ArXiv 1202.3096* (2012).

[Lagoudakis et al. 2008]
K. G. Lagoudakis, M. Wouters, M. Richard, A. Baas, I. Carusotto, R. André, L. S.

Dang, and B. Deveaud-Plédran, "Quantized vortices in an exciton-polariton condensate", *Nature Physics* **4**, 706 (2008).

[Laikhtman et al. 2009]
B. Laikhtman and R. Rapaport, "Exciton correlations in coupled quantum wells and their luminescence blue shift", *Phys. Rev. B* **80**, 195313 (2009).

[Larionov et al. 2002]
A. V. Larionov, V. B. Timofeev, P. A. Ni, S. V. Dubonos, I. Hvam, and K. Soerensen, "Bose Condensation of Interwell Excitons in Double Quantum Wells", *Soviet Journal of Experimental and Theoretical Physics Letters* **75**, 570–574 (2002).

[Latta et al. 2011]
C. Latta, F. Haupt, M. Hanl, A. Weichselbaum, M. Claassen, W. Wuester, P. Fallahi, S. Faelt, L. Glazman, J. von Delft, H. E. Türeci, and I. A., "Quantum quench of Kondo correlations in optical absorption", *Nature* **474**, 627–630 (2011).

[Laux et al. 1988]
S. Laux, D. Frank, and F. Stern, "Quasi-one-dimensional electron states in a split-gate GaAs/AlGaAs heterostructure", *Surface Science* **196**, 101 –106 (1988).

[Leggett 1999]
A. J. Leggett, "Superfluidity", *Rev. Mod. Phys.* **71**, S318–S323 (1999).

[Leonard et al. 2009]
J. R. Leonard, Y. Y. Kuznetsova, S. Yang, L. V. Butov, T. Ostatnicky, A. Kavokin, and A. C. Gossard, "Spin Transport of Excitons", *Nano Letters* **9**, 4204–4208 (2009).

[Li et al. 1999]
M. Li, L. Chen, and C. Chen, "Density of states of particles in a generic power-law potential in any dimensional space", *Phys. Rev. A* **59**, 3109–3111 (1999).

[Li et al. 2003]
X. Li, Y. Wu, D. Steel, D. Gammon, T. H. Stievater, D. S. Katzer, D. Park, C. Piermarocchi, and L. J. Sham, "An All-Optical Quantum Gate in a Semiconductor Quantum Dot", *Science* **301**, 809–811 (2003).

[London 1938]
F. London, "On the Bose-Einstein Condensation", *Phys. Rev.* **54**, 947–954 (1938).

[Loss et al. 1998]
D. Loss and D. P. DiVincenzo, "Quantum computation with quantum dots", *Phys. Rev. A* **57**, 120–126 (1998).

[Lozovik et al. 1975]
Y. E. Lozovik and V. I. Yudson, "Feasibility of superfluidity of paired spatially

separated electrons and holes; a new superconductivity mechanism", *Soviet Journal of Experimental and Theoretical Physics Letters* **22**, 274 (1975).

[Lozovik et al. 1976]
Y. E. Lozovik and V. I. Yudson, "A new mechanism for superconductivity: pairing between spatially separated electrons and holes", *Soviet Journal of Experimental and Theoretical Physics* **44**, 389 (1976).

[Lozovik et al. 1997]
Y. E. Lozovik and A. M. Ruvinsky, "Magnetoexcitons in coupled quantum wells", *Physics Letters A* **227**, 271–284 (1997).

[Lozovik et al. 1999]
Y. E. Lozovik, O. L. Berman, and A. M. Ruvinskiĭ, "Superfluidity of dirty excitons", *Soviet Journal of Experimental and Theoretical Physics Letters* **69**, 616–622 (1999).

[Lozovik et al. 2002a]
Y. E. Lozovik, I. V. Ovchinnikov, S. Y. Volkov, L. V. Butov, and D. S. Chemla, "Quasi-two-dimensional excitons in finite magnetic fields", *Phys. Rev. B* **65**, 235304 (2002).

[Lozovik et al. 2002b]
Y. E. Lozovik, O. L. Berman, and M. Willander, "Superfluidity of indirect excitons and biexcitons in coupled quantum wells and superlattices", *Journal of Physics: Condensed Matter* **14**, 12457 (2002).

[Lundstrom et al. 1999]
T. Lundstrom, W. Schoenfeld, H. Lee, and P. M. Petroff, "Exciton Storage in Semiconductor Self-Assembled Quantum Dots", *Science* **286**, 2312–2314 (1999).

[Mahan 1967]
G. D. Mahan, "Excitons in Degenerate Semiconductors", *Phys. Rev.* **153**, 882–889 (1967).

[Matthews et al. 1999]
M. R. Matthews, B. P. Anderson, P. C. Haljan, D. S. Hall, C. E. Wieman, and E. A. Cornell, "Vortices in a Bose-Einstein Condensate", *Phys. Rev. Lett.* **83**, 2498–2501 (1999).

[Matuszewski et al. 2012]
M. Matuszewski, T. Taylor, and A. V. Kavokin, "Exciton Supersolidity in Hybrid Bose-Fermi Systems", *Phys. Rev. Lett.* **108**, 060401 (2012).

[Mermin et al. 1966]
N. D. Mermin and W. H., "Absence of Ferromagnetism or Antiferromagnetism in

One- or Two-Dimensional Isotropic Heisenberg Models", *Phys. Rev. Lett.* **17**, 1133 –1136 (1966).

[Michaelis de Vasconcellos et al. 2010]
S. Michaelis de Vasconcellos, S. Gordon, M. Bichler, T. Meier, and A. Zrenner, "Coherent control of a single exciton qubit by optoelectronic manipulation", *Nature Photonics* **4**, 545–548 (2010).

[Miller et al. 1984]
D. A. B. Miller, D. S. Chemla, T. C. Damen, A. C. Gossard, W. Wiegmann, T. H. Wood, and C. A. Burrus, "Band-Edge Electroabsorption in Quantum Well Structures: The Quantum-Confined Stark Effect", *Phys. Rev. Lett.* **53**, 2173–2176 (1984).

[Miller et al. 1985]
D. A. B. Miller, D. S. Chemla, T. C. Damen, A. C. Gossard, W. Wiegmann, T. H. Wood, and C. A. Burrus, "Electric field dependence of optical absorption near the band gap of quantum-well structures", *Phys. Rev. B* **32**, 1043–1060 (1985).

[Miller et al. 1981]
R. C. Miller, D. A. Kleinman, W. T. Tsang, and A. C. Gossard, "Observation of the excited level of excitons in GaAs quantum wells", *Phys. Rev. B* **24**, 1134–1136 (1981).

[Morales et al. 2008]
A. L. Morales, N. Raigoza, C. A. Duque, and L. E. Oliveira, "Effects of growth-direction electric and magnetic fields on excitons in GaAs-$Ga_{1-x}Al_xAs$ coupled double quantum wells", *Phys. Rev. B* **77**, 113309 (2008).

[Moskalenko 1962]
S. A. Moskalenko, "Reversible optic-hydrodynamic phenomena in a non ideal exciton gas", *Soviet Physics Solid State* **4**, 199–204 (1962).

[Mott 1938]
N. F. Mott, "Conduction in polar crystals. II. The conduction band and ultra-violet absorption of alkali-halide crystals.", *Trans. Faraday Soc.* **34**, 500 (1938).

[Mullin 1997]
W. J. Mullin, "Bose-Einstein condensation in a harmonic potential", *Journal of Low Temperature Physics* **106**, 615–641 (1997).

[Negoita et al. 1999]
V. Negoita, D. W. Snoke, and K. Eberl, "Stretching quantum wells: A method for trapping free carriers in GaAs heterostructures", *Applied Physics Letters* **75**, 2059–2061 (1999).

[Negoita et al. 2000]
V. Negoita, D. W. Snoke, and K. Eberl, "Huge density-dependent blueshift of indirect excitons in biased coupled quantum wells", *Phys. Rev. B* **61**, 2779–2783 (2000).

[Novoselov et al. 2005]
K. S. Novoselov, A. K. Geim, S. V. Morozov, D. Jiang, M. I. Katsnelson, I. V. Grigorieva, S. V. Dubonos, and A. A. Firsov, "Two-dimensional gas of massless Dirac fermions in graphene", *Nature* **438**, 197–200 (2005).

[Osheroff et al. 1972]
D. D. Osheroff, R. C. Richardson, and D. M. Lee, "Evidence for a New Phase of Solid He3", *Phys. Rev. Lett.* **28**, 885–888 (1972).

[Penrose et al. 1956]
O. Penrose and L. Onsager, "Bose-Einstein Condensation and Liquid Helium", *Phys. Rev.* **104**, 576–584 (1956).

[Petrov et al. 2000]
D. S. Petrov, M. Holzmann, and G. V. Shlyapnikov, "Bose-Einstein Condensation in Quasi-2D Trapped Gases", *Physical Review Letters* **84**, 2551–2555 (2000).

[Peyghambarian et al. 1984]
N. Peyghambarian, H. M. Gibbs, J. L. Jewell, A. Antonetti, A. Migus, D. Hulin, and A. Mysyrowicz, "Blue Shift of the Exciton Resonance due to Exciton-Exciton Interactions in a Multiple-Quantum-Well Structure", *Phys. Rev. Lett.* **53**, 2433–2436 (1984).

[Phillips 1998]
W. D. Phillips, "Nobel Lecture: Laser cooling and trapping of neutral atoms", *Rev. Mod. Phys.* **70**, 721–741 (1998).

[Posazhennikova 2006]
A. Posazhennikova, "Weakly interacting, dilute Bose gases in 2D", *Rev. Mod. Phys.* **78**, 1111–1134 (2006).

[Raman et al. 1999]
C. Raman, M. Köhl, R. Onofrio, D. S. Durfee, C. E. Kuklewicz, Z. Hadzibabic, and W. Ketterle, "Evidence for a Critical Velocity in a Bose-Einstein Condensed Gas", *Phys. Rev. Lett.* **83**, 2502–2505 (1999).

[Ramsay et al. 2008]
A. J. Ramsay, S. J. Boyle, R. S. Kolodka, J. B. B. Oliveira, J. Skiba-Szymanska, H. Y. Liu, M. Hopkinson, A. M. Fox, and M. S. Skolnick, "Fast Optical Preparation, Control, and Readout of a Single Quantum Dot Spin", *Phys. Rev. Lett.* **100**, 197401 (2008).

[Rapaport et al. 2005]
R. Rapaport, G. Chen, S. Simon, O. Mitrofanov, L. Pfeiffer, and P. M. Platzman, "Electrostatic traps for dipolar excitons", *Phys. Rev. B* **72**, 075428 (2005).

[Rapaport et al. 2007]
R. Rapaport and G. Chen, "Experimental methods and analysis of cold and dense dipolar exciton fluids", *Journal of Physics: Condensed Matter* **19**, 295207 (2007).

[Regal et al. 2003]
C. A. Regal, C. Ticknor, J. L. Bohn, and D. S. Jin, "Creation of ultracold molecules from a Fermi gas of atoms", *Nature* **424**, 47–50 (2003).

[Regal et al. 2004]
C. A. Regal, M. Greiner, and D. S. Jin, "Observation of Resonance Condensation of Fermionic Atom Pairs", *Phys. Rev. Lett.* **92**, 040403 (2004).

[Remeika et al. 2012]
M. Remeika, M. M. Fogler, L. V. Butov, M. Hanson, and A. C. Gossard, "Two-dimensional electrostatic lattices for indirect excitons", *Applied Physics Letters* **100**, 061103 (2012).

[Riedel et al. 2010]
M. F. Riedel, P. Böhi, Y. Li, T. W. Hänsch, A. Sinatra, and P. Treutlein, "Atom-chip-based generation of entanglement for quantum metrology", *Nature* **464**, 1170–1173 (2010).

[Rocke et al. 1997]
C. Rocke, S. Zimmermann, A. Wixforth, J. P. Kotthaus, G. Böhm, and G. Weimann, "Acoustically Driven Storage of Light in a Quantum Well", *Phys. Rev. Lett.* **78**, 4099–4102 (1997).

[Rudolph et al. 2007]
J. Rudolph, R. Hey, and P. V. Santos, "Long-Range Exciton Transport by Dynamic Strain Fields in a GaAs Quantum Well", *Phys. Rev. Lett.* **99**, 047602 (2007).

[Sakaki et al. 1987]
H. Sakaki, T. Noda, K. Hirakawa, M. Tanaka, and T. Matsusue, "Interface roughness scattering in GaAs/AlAs quantum wells", *Applied Physics Letters* **51**, 1934–1936 (1987).

[Schafroth 1954]
M. R. Schafroth, "Superconductivity of a Charged Boson Gas", *Phys. Rev.* **96**, 1149–1149 (1954).

[Schindler et al. 2008]
C. Schindler and R. Zimmermann, "Analysis of the exciton-exciton interaction in semiconductor quantum wells", *Phys. Rev. B* **78**, 045313 (2008).

[Schinner et al. 2011a]
G. J. Schinner, E. Schubert, M. P. Stallhofer, J. P. Kotthaus, D. Schuh, A. K. Rai, D. Reuter, A. D. Wieck, and A. O. Govorov, "Electrostatically trapping indirect excitons in coupled $In_xGa_{1-x}As$ quantum wells", *Phys. Rev. B* **83**, 165308 (2011).

[Schinner et al. 2011b]
G. J. Schinner, J. Repp, E. Schubert, A. K. Rai, D. Reuter, A. D. Wieck, A. O. Govorov, A. Holleitner, and J. P. Kotthaus, "Many-body correlations of electrostatically trapped dipolar excitons", *ArXiv, 1111.7175* (2011).

[Schmitt-Rink et al. 1985]
S. Schmitt-Rink, D. S. Chemla, and D. A. B. Miller, "Theory of transient excitonic optical nonlinearities in semiconductor quantum-well structures", *Phys. Rev. B* **32**, 6601–6609 (1985).

[Schmitt-Rink et al. 1989]
S. Schmitt-Rink, D. Chemla, and D. Miller, "Linear and nonlinear optical properties of semiconductor quantum wells", *Advances in Physics* **38**, 89–188 (1989).

Schubert, Enrico. *Elektrostatische Fallen für indirekte Exzitonen in gekoppelten InGaAs-Quantentöpfen.* Diploma thesis. Ludwig-Maximilians-Universität München. 2010.

[Sivalertporn et al. 2012]
K. Sivalertporn, L. Mouchliadis, A. L. Ivanov, R. Philp, and E. A. Muljarov, "Direct and indirect excitons in semiconductor coupled quantum wells in an applied electric field", *Phys. Rev. B* **85**, 045207 (2012).

[Skolnick et al. 1987]
M. S. Skolnick, J. M. Rorison, K. J. Nash, D. J. Mowbray, P. R. Tapster, S. J. Bass, and A. D. Pitt, "Observation of a Many-Body Edge Singularity in Quantum-Well Luminescence Spectra", *Phys. Rev. Lett.* **58**, 2130–2133 (1987).

[Snoke 2011]
D. W. Snoke, "Coherence and Optical Emission from Bilayer Exciton Condensates", *Advances in Condensed Matter Physics* **2011**, 938609 (2011).

[Snoke et al. 1990]
D. W. Snoke, J. P. Wolfe, and A. Mysyrowicz, "Evidence for Bose-Einstein condensation of excitons in Cu_2O", *Phys. Rev. B* **41**, 11171–11184 (1990).

[Snoke et al. 2005]
D. W. Snoke, Y. Liu, Z. Vörös, L. Pfeiffer, and K. West, "Trapping long-lifetime excitons in a two-dimensional harmonic potential", *Solid State Communications* **134**, 37–42 (2005).

[Sommer et al. 2012]
A. T. Sommer, L. W. Cheuk, M. J. H. Ku, W. S. Bakr, and M. W. Zwierlein, "Evolution of Fermion Pairing from Three to Two Dimensions", *Phys. Rev. Lett.* **108**, 045302 (2012).

[Spielman et al. 2000]
I. B. Spielman, J. P. Eisenstein, L. N. Pfeiffer, and K. W. West, "Resonantly Enhanced Tunneling in a Double Layer Quantum Hall Ferromagnet", *Phys. Rev. Lett.* **84**, 5808–5811 (2000).

Stallhofer, Markus. *Untersuchung indirekter Exzitonen in gekoppelten InGaAs-Quantentöpfen*. Diploma thesis. Ludwig-Maximilians-Universität München. 2009.

[Stern et al. 2008a]
M. Stern, V. Garmider, V. Umansky, and I. Bar-Joseph, "Mott Transition of Excitons in Coupled Quantum Wells", *Phys. Rev. Lett.* **100**, 256402 (2008).

[Stern et al. 2008b]
M. Stern, V. Garmider, E. Segre, M. Rappaport, V. Umansky, Y. Levinson, and I. Bar-Joseph, "Photoluminescence Ring Formation in Coupled Quantum Wells: Excitonic Versus Ambipolar Diffusion", *Phys. Rev. Lett.* **101**, 257402 (2008).

[Stotz et al. 2005]
J. A. H. Stotz, R. Hey, P. V. Santos, and K. H. Ploog, "Coherent spin transport through dynamic quantum dots", *Nature Materials* **4**, 585 (2005).

[Strecker et al. 2003]
K. E. Strecker, G. B. Partridge, and R. G. Hulet, "Conversion of an Atomic Fermi Gas to a Long-Lived Molecular Bose Gas", *Phys. Rev. Lett.* **91**, 080406 (2003).

[Szymanska et al. 2003]
M. H. Szymanska and P. B. Littlewood, "Excitonic binding in coupled quantum wells", *Phys. Rev. B* **67**, 193305 (2003).

[Tanzilli et al. 2005]
S. Tanzilli, W. Tittel, M. Halder, O. Alibart, P. Baldi, N. Gisin, and H. Zbinden, "A photonic quantum information interface", *Nature* **437**, 116–120 (2005).

[Tersoff 1984]
J. Tersoff, "Theory of semiconductor heterojunctions: The role of quantum dipoles", *Phys. Rev. B* **30**, 4874–4877 (1984).

[Timofeev et al. 1999]
V. B. Timofeev, A. V. Larionov, M. G. Alessi, M. Capizzi, A. Frova, and J. M. Hvam, "Charged excitonic complexes in GaAs/$Al_{0.35}Ga_{0.65}As$ *p-i-n* double quantum wells", *Phys. Rev. B* **60**, 8897–8901 (1999).

[Timofeev et al. 2007]
V. B. Timofeev and A. V. Gorbunov, "Collective state of the Bose gas of interacting dipolar excitons", *J. Appl. Phys.* **101**, 081708 (2007).

[Trauernicht et al. 1983]
D. P. Trauernicht, A. Mysyrowicz, and J. P. Wolfe, "Strain confinement and thermodynamics of free excitons in a direct-gap semiconductor", *Phys. Rev. B* **28**, 3590–3592 (1983).

[Tsui et al. 1982]
D. C. Tsui, H. L. Stormer, and A. C. Gossard, "Two-Dimensional Magnetotransport in the Extreme Quantum Limit", *Phys. Rev. Lett.* **48**, 1559–1562 (1982).

[Turberfield et al. 1990]
A. J. Turberfield, S. R. Haynes, P. A. Wright, R. A. Ford, R. G. Clark, J. F. Ryan, J. J. Harris, and C. T. Foxon, "Optical detection of the integer and fractional quantum Hall effects in GaAs", *Phys. Rev. Lett.* **65**, 637–640 (1990).

[Türeci et al. 2011]
H. E. Türeci, M. Hanl, M. Claassen, A. Weichselbaum, T. Hecht, B. Braunecker, A. Govorov, L. Glazman, A. Imamoglu, and J. von Delft, "Many-Body Dynamics of Exciton Creation in a Quantum Dot by Optical Absorption: A Quantum Quench towards Kondo Correlations", *Phys. Rev. Lett.* **106**, 107402 (2011).

[Van Wees et al. 1988]
B. J. van Wees, H. van Houten, C. W. J. Beenakker, J. G. Williamson, L. P. Kouwenhoven, D. van der Marel, and C. T. Foxon, "Quantized conductance of point contacts in a two-dimensional electron gas", *Phys. Rev. Lett.* **60**, 848–850 (1988).

[Vögele et al. 2009a]
X. P. Vögele, D. Schuh, W. Wegscheider, J. P. Kotthaus, and A. W. Holleitner, "Density Enhanced Diffusion of Dipolar Excitons within a One-Dimensional Channel", *Phys. Rev. Lett.* **103**, 126402 (2009).

[Vörös et al. 2005]
Z. Vörös, R. Balili, D. W. Snoke, L. Pfeiffer, and K. West, "Long-Distance Diffusion of Excitons in Double Quantum Well Structures", *Phys. Rev. Lett.* **94**, 226401 (2005).

[Vörös et al. 2006]
Z. Vörös, D. W. Snoke, L. Pfeiffer, and K. West, "Trapping Excitons in a Two-Dimensional In-Plane Harmonic Potential: Experimental Evidence for Equilibration of Indirect Excitons", *Phys. Rev. Lett.* **97**, 016803 (2006).

[Vörös et al. 2009b]
Z. Vörös, D. W. Snoke, L. Pfeiffer, and K. West, "Direct Measurement of Exciton-Exciton Interaction Energy", *Phys. Rev. Lett.* **103**, 016403 (2009).

[Walck et al. 1998]
S. N. Walck and T. L. Reinecke, "Exciton diamagnetic shift in semiconductor nanostructures", *Phys. Rev. B* **57**, 9088–9096 (1998).

[Wannier 1937]
G. H. Wannier, "The Structure of Electronic Excitation Levels in Insulating Crystals", *Phys. Rev.* **52**, 191–197 (1937).

[Warburton et al. 2000]
R. J. Warburton, C. Schäflein, D. Haft, F. Bickel, A. Lorke, K. Karrai, J. M. Garcia, W. Schoenfeld, and P. M. Petroff, "Optical emission from a charge-tunable quantum ring", *Nature* **405**, 926–929 (2000).

[Weitenberg et al. 2011]
C. Weitenberg, M. Endres, J. F. Sherson, M. Cheneau, P. Schauß, T. Fukuhara, I. Bloch, and S. Kuhr, "Single-spin addressing in an atomic Mott insulator", *Nature* **471**, 319–324 (2011).

[Wendler et al. 1996]
L. Wendler, V. M. Fomin, A. V. Chaplik, and A. O. Govorov, "Optical properties of two interacting electrons in quantum rings: Optical absorption and inelastic light scattering", *Phys. Rev. B* **54**, 4794–4810 (1996).

[Wharam et al. 1988]
D. A. Wharam, T. J. Thornton, R Newbury, M Pepper, H Ahmed, J. E. F. Frost, D. G. Hasko, D. C. Peacock, D. A. Ritchie, and G. A. C. Jones, "One-dimensional transport and the quantisation of the ballistic resistance", *Journal of Physics C: Solid State Physics* **21**, L209 (1988).

[Widom 1968]
A. Widom, "Superfluid Phase Transitions in One and Two Dimensions", *Phys. Rev.* **176**, 254–257 (1968).

[Wiemann et al. 1998]
C. Wiemann, M. Versen, and A. D. Wieck, "Direct writing of active loads by focused ion beams", *J. Vac. Sci. Techn. B* **16**, 2567–2569 (1998).

[Winbow et al. 2008]
A. G. Winbow, L. V. Butov, and A. C. Gossard, "Photon storage with subnanosecond readout rise time in coupled quantum wells", *Journal of Applied Physics* **104**, 063515 (2008).

[Winbow et al. 2011]
A. G. Winbow, J. R. Leonard, M. Remeika, Y. Y. Kuznetsova, A. A. High, A. T. Hammack, L. V. Butov, J. Wilkes, A. A. Guenther, A. L. Ivanov, M. Hanson, and A. C. Gossard, "Electrostatic Conveyer for Excitons", *Phys. Rev. Lett.* **106**, 196806 (2011).

[Winbow et al. 2007]
A. G. Winbow, A. T. Hammack, L. V. Butov, and A. C. Gossard, "Photon Storage with Nanosecond Switching in Coupled Quantum Well Nanostructures", *Nano Letters* **7**, 1349–1351 (2007).

[Yan 2000]
Z. Yan, "General thermal wavelength and its applications", *European Journal of Physics* **21**, 625–631 (2000).

[Yang 1962]
C. N. Yang, "Concept of Off-Diagonal Long-Range Order and the Quantum Phases of Liquid He and of Superconductors", *Rev. Mod. Phys.* **34**, 694–704 (1962).

[Yang et al. 2006]
S. Yang, A. T. Hammack, M. M. Fogler, L. V. Butov, and A. C. Gossard, "Coherence Length of Cold Exciton Gases in Coupled Quantum Wells", *Phys. Rev. Lett.* **97**, 187402 (2006).

[Yoon et al. 2010]
Y. Yoon, L. Tiemann, S. Schmult, W. Dietsche, K. von Klitzing, and W. Wegscheider, "Interlayer Tunneling in Counterflow Experiments on the Excitonic Condensate in Quantum Hall Bilayers", *Phys. Rev. Lett.* **104**, 116802 (2010).

[Yoshioka et al. 1990]
D. Yoshioka and A. H. MacDonald, "Double quantum well electron-hole systems in strong magnetic fields", *Journal of the Physical Society of Japan* **59**, 4211–4214 (1990).

[Yoshioka et al. 2011]
K. Yoshioka, E. Chae, and M. Kuwata-Gonokami, "Transition to a Bose-Einstein condensate and relaxation explosion of excitons at sub-Kelvin temperatures", *Nature Communications* **2** (2011).

[Yusa et al. 2001]
G. Yusa, H. Shtrikman, and I. Bar-Joseph, "Charged Excitons in the Fractional Quantum Hall Regime", *Phys. Rev. Lett.* **87**, 216402 (2001).

[Zhu et al. 1995]
X. Zhu, P. B. Littlewood, M. S. Hybertsen, and T. M. Rice, "Exciton Condensate in Semiconductor Quantum Well Structures", *Phys. Rev. Lett.* **74**, 1633–1636 (1995).

[Zimmermann et al. 2007]
R. Zimmermann and C. Schindler, "Exciton-exciton interaction in coupled quantum wells", *Solid State Communications* **144**, 395 –398 (2007).

[Zimmermann et al. 1997]
S. Zimmermann, A. O. Govorov, W. Hansen, J. P. Kotthaus, M. Bichler, and W. Wegscheider, "Lateral superlattices as voltage-controlled traps for excitons", *Phys. Rev. B* **56**, 13414–13421 (1997).

[Zimmermann et al. 1998]
S. Zimmermann, G. Schedelbeck, A. O. Govorov, A. Wixforth, J. P. Kotthaus, M. Bichler, W. Wegscheider, and G. Abstreiter, "Spatially resolved exciton trapping in a voltage-controlled lateral superlattice", *Applied Physics Letters* **73**, 154–156 (1998).

[Zimmermann et al. 1999]
S. Zimmermann, A. Wixforth, J. P. Kotthaus, W. Wegscheider, and M. Bichler, "A Semiconductor-Based Photonic Memory Cell", *Science* **283**, 1292 (1999).

[Zrenner et al. 2002]
A. Zrenner, E. Beham, S. Stufler, F. Findeis, M. Bichler, and G. Abstreiter, "Coherent properties of a two-level system based on a quantum-dot photodiode", *Nature* **418**, 612–614 (2002).